Large Eddy Simulation of Turbulent Swirling Flows and Turbulent Premixed Combustion

Wang, Ping

2005

Citation for published version (APA):
Wang, P. (2005). *Large Eddy Simulation of Turbulent Swirling Flows and Turbulent Premixed Combustion*. [Doctoral Thesis (monograph), Fluid Mechanics]. Fluid Mechanics.

Total number of authors:
1

LUND UNIVERSITY

PO Box 117
221 00 Lund
+46 46-222 00 00

Large Eddy Simulation of Turbulent Swirling Flows and Turbulent Premixed Combustion

Ping Wang

January 2005

Thesis for the degree of Doctor of Philosophy in engineering.
ISBN 91–628–6376–2
ISRN LUTMDN/TMHP–05/1025–SE
ISSN 0282-1990

Division of Fluid Mechanics
Department of Heat and Power Engineering
Lund Institute of Technology
Box 118
SE–221 00 Lund
Sweden

Printed by KFS AB, Lund, December 2004

Abstract

With the increasing concerns about our environment and human health, more and more stringent emission limits have been specified. These adopted and still coming emission limits require and promote more accurate, less experiential methods to design and develop the combustors. In this thesis, computation fluid dynamics (CFD) technology, based on large eddy simulation (LES) and level set *G*-equation methods, is applied to study the turbulent premixed combustion related problems. This thesis work consists of three parts.

First, this thesis studies the flow structures of isothermal turbulent swirling flows in a dump combustor related geometry, and compared the simulation results with corresponding experimental data. The aims are to gain deeper understanding of the flow and turbulence structures in dump combustors and to examine the capability of LES for prediction of turbulent swirling flows. With appropriate inflow, outflow boundary conditions, and fine grid resolution, LES successfully simulates the vortex breakdown, and the anisotropic turbulence structures for all the swirl numbers considered. Large-scale motion of the vortex core center, i.e. the so-called precessing vortex core (PVC) phenomenon, is predicted. The PVC is found to rotate around the combustor axis at a frequency about 18–25 Hz (Strouhal number about 0.17–0.4).

To model the turbulent premixed combustion processes, a level set *G*-equation is first derived in the LES framework. Some aspects of the level set *G*-equation have also been addressed in detail in this dissertation. This level set *G*-equation combined with the stationary flamelet library is used to simulate a lean premixed propane/air flame in a jet engine afterburner. The results indicate that the fluctuation of the flame surface, which is responsible for the broadening of the time averaged mean flame brush by turbulence, depends on the large resolved turbulence eddies. Time averaged mean flow velocity, temperature and major species concentrations also mainly depend on these large scale resolved eddies. Contrarily, the unresolved subgrid scale (SGS) eddies mainly contribute to the wrinkling at the SGS level and play an important role in the enhancement of the propagation speed of the resolved flame front. In addition, the spatially filtered intermediate species such as CO strongly depends on the small SGS eddies.

Further, the effect of subgrid scale eddies on the wrinkling of premixed turbulent flame is studied using a so-called *h*-equation, in which the flow field is a prescribed shear flow field with eddies of different scales. It is shown that the effect of subgrid eddies on the wrinkling of flame surface decreases monotonically with the LES filter size; however, the decrease rate strongly depends on the filter size. This implies that, if one wants to resolve most of the flame wrinkling, rather fine grid resolution and filter size should be used.

Key words: level set *G*-equation, swirling flow, turbulent premixed combustion, vortex breakdown, large eddy simulation, flame wrinkle, flamelet model.

Acknowledgments

This work was supported by the Swedish Research Council (VR), and partially supported by the Center for Combustion Science and Technology (CeCOST) and the National Supercomputer Center (NSC) in Linköping, Sweden.

I am very grateful to Prof. Xue-Song Bai for introducing me to the field of numerical analysis of turbulent combustion, and I also would like to give thanks for all his effort, guidance and suggestions. Without his patient support and discussions this thesis would not have been possible.

Thanks also go to Prof. Laszlo Fuchs for valuable commenting on this thesis work, docent Johan Revstedt for many interesting discussions, the department secretaries for their kindness and help, and all the teachers of me for sharing their knowledge, enthusiasm and happiness with me in all the past years.

My present and former colleagues at the Department of Heat and Power Engineering, Daniel Lorstad, Robert Szasz, Jessica Gullbrand, Per Nilsson, Ulf Engdar, Karl-Johan Nogenmyr, Rixin Yu, Ashraf Elfasakhany, just an incomplete list, deserve acknowledgement for their interesting questions and continuous support. I would also like to thank my roommate, Torbern Klason, for sharing a ‘disorderly’ office with me for two years, for his encouragement about the life, and for being my Swedish teacher without pay.

I own a lot to my kindly mother and all other family members. It is a pity that I can not pay them back for their never-failing support, understanding and love, even with my whole life.

Last, but not least, I would like to thank all the friends I made in this lovely Lund. I will never forget their selfless help and continuous support, and I will remember all the happiness and sadness they shared with me.

Thank you, my lovely Lund! Thank you, my dear Lover!

Preface

This thesis deals with turbulent swirling flows in a dump combustor and turbulent lean premixed flame in a jet engine afterburner using LES and level set *G*-equation methods. It is based on the following papers:

1. Wang P., Bai X.S., Wessman M. and Klingmann J. Large eddy simulation and experimental studies of a confined turbulent swirling flow. *Physics of Fluids*, 16(9): 3306–3324, 2004.

2. Wang P., Bai X.S. Large eddy simulation of turbulent swirling flows in a dump combustor: a sensitivity study. *International Journal for Numerical Methods in Fluids*, 47: 99–120, 2005.

3. Wang P., Bai X.S. Large eddy simulation of turbulent premixed flames using level-set *G*-equation. *Proceedings of the Combustion Institute*, 30: 583–591, 2004.

4. Wang P., Bai X.S. Large eddy simulation of premixed turbulent flames by *G*-equation. *Proceedings of the Third Mediterranean Combustion Symposium*, Marrakech, Morocco, pages: 951–959, June 8–13, 2003.

5. Bai X.S., Wang P. Large eddy simulation of flame wrinkling in turbulent premixed combustion. *Proceedings of the Joint Meeting of Scandinavian–Nordic and Italian Sections of the Combustion Institute*, Ischia, Italy, No. 2.13, September 18–21, 2003.

Contents

Chapter 1

Introduction

1.1 Combustion and pollutant emissions

Combustion, which is defined in Webster's dictionary as "*rapid oxidation generating heat, or both light and heat; also, slow oxidation accompanied by relatively little heat and no light*" (Turns, 2000), is so essential to human being's existence on this planet. From house illumination, house heating, food cooking, to motor vehicles, many things shows the importance of combustion in our daily life. In a larger scale, industrial processes rely even more heavily on combustion. Iron, steel factories, cement manufacturing industry, transportation system rely almost entirely on combustion, to give just a few examples. It is estimated that, at present, approximate 90% global energy use comes from combustion processes, and the global energy need increase by 3% per year (Bengtsson & Andersson, 2002). In the foreseeable future, combustion will still be the main source of energy provider.

The combustion process typically burns fuel in a device to create heat and power. Most fuels are mixtures of hydrocarbons, e.g. gasoline and diesel fuels, which are compounds that contain hydrogen and carbon atoms. In 'perfect' combustion, oxygen in the air would combine with all the hydrogen in the fuel to form water and with all the carbon in the fuel to form carbon dioxide. Nitrogen in the air would remain unaffected. In reality, the combustion process is not 'perfect', and combustion devices emit several types of pollutants as combustion byproducts.

Pollutants generated by combustion include particulate matter (Turns, 2000; Glassman, 1996), such as fly ash, soot, various aerosols, etc.; the sulfur oxides, SO_2 and SO_3; unburned and partially burned hydrocarbons (UHC); oxides of nitrogen, NO_x, which represents the combination of NO and NO_2; carbon monoxide, CO; and greenhouse gases, particularly CO_2. These pollutants affect our environment and human health in many ways. Seinfeld (1986) indicates four principal effects of pollutants in the troposphere—the lowest layer of the atmosphere:

- Altered properties of the atmosphere and precipitation.
- Harm to vegetation.
- Soiling and deterioration of materials.
- Potential increase of morbidity (sickness) and mortality in humans.

In addition to the air pollution in the troposphere, the pollution is also found in the stratospheric due to the high speed civil transport (HSCT) aircraft (Turns, 2000). Major concern is about the destruction of stratospheric ozone by NO following the reaction mechanism (Turns, 2000)

$$NO + O_3 \rightarrow NO_2 + O_2 \tag{1.1}$$

$$NO_2 + O \rightarrow NO + O_2 \tag{1.2}$$

Depletion of ozone layer allows more harmful ultraviolet solar radiation to penetrate to Earth's surface, therefore increases the possibility of occurrence of some sickness, such as skin cancer.

1.2 Development of low emission combustors

With the increasing concerns about our environment and human health, more and more stringent emission limits have been specified by local or regional regulatory agencies, especially in western industrialized countries. These adopted and still coming emission limits reduced the air pollution to a low level, and promoted the development of combustion technology. Because of this, unlike the earlier stage of the twentieth century, while the mechanical problems and rise of efficiency of the combustor were the principal issues of development, control of pollutant emissions becomes a more and more important focus in the design of modern combustion systems.

Generally, three types of actions (Leckner, 2002) can be used to control the emissions.

- **Post-treat the exhaust gases**

  This method usually uses the catalytic reactions. Selective catalytic reduction (SCR) method is one such method that has been adopted in many engine installations. In SCR, the ammonia is injected into the engine exhaust gases and reacts with NO_x to form water and nitrogen following the reaction mechanism (Lefebvre, 1995)

  $$4NH_3 + 6NO \rightarrow 5N_2 + 6H_2O \tag{1.3}$$

  $$8NH_3 + 6NO_2 \rightarrow 7N_2 + 12H_2O \tag{1.4}$$

  With this approach, around 60%–90% NO_x can be removed from the exhaust gases. These SCR units, however, are expensive to produce, install and maintain, so they are only applied to some industrial engines. For aircraft engines, this method is not practical.

- **Select, clean, and prepare fuel**

  One example is pre-processing the coal to remove the sulphur from it before sending it to the combustor. This can reduce the formation of sulphur dioxide to a large extent. Another example is use of natural gas, in place of distillate fuels. Natural gas (its main component is methane, CH_4) has lower stoichiometric flame temperature, which is good for restraining the thermal NO_x formation. In addition to this, burning CH_4 can produce the same amount of heat release with less CO_2 emission compared with other hydrocarbon fuels, because of its higher heating value and lower molecular weight (Turns, 2000; Glassman, 1996). The drawback of using CH_4 is its gaseous state under natural condition. In the aircraft, the volume for holding the fuel is very limited, so aircraft engines prefer liquid fuels to CH_4.

- **Modify combustion conditions in the combustion chamber**

  This is the preferred option for all combustors, and also the only applicable option for the aircraft engines. The controllable combustion conditions include the global equivalence ratio, local equivalence ratio, peak flame temperature, residence time, and so on.

To meet the stringent emission requirement without hurting the combustion efficiency, scientists and technologists found them in a more and more difficult situation, due to the fact that, the means of improving the combustion efficiency may conflict with the approaches of decreasing the pollutant emissions (Lefebvre, 1995; Bahr, 1999; Turns, 2000). This can be explained by the control of CO and NO emissions in combustion process.

It is known that NO is mainly formed through three chemical routes: 1) thermal or Zeldovich mechanism, 2) prompt or Fenimore mechanism, and 3) fuel bounded nitrogen mechanism (Glassman, 1996; Turns, 2000). Thermal mechanism is a strongly temperature dependent mechanism, in which formation rate of NO is exponentially dependent on the flame temperature. At temperatures below 1850 K, the thermal mechanism is usually unimportant (Lefebvre, 1995). Compared with the time scales of fuel oxidation process, the NO formulation rate is rather slow by the thermal mechanism. In postflame zone, the NO increases almost linearly with time but does not attain its equilibrium value (Lefebvre, 1995).

According to the above discussions, important measures to decrease the NO emission are to reduce the temperature of the flame and to decrease the residence time. The production of CO, however, is high at too low flame temperature, due to the fact that oxidation rate is low at low combustion temperature. This situation is indicated in Figure 1.1 (Lefebvre, 1995).

It is shown that, to obtain low levels of CO and NO_x at the same time, the combustion temperature should be in a fairly narrow window. For example, when temperature is between 1680 and 1900 K, the CO and NO_x levels are below 25 and 15 ppm, respectively. If lower emission level is wanted, this temperature window should be narrower, so the underlying principle of various approaches to develop low-emission combustors is that of maintaining the combustion zone within a fairly narrow band of temperatures over the entire power output range of the combustor.

Combustion processes usually are categorized as premixed and non-premixed (or diffusion) depend on the state of mixedness of the reactants. In a non-premixed flame, the fuel and the oxidizer are initially separated, and the burning occurs only at the

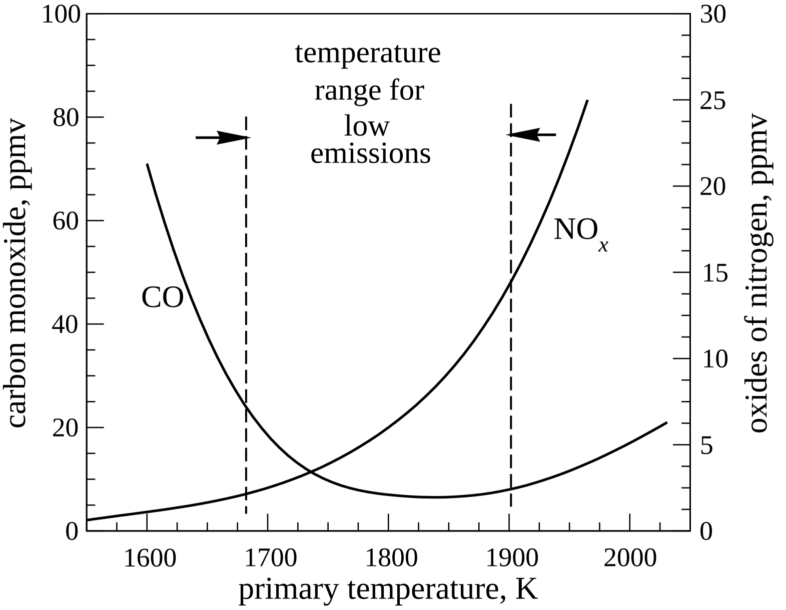

Figure 1.1 Influence of temperature on CO and NO$_x$ emissions (Lefebvre, 1995).

interface between the fuel and oxidizer, where mixing and reaction take place at the same time. Contrarily, in a premixed flame, the fuel and the oxidizer are mixed at the molecular level prior to the reaction. The spark-ignition engine is an example where premixed flames occur, while the candle burning is an example for non-premixed combustion. In practical devices, both types of flames can coexist in some degrees.

In turbulent non-premixed flames, before the reaction can take place, the fuel and oxidizer have to be mixed together on a macro scale by turbulent convection, and then further mixed at small scale by molecular diffusion. Due to the time needed to complete the mixing process, the non-premixed combustion progress ‘slower’ than the premixed combustion, hence it is more stable (Bengtsson & Andersson, 2002). Additionally, the non-premixed burner is free of the flame flashback problem. One of the characteristics of non-premixed combustion is that the reaction always occurs around the stoichiometric surface, so the local peak flame temperature is close to the adiabatic temperature. Unfortunately, the adiabatic temperature is generally higher than the threshold temperature, above which the thermal NO$_x$ production is high. Consequently, the non-premixed combustion is not preferred in the development of low emission combustors (Turns, 2000; Lefebvre, 1995).

In premixed combustions, the fuel and oxidizer are mixed before entering the combustion chamber. It is possible to control the equivalence ratio, by operating the combustion in either lean or rich conditions (keep away from the stoichiometric state); hence the temperature of flame can be lower than the threshold temperature. This is preferred in developing low NO$_x$ emission combustors. The premixed combustion, however, suffers from some problems as well.

One problem is flashback. Flashback means the flame propagates through the reactant mixture supply tube and enters the mixture tank without quenching (Turns, 2000). It may result in an explosion. The flashback phenomena happen when the local flow velocity is lower than the local flame speed. Generally, this situation occurs when the fuel flow is decreased or turned off. In addition to this problem, at low power conditions, those general design approaches will result in too lean mixtures, which are not good for ignition and decrease the lean blow-off capability (Bahr, 1999).

At present, many new concepts for combustor design (Lefebvre, 1995) have been proposed. Some of them are described briefly below.

Variable geometry combustor. In this design, the air mass flow, which is used to mix with fuel, is admitted at the upstream, depending on the combustor power setting, to keep the reactants equivalence ratio around a certain value, thus the combustion temperature is maintained in an ideal range. This kind of combustor has the potential of reducing simultaneously all the main pollutants without sacrificing the combustor's performance. Due to this, the variable geometry combustor attracts more attention despite many drawbacks it suffers, which includes the complex control and feedback mechanisms, and operational reliability problem.

Staged combustor. In this combustor, the whole combustor chamber is staged or arranged with several zones or sub-chambers. At low power settings, only one zone works. When power increases, more and more zones come into effect. This allows the combustor to operate over the whole power range while keeping the combustion temperatures within the expected low-emissions window. Depending on the arrangement of the zones, the staged combustors can be classified as radial staging and axial staging.

Rich-burn, Quick-quench, Lean-burn staged combustor. Unlike those lean combustors, which use lean combustion to obtain low combustion temperature hence to suppress the NO_x emissions, the Rich-burn/Quick-quench/Lean-burn (RQL) concept combustor utilizes staged burning. In first staged zone, the combustion is in a fuel-rich state at equivalence ratio between 1.2 and 1.6, thereby reducing NO_x formation by lowering both the available oxygen and flame temperature. This initial rich combustion is also good for suppressing the NO_x formation from fuel-bound nitrogen. As the fuel-rich combustion products flow out of the initial zone, they rapidly mixed with the cold air in the quench mixer (the equivalence ratio reaches between 0.5 and 0.7), and reduce their temperature to a level at which NO_x formation is negligibly small. At last, the lean mixtures burns out in the lean-burn staged zone. The key, to exploit the fully potential of RQL, is the quick quench mixer design. If the transition from the rich zone to lean zone does not take place rapidly, near-stoichiometric mixture fluid group may exist for some long time, and produce much NO_x. Another inherent problem of RQL is the high soot formation in the rich staged zone, which gives rise to problems of exhaust smoke and high level flame radiation.

Catalytic combustor. In catalytic systems, fuel and combustion airflow are mixed upstream of the reactor to provide lean and homogeneous mixtures at the catalyst inlet. Catalytic combustor requires very uniform mixtures at the catalyst inlet. In the catalyst reactor, the catalyst materials, such as platinum or palladium, enhance fuel oxidation that occurs on the reactor substrate surfaces. The catalytic combustion is a 'flameless' kind, which allows the combustion to take place at temperatures well below the normal lean flammability limit; therefore both ultra low NO_x levels and very low UHC and CO levels can be obtained. Additionally, steady combustion with no dynamic pressure instabilities can be obtained even with very lean mixtures. These stability problems are common in many lean combustion burners. The main drawbacks of the catalytic combustors are limited life time of catalysts, and the incomplete fuel oxidation within the reactor.

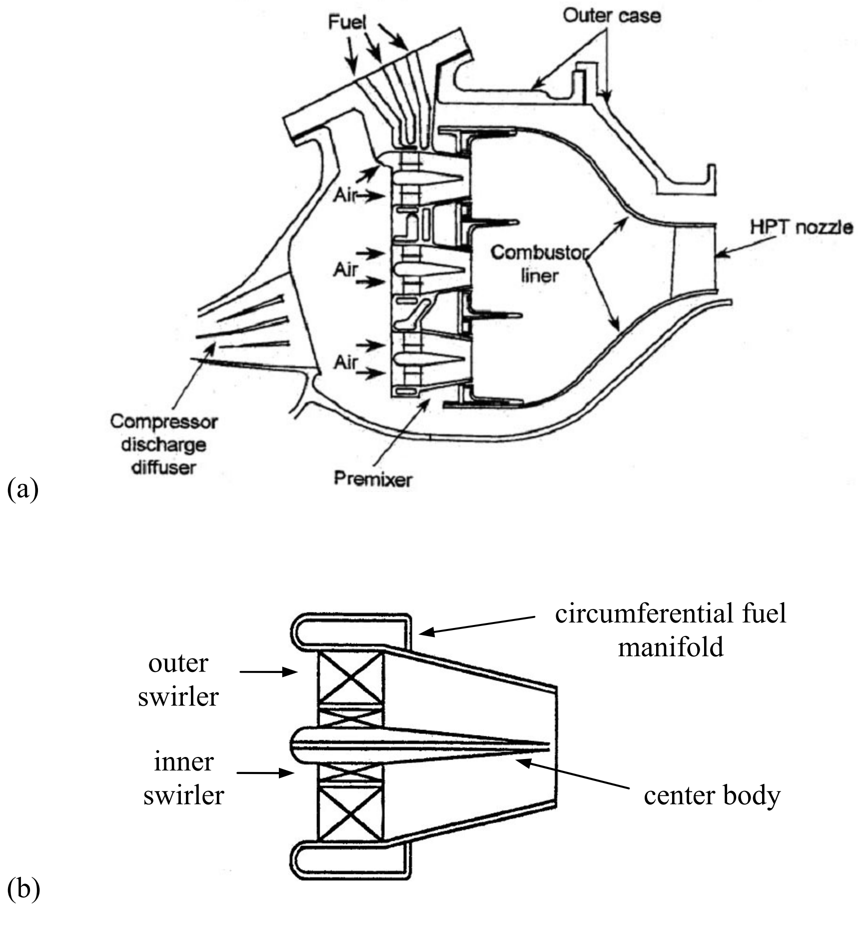

Figure 1.2 Schematic drawing of LM6000 DLE combustor (Gabrielsson & Hermann, 2002) and the premixer module (Bahr, 1999).

Lean premixed prevaporized combustor. This concept combustor operates with much leaner fuel/air mixtures in primary zone. If they use liquid fuels, they are referred to as Lean Premixed/Prevaporized (LPP) combustors. Those which are designed to use gaseous fuels are called as Lean Premixed (LP) combustors. The underlying principle is to supply the primary combustion zone with a completely homogeneous mixture of fuel and air, and the equivalence ratio is very close to the lean blow-off limit. The closer the equivalence ratio to the lean blow-off ratio, the lower will be the output of NO_x, but the combustion will be more unstable. An advantage of LPP/LP combustions is that their ultra low soot formation. This greatly reduces the amount of heat transferred to the wall by radiation, thereby reducing the amount of cooling air. Another advantage of LPP/LP combustors is that for combustion temperature mostly lower than 1900 K the formation of NO_x does not increase with increase of residence time. This is good for obtaining low CO and UHC by increasing residence time. The drawback of LPP/LP system is that the long time needed to achieve complete evaporation and mixing may result in the occurrence of autoignition or flashback in some cases. Another problem is the acoustic resonance. In severe cases, it may cause great damage to the combustor.

Applying these advanced concepts described above, a few dry low NO_x (DLN) or dry low emission (DLE) combustors have been developed successfully. Two examples of these combustors have been made to date: one is the General Electric (GE) LM6000 engine and another is the Asea Brown Boveri (ABB) combustor. They are described in the following.

Figure 1.2 is a schematic drawing of GE's LM6000 DLE combustor (Bahr, 1999; Gabrielsson & Hermann, 2002). The air flows into the combustion chamber through three annular rings of premixers. There are 75 premixer modules in its combustor dome. The outer and middle rings each has 30 while the inner ring has 15. The amount of wall-cooling air is small, since the annular liner is short. The design of premixer modules is of very important to achieve low emissions. Each premixer consists of a counter-rotating inner and outer swirler assembly, a fuel supply manifold. One of the premixers is shown in Figure 1.2(b).

The double annular counter rotation swirler is designed to restrain flashback (Lefebvre, 1995). The duct diameter is reduced at the exit, which creates an accelerating flow and thereby prevents flashback. Liquid or gaseous fuels are supplied through the center body. The design objective of the premixer module is to obtain a completely homogeneous mixture at the premixer exit.

ABB Company has developed a conical premixed combustor module, which is called the EV burner. Figure 1.3 shows the cross-sectional view of the dual fuel EV burner (Strand, 2002). A unique feature is the two offset half cones, which creates two axial air inlet slots. The flame is stabilized in free space near the burner outlet by the sudden breakdown of a swirling flow. The gaseous fuel is injected into the airflow as it enters the half cones. Rapid fuel/air mixing is obtained in the swirling flow. If liquid fuel is used, it is injected into premix cone at the apex of the cone using an atomizer, then evaporates and mixes with air. If needed, water or steam can be injected into the cone for lowering the combustion temperature. Due to the utilization of swirling breakdown to stabilize the flame, no diffusion, pilot stage or mechanical flame holder is needed to improve the stability of the premixed flame.

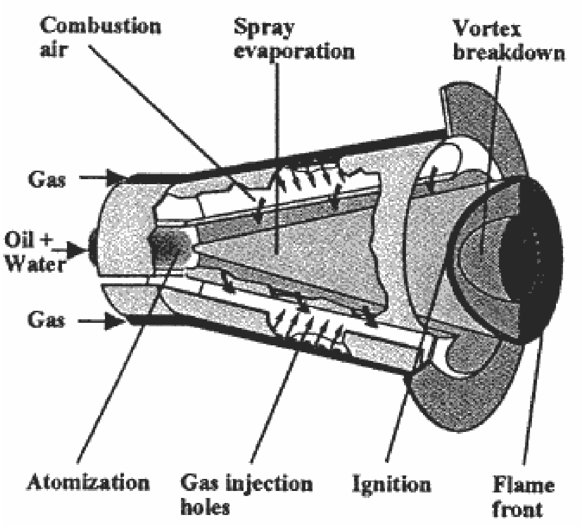

Figure 1.3 Schematic drawing of ABB conical premix dual fuel EV burner module (Strand, 2002).

1.3 Towards understanding of the fundamental combustion process

As discussed above, many advanced combustors have been developed up to date to satisfy the emission limits; however, they are still facing many problems. For example, there are many problems that are related to the lean combustion: lean blow-off, flame stabilization, acoustic resonance, and so on. Considering the future coming more stringent emission limits, the working condition of the combustors will be more rigorous, and the problems will be more serious. To meet this high industry demand, a deeper and better understanding of the physics of the turbulent combustion process is wanted. In doing this, both experimental and computational studies are necessary.

With the rapid development of non-intrusive, optical measuring equipments, many advanced experimental methods are now available. Some of them are briefly described below.

- Coherent Anti-Stokes Raman Scattering (CARS) for temperature measurement.
- Laser Doppler Velocimetry (LDV) for single point velocity measurement.
- Schlieren technique detects gradients in the refractive index (or density) for visualization of flame fronts.
- Particle Image Velocimetry (PIV) for the velocity measurement in a 2D plane.
- Planar Laser-Induced Fluorescence (PLIF) for concentration of radicals and some species, such as CH, OH.
- Raman–Rayleigh scattering technique for mixture fraction, temperature and the concentration of major species.

During the last twenty years, substantial experimental works have been conducted with these non-intrusive optical measuring equipments. They have been proven successful in providing information on turbulence and flame structures, interaction between turbulence and combustion, and have become standard tools in combustion research. For example, Kaminski et al. (2000a; 2000b) used a high-speed PLIF technique to record the evolution of turbulent in real time in a film-like manner, and compared it qualitatively to 2-D DNS and 3-D LES results. Three-dimensional PLIF techniques have also been developed to study the combustion problems (Nygren et al., 2002).

Recently, joint measurements, which apply two or more of these techniques, become attractive. A time resolved PLIF and instantaneous PIV measurements are used simultaneous to study the dynamics of turbulent/chemistry interaction in real time by Hult et al. (2000). Chen et al. (1997) reported an experiment using Rayleigh scattering and laser-induced fluorescence simultaneous in a high speed premixed hydrocarbon flames.

Based on the data obtained using these measuring techniques, a better understanding of the complex physical and chemical mechanisms that govern turbulent combustion can be expected. A recent review of the combustion diagnostic techniques based on laser equipments is given by Kohse-Höinghaus et al. (2004).

The experimental studies, however, suffer from many limitations, such as the time required to design, manufacture, prepare experimental setup, high cost of these setup and measuring equipments, and especially, they can not provide detailed whole-flowfield information. Due to these limitations, the main objectives of the experimental studies are not to help combustor design directly, but to improve the physical understanding of the combustion process and to provide databases for validation or development of the combustion prediction models.

Computational fluid dynamics (CFD), on the other hand, uses computers to simulate or predict the fluid flow by solving differential equations, such as the Navier–Stokes equations. With the rapid development of computer technology and improvement of numerical methods, CFD becomes a more and more important tool in studying flow problems and developing flow related equipments, such as airplanes, motor vehicles, gas turbines, to give just a few examples. Compared to experimental methods, CFD has many advantages: it can simulate most of the flow problems, if suitable models and computation resources are provided; the cost of CFD is lower than corresponding experiment; it can provide detailed flow field information, and so on. There are many successful applications of CFD in the last twenty or thirty years, and recently, many powerful commercial CFD packages are available in the market, such as Fluent, CFX, and StarCD.

1.4 Objectives of this thesis

This thesis deals with numerical modeling of turbulent reactive flows that are related to LP gas turbine combustion applications. It consists of three parts. First, the flow structures of turbulent swirling flows in a dump combustor related geometry are studied; the Reynolds numbers range from 10 000 and 20 000, and the swirl number is varied from 0 to 0.43. The influence of some important factors on the turbulent swirling flows have also been tested, such as the inflow/outflow conditions, viscosity effect, and the inflow swirl velocity profiles. The turbulence structures and large scale coherent flow structures such as precessing vortex core (PVC), are investigated.

Second, the level set *G*-equation, derived in the LES framework, is used to simulate a lean premixed propane/air flame in a jet engine afterburner. The results have been compared to the experimental data. Finally, the effect of subgrid scale eddies on the wrinkling of premixed turbulent flame is studied to investigate the basis of flame/ turbulence interaction.

The main objectives are:

- to study the turbulent swirling flow structures using large eddy simulation (LES).
- to develop simulation models for turbulent premixed combustion based on level set *G*-equation and LES.
- to investigate the mechanisms of flame/eddy interaction using level set approach.
- to validate numerical simulations with the experimental data for swirling flows and premixed combustion processes.

The thesis is organized as follows. In Chapter 2, an overview of the modeling approaches for turbulent reactive flows is presented. Chapter 3 presents the key features of turbulent premixed combustion, the regimes of turbulent premixed, as well as the often used modeling methods. A detailed description of the background of level set *G*-equation, the derivation of it in LES framework, and the flamelet library approach based on *G*-equation, is given in Chapter 4. Chapter 5 presents the numerical methods employed in this thesis work. The results of turbulent swirling flows and turbulent premixed combustion are presented and discussed in Chapter 6 and 7, respectively. Chapter 8 deals with the *h*-equation study of flame/eddy interaction, and Chapter 9 contains a summary of papers and suggestions for future work. An appendix of a glossary lists some abbreviations appeared in this dissertation.

Chapter 2

Mathematic description of turbulent reactive flows

In this Chapter, a review is given on the fundamental aspects of numerical modeling of turbulent combustion process. The important physics behind the turbulent combustion process are outlined. To describe the process in a systematic way, turbulent non-reactive flows are first discussed, followed by reactive flows.

2.1 Turbulence and turbulence modeling

Turbulence is a state of fluid flow in which the instantaneous velocities exhibit irregular and apparently random fluctuations. Most of the flows occurring in nature and in industrial applications are turbulent.

2.1.1 Turbulence properties

Osborne Reynolds was the first one who studied the transition and turbulence in a pipe flow. He found that the onset of transition depends upon a dimensionless parameter, the so-called Reynolds number,

$$Re = \frac{\rho UL}{\mu} = \frac{UL}{\nu} \tag{2.1}$$

It represents the ratio of the diffusion time to the convection time, or the inertial force to the viscous force. In his experiment, Reynolds found that the flow is turbulence when Reynolds number is greater than a critical value, around 2300. It is explained that, at high Reynolds number, the diffusion effect due to the viscous force is much smaller than the inertial force, so it can no longer stabilize the flow and thereby the flow becomes unstable. If the Reynolds number is large enough, the flow finally becomes turbulent. Although, turbulence is not completely understood yet, its important features are quite known to us (Tennekes & Lumley, 1990; Mathieu & Scott, 2000).

- turbulence is a random process
- turbulence contains a wide range of space and time scales at high Reynolds number
- turbulence dissipates energy

- turbulence has random small-scale vorticity
- turbulence occurs at high Reynolds numbers
- turbulence is a continuum phenomenon
- turbulence is intrinsically three-dimensional
- the large scales of turbulence are insensitive to viscosity at high enough Reynolds number

A characteristic property of turbulence is the occurrence of eddies of different scales. Each eddy can be connected to a local value of velocity, length, time scale. In order to characterize the distribution of eddy length scales at any position, one measures the velocity at point (x,t) and a second point $(x+r,t)$ with distance r apart from the first point, and then the correlation between these two points is defined by the average

$$\overline{u'(x,t)u'(x+r,t)} \tag{2.2}$$

For homogeneous isotropic turbulence case, the normalized correlation $f(r,t)$ is

$$f(r,t)=\frac{\overline{u'(x,t)u'(x+r,t)}}{\overline{u'(x,t)u'(x,t)}} \tag{2.3}$$

Figures 2.1 shows schematically the normalized correlation $f(r,t)$ (Peters 2000). It approaches unity for $r\to 0$ and decreases continuously and may even take negative values. Very large eddies corresponding to large distances between the two points are very seldom and they do not contribute much to the correlation.

Among these different scale eddies, there is an energy cascade from large to small turbulent scales, which was first conjectured by Richardson in 1922 (Mathieu & Scott, 2000). Kolmogorov (1941) brought forward a theory for homogeneous isotropic turbulence, i.e. energy cascade hypothesis. It assumes that there is a steady transfer of kinetic energy from the large scales to the small scales and that this energy is being consumed at the small scales by viscous dissipation. When Reynolds number is large enough, there exists a universal equilibrium range, in which the production of turbulent kinetic energy *k*, equals to the dissipation rate ε. The universal equilibrium range can be divided into two subrange, the inertial subrange and viscous subrange.

In inertial subrange, turbulence is affected by neither the real geometry nor the viscous dissipation. ε is the only dimensional quantity apart from the correlation coordinate *r* for the scaling of $f(r,t)$. From the dimensional analysis, the second-order structure function defined by

$$F_2(r,t)=\overline{(u'(x,t)-u'(x+r,t))^2}=2\overline{u'^2(t)}(1-f(r,t) \tag{2.4}$$

which can be scaled as

$$F_2(r,t)=C(\varepsilon r)^{2/3} \tag{2.5}$$

where C is the Kolmogorov constant. In homogeneous isotropic turbulences, the turbulent kinetic energy k is defined as

$$k = 3\overline{u'^2}/2 \tag{2.6}$$

Using this, one obtains from (2.4) and (2.5)

$$f(r,t) = 1 - \frac{3}{4}\frac{C}{k}(\varepsilon r)^{2/3} \tag{2.7}$$

which is also plotted in Figure 2.1.

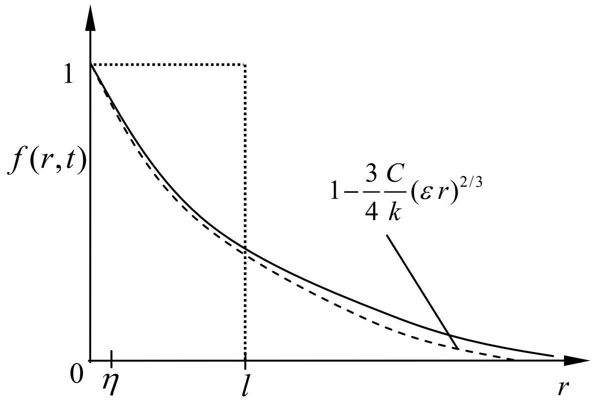

Figure 2.1 The normalized two-point velocity correlation for homogeneous isotropic turbulence.

There are eddies of a characteristic size at which they contain most of the kinetic energy. At these eddies there remains a relative large correlation before it decays to zero. The length scale of these eddies is called the integral length scale l. l is defined by

$$l(t) = \int_0^\infty f(r,t)dr \tag{2.8}$$

It is also shown in Figure 2.1. We denote the characteristic velocity and time scale of the integral length scale eddies by

$$u' = \sqrt{2k/3} \tag{2.9}$$

$$t_l = \frac{k}{\varepsilon} \tag{2.10}$$

In viscous subrange, the motion of these eddies is highly influenced by viscosity, and the turbulent kinetic energy is here transformed into heat by viscous dissipation, therefore the kinematic viscosity, ν (unity: m^2/s), is another dimensional quantity for scaling in addition to the dissipation rate, ε (unity: m^2/s^3). A characteristic length scale for this subrange, which is the so-called Kolmogorov length scale, η, as well as its time scale t_η and velocity scale u_η, are determined by dimensional analysis. The Kolmogorov length scale, η, is also shown in Figure 2.1.

$$\eta = \left(\frac{\nu^3}{\varepsilon}\right)^{1/4}, \qquad t_\eta = \left(\frac{\nu}{\varepsilon}\right)^{1/2}, \qquad u_\eta = (\nu\varepsilon)^{1/4} \tag{2.11}$$

Between the integral scale and the Kolmogorov scale, a Taylor length scale, λ, is defined. From the definition of ε, one has

$$\varepsilon = \nu\overline{\frac{\partial u_i'}{\partial x_j}\frac{\partial u_j'}{\partial x_i}} \tag{2.12}$$

By replacing the average gradient in the definition by u'/λ, it is found

$$\varepsilon = 15\nu\frac{u'^2}{\lambda^2} \tag{2.13}$$

Factor 15 is due to the assumption that the turbulence is isotropic homogeneous (Peters, 2000; Mathieu & Scott, 2000). Using (2.13), we obtain that λ is proportional to $u't_\eta$

$$\lambda = (15\nu u'^2/\varepsilon)^{1/2} \sim u't_\eta \tag{2.14}$$

Taylor scale, λ, may be interpreted as the distance that a large eddy convects a Kolmogorov eddy during its turnover time t_η.

In Kolmogorov's theory, it is assumed that the energy transferred from the large eddies of integral length scale, *l*, is in equilibrium with the energy dissipation at the Kolmogorov scale, η, thus, the viscous dissipation can be estimated by

$$\varepsilon \sim \frac{u'^3}{l} \tag{2.15}$$

Within the inertial subrange, the dissipation rate ε is independent of the size of eddies. We define a discrete sequence of eddies (Peters, 2000) by

$$l_n = \frac{l}{2^n} \geq \eta, \quad \text{n=1, 2...} \tag{2.16}$$

The kinetic energy spectrum $E(\kappa)$, which is the density of kinetic energy per unit wave-number κ, can be obtained from the Fourier transform of the isotropic two-point correlation function. Here, we relate the wavenumber κ to the inverse of the eddy size as

$$\kappa \sim l_n^{-1} \tag{2.17}$$

Then, the kinetic energy at the discrete scale l_n is estimated as

$$u_n^2 \sim (\varepsilon l_n)^{2/3} = \varepsilon^{2/3}\kappa^{-2/3} \tag{2.18}$$

From the definition, the kinetic energy spectrum $E(\kappa)$ is proportional to

$$E(\kappa) = \frac{du_n^2}{d\kappa} \sim \frac{d\varepsilon^{2/3}\kappa^{-2/3}}{d\kappa} \sim \varepsilon^{2/3}\kappa^{-5/3} \tag{2.19}$$

This is the well-known –5/3 law for the kinetic energy spectrum in the inertial subrange. Figure 2.2 is a typical schematic drawing of the energy spectrum as a function of the wavenumber, which drawn in log–log system. The small wavenumbers represent the large scale eddies, at which the energy spectrum is not universal and depends on the local geometry condition. Around the integral length scale, energy spectrum reaches maximum, thus, these eddies contain most of the kinetic energy. Increasing wavenumber further, these eddies fall into the inertial subrange, and the energy spectrum decrease follows the –5/3 law. Near the Kolmogorov length scale, the energy spectrum decreases exponentially due to the dominant viscous effects.

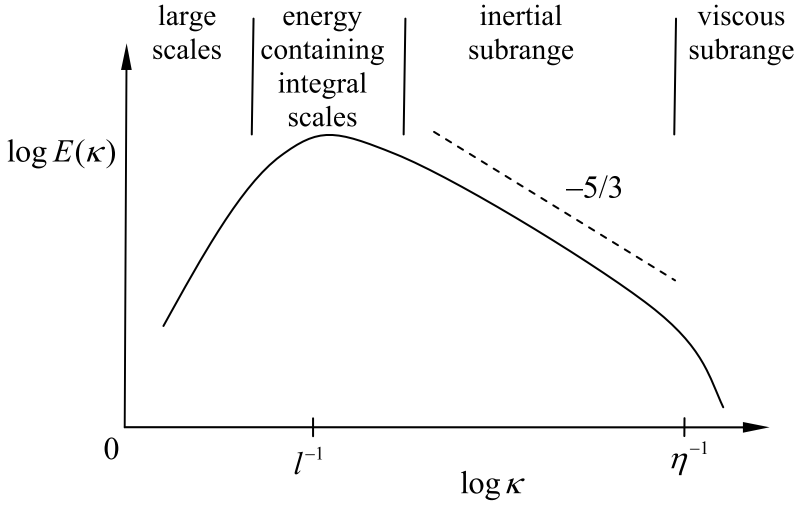

Figure 2.2 Turbulent kinetic energy spectrum as a function of wavenumber κ.

By using dimensional analysis, important relations can be established between the integral scale and Kolmogorov scale.

$$\frac{l}{\eta} = \frac{\varepsilon^{1/4} l}{\nu^{3/4}} \sim \frac{u'^{3/4} l}{\nu^{3/4} l^{1/4}} = \left(\frac{u'l}{\nu}\right)^{3/4} = Re_l^{3/4} \tag{2.20}$$

$$\frac{t_I}{t_\eta} = \frac{l}{u' t_\eta} = \frac{l\varepsilon^{1/2}}{u'\nu^{1/2}} \sim \frac{l u'^{3/2}}{u'\nu^{1/2} l^{1/2}} = \left(\frac{u'l}{\nu}\right)^{1/2} = Re_l^{1/2} \tag{2.21}$$

$$\frac{u'}{u_\eta} = \frac{u'}{(\nu\varepsilon)^{1/4}} \sim \frac{u' l^{1/4}}{\nu^{1/4} u'^{3/4}} = \left(\frac{u' l}{\nu}\right)^{1/4} = Re_l^{1/4} \tag{2.22}$$

where $Re_l = u'l/\nu$ is the so called turbulent Reynolds number defined at the integral scale. From (2.14), the relation between the integral length scale and Taylor length scale is also obtained as

$$\frac{l}{\lambda} \sim \frac{l}{u' t_\eta} = \frac{l}{u'} \frac{u_\eta}{\eta} \sim Re_l^{3/4} Re_l^{-1/4} = Re_l^{1/2} \tag{2.23}$$

2.1.2 Reynolds averaged Navier–Stokes equations

Due to the random property of turbulence, the statistical method is a useful method to study it. The classical approach to model turbulent flows is based on single point averages of the Navier–Stokes equations, which is the so-called Reynolds averaged Navier–Stokes (RANS) equations. Reynolds was the first one to decompose the turbulent variables into a mean value and a fluctuating value.

To obtain the mean value, many methods can be used, such as time average, space average, ensemble average and weighted average. In time average approach, the time averaged mean value of quantity ϕ is

$$\overline{\phi} = \lim_{T\to\infty} \frac{1}{T} \int_{t_0}^{t_0+T} \phi(x,y,z,t)dt \tag{2.24}$$

In order to get an appropriate averaged quantity, the time interval T should be much longer than all the time scales of the turbulent flow. Then, the time dependent quantity ϕ is decomposed as

$$\phi(t) = \overline{\phi} + \phi'(t) \tag{2.25}$$

where ϕ' is the fluctuating part. The mean of this fluctuating part is zero, according to

$$\begin{aligned} \overline{\phi'} &= \lim_{T\to\infty} \frac{1}{T} \int_{t_0}^{t_0+T} \left(\phi(x,y,z,t) - \overline{\phi(x,y,z,t)}\right) dt \\ &= \overline{\phi(x,y,z,t)} - \overline{\phi(x,y,z,t)} \equiv 0 \end{aligned} \tag{2.26}$$

In nonconstant density flow problems, such as compressible flows and reactive flows, if one applies above time averaging method to the Navier–Stokes equations, some terms containing ρ' arise, such as $\overline{\rho' u'}$. To avoid these terms and simplify the problem, a density weighted averaging procedure, which is the so-called Favre averaging, is applied. The definition of density weighted averaging on variable ϕ is

$$\tilde{\phi} = \frac{\overline{\rho\phi}}{\overline{\rho}} \tag{2.27}$$

and the decomposition of quantity ϕ is

$$\phi = \tilde{\phi} + \phi'' \tag{2.28}$$

$\tilde{\phi}$ is the density weighted mean value, and ϕ'' is the fluctuation term. From the definition, it is found that

$$\overline{\rho\phi''} = \overline{\rho(\phi - \tilde{\phi})} = \overline{\rho\phi} - \overline{\rho}\tilde{\phi} = \overline{\rho}\tilde{\phi} - \overline{\rho}\tilde{\phi} \equiv 0 \tag{2.29}$$

For nonconstant density flows, the governing equations in conservative form are written in:

Continuity: $$\frac{\partial \rho}{\partial t} + \frac{\partial \rho u_j}{\partial x_j} = 0 \tag{2.30}$$

Momentum: $$\frac{\partial \rho u_i}{\partial t} + \frac{\partial \rho u_i u_j}{\partial x_j} = -\frac{\partial P}{\partial x_i} + \frac{\partial t_{ij}}{\partial x_j} \tag{2.31}$$

where t_{ij} is the molecular viscous stress tensor

$$t_{ij} = \mu(2S_{ij} - \tfrac{2}{3}\delta_{ij}\frac{\partial u_k}{\partial x_k}) \tag{2.32}$$

S_{ij} is the strain rate tensor by

$$S_{ij} = \frac{1}{2}(\frac{\partial u_i}{\partial x_j} + \frac{\partial u_j}{\partial x_i}) \tag{2.33}$$

Applying the Favre averaging on (2.30) and (2.31), we obtain

$$\frac{\partial \overline{\rho}}{\partial t} + \frac{\partial \overline{\rho}\tilde{u}_j}{\partial x_j} = 0 \tag{2.34}$$

$$\frac{\partial \overline{\rho}\tilde{u}_i}{\partial t} + \frac{\partial \overline{\rho}\tilde{u}_i\tilde{u}_j}{\partial x_j} = -\frac{\partial \overline{P}}{\partial x_i} + \frac{\partial \overline{t_{ij}}}{\partial x_j} - \frac{\partial}{\partial x_j}\left(\overline{\rho u_i'' u_j''}\right) \tag{2.35}$$

where $\overline{t_{ij}}$ is the averaged molecular viscous stress tensor

$$\overline{t_{ij}} = \mu(2\tilde{S}_{ij} - \tfrac{2}{3}\delta_{ij}\frac{\partial \tilde{u}_k}{\partial x_k}) \tag{2.36}$$

$$\tilde{S}_{ij} = \frac{1}{2}(\frac{\partial \tilde{u}_i}{\partial x_j} + \frac{\partial \tilde{u}_j}{\partial x_i}) \tag{2.37}$$

The averaged continuity equation (2.34) is similar to the original one (2.30), but in the averaged momentum equation (2.35), an unclosed correlation term, $-\overline{\rho u_i'' u_j''}$ is present and has to be modeled. This term is the so-called Reynolds stresses tensor.

The simplest turbulence models are based on the Boussinesq eddy-viscosity hypothesis. Boussinesq modeled the Reynolds stresses as the product of an equivalent turbulent eddy viscosity μ_t, and the mean strain-rate tensor, in analogy to the viscous stress tensor (2.36). So, the problem turns to how to calculate the turbulent eddy viscosity μ_t.

$$-\overline{\rho u_i'' u_j''} = \mu_t (2\tilde{S}_{ij} - \frac{2}{3}\delta_{ij}\frac{\partial \tilde{u}_k}{\partial x_k}) - \frac{2}{3}\delta_{ij}\bar{\rho}k \tag{2.38}$$

The last term is needed in order to fulfill $-\overline{\rho u_i'' u_i''} = -2\bar{\rho}k$.

Models originated from the Boussinesq eddy-viscosity hypothesis, however, suffer from some inherent drawbacks (Wilcox, 1998). First, the modeled Reynolds stresses follows immediately the mean strain rate tensor change without any delay, which means no history effect is taken into account. Second, it can not account for those extra rates of strain, for example, produced by rotation movement, since the strain rate tensor $\tilde{S}_{ij}$ is symmetric, whereas the rotation tensor $\tilde{\Omega}_{ij}$ is anti-symmetric, where the $\tilde{\Omega}_{ij}$ is defined as

$$\tilde{\Omega}_{ij} = \frac{1}{2}(\frac{\partial \tilde{u}_i}{\partial x_j} - \frac{\partial \tilde{u}_j}{\partial x_i}) \tag{2.39}$$

For these reasons, the turbulence models based on the Boussinesq hypothesis are known not to be suitable (Wilcox, 1998) for: flow with sudden changes in mean strain rate; flow over curved surfaces; flow in ducts with secondary motions; flow in rotating; flow with boundary-layer separation, and in general for non-isotropic flows.

Although they are suffered from many drawbacks, those Boussinesq hypothesis based models are still widely used in many cases. This is mainly due to its simplicity, low computation load compared with larger eddy simulation (LES) and direct numerical simulation (DNS), and easily handled by numerical methods.

Many Boussinesq hypothesis based models have now been developed to estimate the turbulent eddy viscosity μ_t, which appears in (2.38). From dimensional analysis, μ_t is calculated according to

$$\mu_t = C_\mu \bar{\rho} u^* l^* \tag{2.40}$$

where C_μ is a constant, u^* is a turbulent velocity scale and l^* is a turbulent length scale.

- **Zero-equation model**

These models are also called algebraic model. They use algebraic expressions to calculate u^* and l^*, therefore no transport equation is needed. These models are only suitable for very limited cases, which are simple and well documented, for example, jet flows, mixing layer flows. Examples of this kind model include Prandtl mixing length model (Prandtl, 1925), Cebeci–Smith model (Smith & Cebeci, 1967), and Baldwin–Lomax model (Baldwin & Lomax, 1978).

- **One-equation model**

  In this kind model, a transport equation for one turbulent scale, usually the turbulent kinetic energy *k*, is solved, while another scale is estimated by algebraic expression. For example, if the equation for turbulent kinetic energy *k* is solved, then the turbulent velocity scale u^* can be estimated by

$$u^* \sim \sqrt{k} \tag{2.41}$$

  and the turbulent eddy viscosity is

$$\mu_t = C_\mu \bar{\rho} k^{1/2} l^* \tag{2.42}$$

  Many applications have shown that only a modest advantage is obtained in using one-equation model rather than zero-equation model, thus it is not commonly used (Wilcox, 1998). Baldwin–Barth model (Baldwin & Barth, 1990) and Spalart–Allmaras model (Spalart & Allmaras, 1992) are two examples of this kind model.

- **Two-equation model**

  This kind model solves not only a *k* equation, but also an equation for the turbulent length scale or equivalent. Contrary to the zero- and one-equation model, it is complete, i.e. it can be used to calculate a given turbulent flow without prior knowledge of the turbulence structure. The two transport equations contain many closure coefficients which have to be tuned from case to case. Depending on the way how to calculate the turbulent length scale, many kinds two-equation model have been developed, such as $k-\omega$ (Kolmogorov, 1942; Launder & Spalding, 1972), $k-\tau$ (Speziale et al., 1990), and $k-\varepsilon$ (Jones & Launder, 1972; Launder & Sharma, 1974) model.

  A $k-\varepsilon$ model for reacting flows was proposed by Jones and Whitelaw (1982), where two equations are solved

$$\frac{\partial \bar{\rho} k}{\partial t} + \frac{\partial \bar{\rho} \tilde{u}_j k}{\partial x_j} = -\bar{\rho} \widetilde{u_i'' u_j''} \frac{\partial \tilde{u}_i}{\partial x_j} - \bar{\rho}\varepsilon + \frac{\partial}{\partial x_j}((\mu + \frac{\mu_t}{Pr_k})\frac{\partial k}{\partial x_j}) - \frac{\mu_t}{\bar{\rho}^2}\frac{\partial \bar{\rho}}{\partial x_i}\frac{\partial \bar{P}}{\partial x_i} \tag{2.43}$$

$$\begin{aligned} \frac{\partial \bar{\rho} \varepsilon}{\partial t} + \frac{\partial \bar{\rho} \tilde{u}_j \varepsilon}{\partial x_j} = {} & -C_{\varepsilon 1} \frac{\varepsilon}{k} (\bar{\rho} \widetilde{u_i'' u_j''} \frac{\partial \tilde{u}_i}{\partial x_j} + \frac{\mu_t}{\bar{\rho}^2}\frac{\partial \bar{\rho}}{\partial x_i}\frac{\partial \bar{P}}{\partial x_i}) \\ & + \frac{\partial}{\partial x_j}((\mu + \frac{\mu_t}{Pr_\varepsilon})\frac{\partial \varepsilon}{\partial x_j}) - C_{\varepsilon 2}\bar{\rho}\frac{\varepsilon^2}{k} \end{aligned} \tag{2.44}$$

where Pr_k=1.0, Pr_ε=1.3, $C_{\varepsilon 1}$=1.44, $C_{\varepsilon 2}$=1.92. These coefficients are determined by experimental ‘calibration’. The turbulent eddy viscosity μ_t, in (2.38) is then calculated by

$$\mu_t = C_\mu \bar{\rho} k^2 / \varepsilon \tag{2.45}$$

Model constant C_μ is 0.09.

Reynolds stress model (RSM)

One can derive transport equations for the six components of Reynolds stress tensor in (2.35). However, there will be 22 new unknowns in the derived six new equations (Wilcox, 1998), and all of these unknown terms have to be modeled in some way (Launder et al., 1975). This is the so-called RSM, which is a *second-order closure* or *second-moment closure* model. It has several gains compared with Boussinesq hypothesis based RANS models. It automatically accounts for the convection and diffusion of Reynolds stress tensor, so the flow history effects are considered. It can respond automatically to effects of streamline curvature, system rotation, and so on. Although RSM give a more complete description of the physics, they are not yet widely used, due to its complexity and computational difficulty.

To overcome those drawbacks suffered from the Boussinesq hypothesis based RANS models, one may use nonlinear constitutive relations and without introducing extra differential equations (Wilcox, 1998). For example, Wilcox and Rubesin (1980) propose a nonlinear constitutive relation for their $k-\omega^2$ model,

$$-\overline{\rho u_i'' u_j''} = \mu_t (2\tilde{S}_{ij} - \frac{2}{3}\delta_{ij}\frac{\partial \tilde{u}_k}{\partial x_k}) - \frac{2}{3}\delta_{ij}\bar{\rho}k + \frac{8}{9}\frac{\rho k(\tilde{S}_{ik}\tilde{\Omega}_{kj} + \tilde{S}_{jk}\tilde{\Omega}_{ki})}{(\beta^* \omega^2 + 2\tilde{S}_{mn}\tilde{S}_{nm})} \tag{2.46}$$

Compared with the (2.38), a second order correcting term is added. Rodi (1976) deduced a nonlinear constitutive relation by simplifying the full RSM equations. A model derived in this manner is called algebraic stress model (ASM or ARSM). Johansson and Wallin (1996) proposed an explicit algebraic Reynolds stress turbulence model (EARSM), and later, some new developments are presented in Wallin and Johansson (2000).

2.1.3 Large eddy simulation

LES is a method in which the large eddies of turbulence are explicitly computed whereas the small eddies are modeled. It has several advantages over the RANS models. Since the small eddies contain less turbulent kinetic energy, have a more like universal behavior, and are more isotropic, it is relatively easier to model the small eddies than to model the full spectrum. The direct time-unsteady calculation of those large eddies, which are affected by the flow geometry and boundary conditions significantly, leads to a more high fidelity representation of the flow structure than that from RANS.

In LES, the variables are filtered in spectral space (eddies with a wavenumber greater than the cut-off wavenumber are filtered out) or in physical space (weighted volume averaging). Here, only space filtering is described, and more detailed information about spectral filtering and filter functions can be found in Piomelli (1999). In space filtering, filter function F with the filter width Δ is applied to a flow variable ϕ to obtain a filtered flow variable $\overline{\phi}$, by

$$\overline{\phi}(x,t;\Delta)=\int_{-\infty}^{+\infty}F(x-x';\Delta)\,\phi(x',t)dx' \tag{2.47}$$

The filter function F should fulfill the normalization condition

$$\int_{-\infty}^{+\infty}F(x-x';\Delta)\,dx'=1 \tag{2.48}$$

The filtered quantity $\overline{\phi}$ is resolved in computation whereas $\phi'=\phi-\overline{\phi}$ is the unsolved subgrid scale part. For nonconstant density flow, a Favre filtering is introduced as in (2.27). The LES filtering process has some properties contrary to RANS averaging, such as $\overline{\phi'}\neq 0$, and $\overline{\overline{\phi}}\neq\overline{\phi}$. For Favre filtering also: $\phi=\tilde{\phi}+\phi''$, $\widetilde{\phi'}\neq 0$, and $\tilde{\tilde{\phi}}\neq\tilde{\phi}$.

Applying the filtering procedure to the governing equations (2.30) and (2.31), the governing equations become:

$$\frac{\partial\overline{\rho}}{\partial t}+\frac{\partial\overline{\rho}\tilde{u}_j}{\partial x_j}=0 \tag{2.49}$$

$$\frac{\partial\overline{\rho}\tilde{u}_i}{\partial t}+\frac{\partial\overline{\rho}\tilde{u}_i\tilde{u}_j}{\partial x_j}=-\frac{\partial\overline{P}}{\partial x_i}+\frac{\partial\overline{t_{ij}}}{\partial x_j}-\frac{\partial\tau_{ij}}{\partial x_j} \tag{2.50}$$

where $\overline{t_{ij}}$ is the filtered molecular viscous stress tensor, has a similar form as (2.36). The term, $\tau_{ij}=\overline{\rho}\widetilde{u_iu_j}-\overline{\rho}\tilde{u}_i\tilde{u}_j$ is an unclosed term, and traditionally, it is called the subgrid scale (SGS) stress tensor. Katopodes et al. (2000) and Chow and Moin (2003) proposed to call this term as subfilter scale (SFS), due to the fact that the smallest resolved eddy scale is always in the order of filter scale and greater than grid size. In this work, however, we would like to call it SGS as to follow the tradition.

Different SGS models have been proposed and tested in the literature. Piomelli (1999) summarized the main models developed till today. The main role of SGS model is to dissipate the energy transferred from large scales, since the viscous subrange in the turbulent kinetic energy spectrum are usually unresolved (Piomelli, 1999). Three popular used SGS model are briefly described below.

- **Smagorinsky model**

Smagorinsky model is one of the first models, and is still widely used these days because of its simple formulation and good numerical performance (Smagorinsky, 1963). It is an eddy-viscosity based model, in analogy to the concepts developed in RANS. It has the form

$$\tau_{ij} - \frac{1}{3}\delta_{ij}\tau_{kk} = -2\mu_t \tilde{S}_{ij} \tag{2.51}$$

where $\tilde{S}_{ij}$ is the filtered strain rate tensor having a similar form as (2.37). The eddy-viscosity model proposed by Smagorinsky is

$$\mu_t = C\bar{\rho}\Delta^2 (2\tilde{S}_{kl}\tilde{S}_{kl})^{1/2} \tag{2.52}$$

where C is a model constant. The drawbacks of this model are that the model constant C needed to be tuned from case to case and it is too dissipative. Additionally, it does not take into account the back-scatter phenomenon that is important for some cases, such as transition problem (Lesieur & Métais, 1996; Meneveau & Katz, 2000).

- **Stress similarity model (SSM)**

  Bardina et al. (1980) proposed a model based on the assumption that the unresolved stresses are dominant by those largest unresolved eddies, which are similarly to the smallest resolved eddies. The contribution from the smallest resolved eddies can be estimated by applying filtering process on the resolved scales. The expression for this model is

  $$\tau_{ij} = \bar{\rho}\widetilde{\tilde{u}_i\tilde{u}_j} - \bar{\rho}\tilde{\tilde{u}}_i\tilde{\tilde{u}}_j \tag{2.53}$$

  This mode was found not to be dissipative enough, so Bardina et al. (1980) suggested that a mixed model should be used. Liu et al. (1994) proposed a SSM model using a second filtering function, and also a linear combination with the Smagorinsky model is need to provide enough dissipation of turbulent kinetic energy, as

  $$\tau_{ij} = C_L\bar{\rho}(\widehat{\tilde{u}_i\tilde{u}_j} - \bar{\rho}\hat{\tilde{u}}_i\hat{\tilde{u}}_j) - C\bar{\rho}\Delta^2(2\tilde{S}_{kl}\tilde{S}_{kl})^{1/2}2\tilde{S}_{ij} \tag{2.54}$$

  Gullbrand et al. (2001) and Wang et al. (2004a; 2005) utilize the dissipative character of the numerical scheme to replace the Smagorinsky model used in (2.54), whereby the excessive dissipativity of the Smagorinsky model is remedied.

- **Dynamic model**

  Germano et al. (1991) proposed a dynamic SGS model to improve the Smagorinsky model. In the dynamic model, the model constant is recalculated during the simulations and not a pre-determined constant anymore. The SGS stresses tensors $\tau_{ij} = \bar{\rho}\widetilde{u_iu_j} - \bar{\rho}\tilde{u}_i\tilde{u}_j$ can be modeled in a form

$$\tau_{ij} - \frac{1}{3}\delta_{ij}\tau_{kk} = C\alpha_{ij} \tag{2.55}$$

where C is a model parameter and α_{ij} is a term that needs to be modeled. Appling a second filter function to the filterer momentum equation (2.50), a similar expression is achieved for the new sub-test scale (STS) stress tensor that is defined by $T_{ij} = \hat{\bar{\rho}}\widehat{u_i u_j} - \hat{\bar{\rho}}\hat{\tilde{u}}_i\hat{\tilde{u}}_j$. In the same way, it can be modeled as

$$T_{ij} - \frac{1}{3}\delta_{ij}T_{kk} = C\beta_{ij} \tag{2.56}$$

where β_{ij} must be modeled. Germano et al. (1991) assumed that the same form can be used to model both α_{ij} and β_{ij}, for example, in Smagorinsky form

$$\alpha_{ij} = -2\bar{\rho}\Delta^2(2\tilde{S}_{kl}\tilde{S}_{kl})^{\frac{1}{2}}\tilde{S}_{ij} \tag{2.57}$$

$$\beta_{ij} = -2\hat{\bar{\rho}}\hat{\Delta}^2(2\hat{\tilde{S}}_{kl}\hat{\tilde{S}}_{kl})^{\frac{1}{2}}\hat{\tilde{S}}_{ij} \tag{2.58}$$

Germano et al. found that there is an identity between the SGS and STS stress tensor, that is

$$L_{ij} = \hat{\bar{\rho}}\widehat{\tilde{u}_i\tilde{u}_j} - \hat{\bar{\rho}}\hat{\tilde{u}}_i\hat{\tilde{u}}_j = T_{ij} - \hat{\tau}_{ij} \tag{2.59}$$

It is seen that the L_{ij} is a resolved stress tensor. Substitute (2.55) and (2.56) into (2.59), a system of equation for determining C is obtained

$$L_{ij} - \frac{1}{3}\delta_{ij}L_{kk} = C(\beta_{ij} - \widehat{\alpha_{ij}}) \tag{2.60}$$

This equation system consists of six equations with one unknown, so it is over determined. Some averaging ways or optimization procedures have to be used to calculate C. One method is by using the least square technique. Defining an error as

$$Q = (L_{ij} - \frac{1}{3}\delta_{ij}L_{kk} + CM_{ij})^2 \tag{2.61}$$

where $M_{ij} = (\widehat{\alpha_{ij}} - \beta_{ij})$. The minimum error corresponds to $\partial Q/\partial C = 0$. Using this condition, C is obtained by

$$C = -\frac{L_{ij}M_{ij}}{M_{kl}M_{kl}} \tag{2.62}$$

Dynamic model seems to be very efficient in many applications, for example, Moin et al. (1991) used this dynamic model to simulate compressible flows and scalar transport problem.

2.1.4 Direct numerical simulation

In DNS, the flow field is fully resolved and hence no models are required. To obtain a complete description of turbulence, it is required to resolve all the scale of turbulence, from the integral length scale to the smallest Kolmogorov length scale, as well as the time scales, thus the time step and grid size used should be very fine. DNS is known as ‘numerical experiment’ because its ability to provide complete flowfield information without any modeling. The role of DNS in turbulent combustion studies has been discussed by Poinsot and Veynante (2001).

One inherent drawback of DNS is its requirement for very large amount of computational resources. Additionally, high order discretization schemes are wanted to reduce the numerical error in the solution of the governing equations. Attention is also needed to pay on providing turbulence boundary. Until now, DNS is only applied to moderate Reynolds numbers and simple geometry.

2.2 Combustion and combustion modeling

2.2.1 Governing equations for reacting flows

In combustion process, many species and chemical reactions are involved. To numerically simulate the combustion cases, a system of species transport equations have to be solved in addition to the N–S equations for the flow field. Denote the mass fraction of species *k* with Y_k ($k = 1, ..., N$), where *N* is the number of species involved, then transport equation for species *k* can be derived as

$$\frac{\partial \rho Y_k}{\partial t} + \frac{\partial \rho Y_k u_i}{\partial x_i} = \frac{\partial}{\partial x_i}(D_k \rho \frac{\partial Y_k}{\partial x_i}) + \omega_k \tag{2.63}$$

where ω_k is formation rate of species *k*, it is calculated as summation of formation rates from total *M* elementary chemical reactions

$$\omega_k = W_k \sum_{l=1}^{M} \upsilon_{kl} Q_l \tag{2.64}$$

The rate of reaction *l*, Q_l is

$$Q_l = r_l^f \prod_{k=1}^{N} (\frac{\rho Y_k}{W_k})^{\upsilon_{kl}^f} - r_l^b \prod_{k=1}^{N} (\frac{\rho Y_k}{W_k})^{\upsilon_{kl}^b} \tag{2.65}$$

W_k is the molecular weight of species *k*. υ_{kl}^f and υ_{kl}^b are the stoichiometric coefficients in reaction *l* of the *M* chemical reactions for species k in the forward and backward reactions respectively. Here $\upsilon_{kl} = \upsilon_{kl}^b - \upsilon_{kl}^f$. r_l^f and r_l^b are rate constants of the forward and backward reaction, respectively. They are temperature dependent, and usually calculated using the three-parameter empirical Arrhenius expression (Turns, 2001):

$$r_l^f = A_l^f T^b \exp(-E_l / RT) \tag{2.66}$$

where A_l^f is the preexponential constant, b is the temperature exponent, R is universal gas constant, and E_l is the activation energy.

In deriving (2.63), the diffusive flux in the first term on the r.h.s. is simplified based on Fick's law. The molecular transport process that causes the diffusive flux, however, is very complex. Detailed description can be found in Williams (1985b).

2.2.2 Different modeling approaches

Before conducting a numerical calculation, the species, reactions and chemical kinetics parameters should be provided. A fact is that this information is mostly obtained experimentally and values of the kinetic parameters are often disputed in the kinetics community, and maybe evolved or updated over time (Just, 1994). An example is the Methane chemical kinetic. In the period around 1970, it consisted of less than 15 elementary reactions with 12 species. Up to now, it has evolved to 49 species and 277 elementary reactions in the GRI mechanism, available on the internet (http://www. me.berkeley.edu/ gri_mech/). For more complex fuel, the numbers of the species and elementary reaction are even larger. Due to this, a large amount computation resource is required to apply full reaction kinetics.

In detailed numerical modeling (DNM), full or detailed kinetics are taken into account to study flame structures, ignition and extinction conditions, and instabilities. But this modeling is only affordable for very simple flow configurations, such as plane, cylindrical or spherical flames. DNM is usually used to calculate flamelet libraries for many turbulent combustion models, and to provide test databases for reducing complex reaction mechanism.

One way to solve this problem is to simplify the kinetic mechanism without losing the more important part of the chemical information contained in it. In Peters (1985), a four-step global reduced mechanism for methane-air combustion system is proposed by using steady state and partial equilibrium assumptions. This four-step mechanism is further reduced to three steps by assuming the radical H is in steady state (Peters & Williams, 1987). Later, Bui–Pham et al. (1992) developed a two-steps mechanism further by introduced the steady state assumption for H_2. These reduced mechanisms enhance computation efficiency dramatically, and at the same time give good predictions of burning velocity, flame structure, and so on. For other hydrocarbon fuels and hydrogen flames, similar analyses have been performed by Mauss et al. (1993a; 1993b) and Løvås et al. (2000; 2002). Based on an analysis of flame structures, Jones and Lindstedt (1988) proposed a four-step reaction mechanism, for the combustion of alkane hydrocarbons up to butane. Further information on mechanism reduction can be found in Westbrook and Dryer (1981), Peters (1985), and Seshadri (1996).

Even with these reduced reaction mechanisms, DNS of the turbulent combustion still requires large amount computation resourced, because of the complexity of turbulence and combustion themselves, and the not well-understood mechanisms between them. In DNS, one has to account for all the length scales extending form the Kolmogorov scale to the integral scale in addition to the length- and time-scales that are associated with the flame. The accessible range for DNS of turbulent combustion is not only dependent on the Reynolds number but also on other parameter in combustion, such as the Damköhler number. Detailed description about the DNS of turbulent premixed and diffusion combustion can be found in Poinsot et al. (1996), Candel et al. (1999), and Vervisch and Poinsot (1998). Currently, DNS of reacting flows implies only that one resolves the turbulent scales and handles the other scales, related to the flame, by using simplified models. Hence, using reacting flow DNS as a reference 'truth', has to be taken with some caution.

DNS is usually used to study flame interaction with turbulence and to validate and improve turbulence combustion models. Due to the limitation of computation resources, many DNS have to use simple chemical mechanism and simple transport schemes. In Poinsot et al. (1991; 1990), DNS is used to study flame quenching and the interaction of flame vortex. The important edge-flame (or the so-called triple flame) phenomenon has also been studied using DNS by Domingo and Vervisch (1996).

Although important advances have been achieved in kinetic model reduction, it is necessary to keep a fact in mind that any reduced reaction mechanism is only faithful to the full mechanism over a limited range of conditions. The real combustion conditions (e.g. temperature, composition) vary much in both space and time. Schwer et al. (2003) proposed an adaptive reaction method, in which several reduced reaction mechanism are used in the same simulation. Only one reduced model which is the most suitable to the local condition is used locally. It is hoped that it can accurately reproduce the full chemistry solutions, while reducing the cost of the computation both in terms of CPU time and in terms of memory requirements. The key to realize adaptive chemistry is how to define the appropriate reduced chemistry models for different conditions within the flame, and how to define feasible criteria for switching between chemistry models.

Two simple flames have been tested in Schwer et al. (2003). One of them is the H_2/O_2 shear layer diffusion flame. The full reaction mechanism consists of 12 species and 23 reactions. Two reduced models are derived to account for the hydrogen-rich and oxygen-rich conditions. Both models are valid only below temperature 1500 K. Additionally, pure O_2/N_2 and H_2/N_2 models without reaction are also used. The switching criteria are the temperature and the hydrogen and oxygen mass fractions. It is shown that the full mechanism is only necessary in a rather small region around the shear layer, whereas large areas are computed with reduced models. The agreement between the full chemistry and adaptive chemistry solutions is quite good. With adaptive chemistry, 60% CPU time is saved. It is believed that, if more complex combustion cases are considered, the benefit of using adaptive chemistry will be even bigger.

2.2.3 Modeling of mean reaction rate

Because of the prohibitive requirement for the computation resources, simulations of turbulent combustion of practical system usually require to apply averaging to the governing equations, then to model all the unclosed terms. For example, applying Favre averaging to the species transport equation (2.63),

$$\frac{\partial \bar{\rho}\tilde{Y}_k}{\partial t}+\frac{\partial \bar{\rho}\tilde{Y}_k\tilde{u}_i}{\partial x_i}=\frac{\partial}{\partial x_i}\overline{(D_k\rho\frac{\partial Y_k}{\partial x_i})}+\bar{\omega}_k-\frac{\partial \overline{\rho Y_k''u_i''}}{\partial x_i} \tag{2.67}$$

The first term on the r.h.s. is molecular diffusion flux, and $\bar{\omega}_k$ is the mean chemical source term. The last term on the r.h.s. is the turbulent transport term. In high Reynolds number flows the molecular diffusion flux is small compared to the turbulent transport, so it is generally neglected.

The turbulent transport term is generally modeled with a simple classical gradient transport assumption (Peters, 2000),

$$\overline{\rho Y_k''u_i''}=-\frac{\mu_t}{Sc_t}\frac{\partial \tilde{Y}_k}{\partial x_i} \tag{2.68}$$

where μ_t is the turbulent eddy viscosity and Sc_t is turbulent Schmidt number. This gradient transport assumption is inspired from the turbulent scalar transport models in non-reactive, constant density flows. Due to its diffusive contribution, this model term tends to increase the stability of the numerical computation. Both experimental data and theoretical research (Bray et al., 1981; Shepherd et al., 1982), however, have shown the existence of counter-gradient scalar turbulent transport in some flames. This counter-gradient transport effect is generally explained due to the differential effect of pressure gradients on cold reactants and hot products, and gas expansion effect.

The modeling of mean reaction source term is the main problem of turbulent combustion. The difficulties associated with the mean reaction source term modeling are due to the highly nonlinear of reaction rate, which has a form of (2.66). It is not easy to express the mean reaction source term as a function of the mean mass fractions, the mean density and the mean temperature, without introduce large truncation errors. This problem has been addressed by Jones and Whitelaw (1982), Candel et al. (1999) and so on. For this reason, mean reaction source term is usually modeled from physical analysis.

Several different models have been evolved for closing the mean chemical source term. According to the analysis concepts used, three types of approaches can be classified (Veynante, 2002).

- **Turbulent mixing controlled models**

In this analysis, it is assumed that the reaction is fast and characteristic reaction time t_F is much smaller than the characteristic turbulent time t_I, i.e. the Damköhler number is much large than one. The reaction rate is controlled by the turbulent mixing rate, which is usually described in terms of scalar dissipation rates. The algebraic models, i.e. eddy-break-up (EBU) model and eddy-dissipation-concept (EDC) model, are belonging to this type of models.

- **Statistical models**

In this type of models, a system of joint probability density function (pdf) transport equations for the velocity and the reactive scalars are derived and solved. If the statistical properties of scalar fields are obtained for any location in the flowfield, their mean values and correlations can be extracted. In this analysis, the chemical reaction term is closed and no modeling is required. Additionally, this method is able to handle any complex reaction mechanisms. The drawback of this approach is its high dimensionality, so it is usually solved based on Monte–Carlo simulation techniques (Pope, 1985). Two ways are available for the computation of pdf, i.e. presumed pdf and transport equation for the pdf. The conditional moment closure (CMC) model and the Bray–Moss–Libby (BML) model can be classified to this kind analysis.

- **Flame structure based models**

In this type of models, the flame is viewed as a geometrical surface. This surface is usually defined as an iso-surface of mixture fraction for non-premixed flame or iso-surface of progress variable or *G* scalar for premixed flame. This method usually employs flamelet assumption, in which the flame is thin compared to all flow scales and the whole flame is an ensemble of locally laminar flamelets. The structure of the reacting flow normal to the turbulent flame surface can be analyzed using flamelet equations in one-dimensional flames. The main advantage of this approach is that the chemical mechanism is decoupled from the turbulent flow field. One example of this kind analysis is the *G*-equation based flamelet library approach (Peters, 1999; Nilsson & Bai, 2002; Wang & Bai, 2004b).

2.2.4 Comparison between turbulent premixed/non-premixed combustion modeling

In non-premixed combustion, the reaction is concentrated into a narrow flame zone at the stoichiometric state surface. The fuel and air are separated by this surface. Before the reaction can occur, the fuel and air should be mixed at the molecular level by molecular diffusion and turbulent convection. Since the time needed for convection and diffusion is typically much larger than the time needed for reaction to occur, the reaction rates are normally limited by the mixing rates (diffusion controlled), and it is appropriate to use the fast chemistry assumption, which introduces a significant simplification (Peters, 2000). In premixed combustion, the mixing process is removed, so the chemical kinetics becomes very important. The flame thickness of premixed combustion is usually thinner than that of non-premixed flame, in fact, it is also usually smaller than the Kolmogorov length scale. Depending on the Reynolds number and Damköhler number, the reaction rates can be influenced by either the mixing or the chemistry, so it is more difficult to model.

In addition to this, a very useful ‘conserved scalar’ variable called mixture fraction can be introduced into the non-premixed combustion modeling. The transport equation of it does not have reaction source term. All scalars such as temperature, species concentrations, and density are related to this variable in some way. Bilger (1993) and Klimenko (1990) proposed a conditional moment closure (CMC) concept for non-premixed turbulent combustion. They observed that most fluctuation of the reactive scalars can be associated with the fluctuation of the mixture fraction. Unfortunately, this variable is not useful in premixed combustion, since the value of it is constant everywhere.

Chapter 3

Turbulent premixed combustion

3.1 Features of premixed flame

A premixed flame is a self-sustaining propagation of a localized combustion zone, which can propagate at subsonic velocities or supersonic velocities (Turns, 2000). If it travels supersonically, it is called a detonation wave; otherwise it is a deflagration wave. In detonation, combustion is initiated by the advancing of a shock wave, which compresses and heats up the reactant mixture rapidly. This shock wave, in turn, is sustained by the energy released from the combustion. Contrary to this, a deflagration wave is sustained by the chemical reaction, and its traveling speed is controlled by the heat conduction and radical diffusion (Glassman, 1996). A prominent difference between the detonation and the deflagration is the pressure jump across the flame. Across the detonation flame, pressure increases greatly (the pressure in burnt side is generally 10–50 times higher than that in unburnt side), while in deflagration, the pressure is almost constant across the flame (actually there is a very small decrease). This work only deals with the deflagration combustion wave, which is simply called premixed flame.

Generally, reactants mixtures do not react directly, on the contrary, they react through radicals, which are highly reactive atoms or atoms clusters that have unpaired electrons (Turns, 2000). H, OH and O are typical radicals in combustion systems. These radicals react through a sequence of chain reactions: one molecule dissociates first to form radical species, and then this radical reacts to produce another radical species in a chain mechanism. Depending on the number of consumed radicals and produced radicals, chain reactions are generally classified to four types: chain-initiation, chain-propagating, chain-termination and chain-branching reactions (Turns, 2000; Glassman, 1996).

In chain-termination reaction, two radicals react to form a stable species and to break the chain. This type of reactions is often faster than other type chain reactions at lower temperatures (Glassman, 1996). An example of chain-termination reaction in hydrocarbon combustion is $H + OH + M \rightarrow H_2O + M$. On the other hand, the chain-branching reaction produces two radical species and consumes only one radical. With chain-branching, the concentration of radical species possibly increases geometrically, and causing the products to form rapidly. An example of this is $O + H_2O \rightarrow OH + OH$.

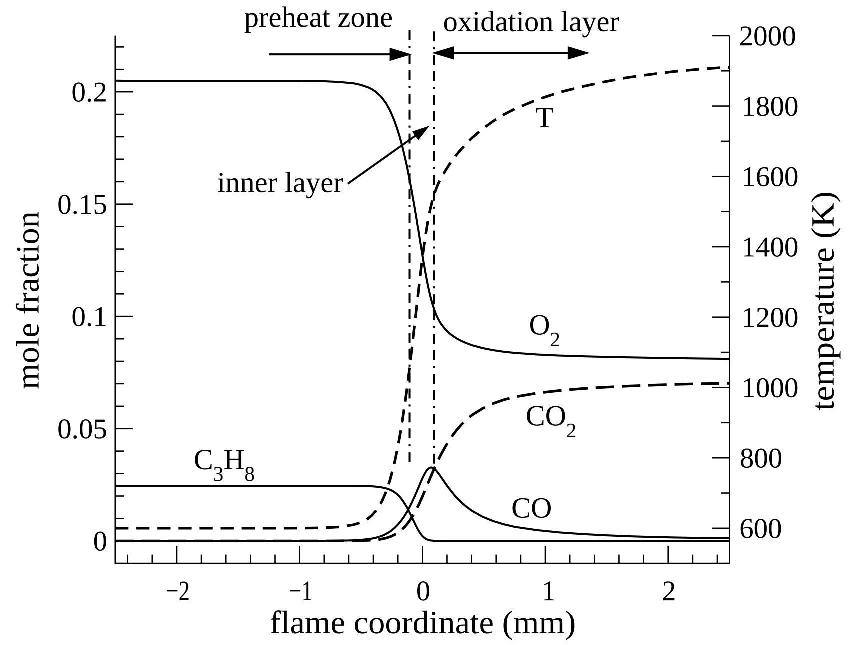

Figure 3.1 The concentration and temperature profiles for a C_3H_8/air laminar flame at 1 atm, fresh mixture temperature 600 K and equivalence ratio 0.6.

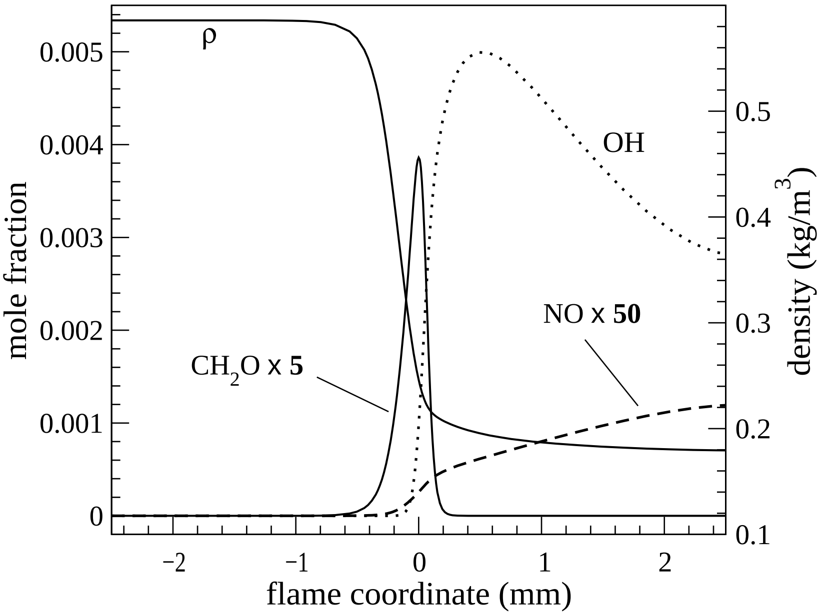

Figure 3.2 The concentration and density profiles for a C_3H_8/air laminar flame at 1 atm, fresh mixture temperature 600 K and equivalence ratio 0.6.

Above a critical temperature, the effects of chain-branching reactions will preponderate over that of chain-termination reactions, hence, a self-propagating flame sustained. This critical temperature, which is the so-called crossover temperature, is around 1300 K for hydrocarbon flames at ambient pressure (Peters, 2000).

The profiles of temperature, species and other important features of a premixed flame can be obtained using CFD tools employing detailed or simplified chemical mechanism. Figure 3.1 and 3.2 show the results for a lean propane-air flame with equivalence ratio 0.6 and fresh mixture temperature 600 K. The used code was developed by Mauss (1998).

As denoted in Figure 3.1, the flame contains several zones: the preheat zone, where little heat is released; an inner layer; and an oxidation zone. The inner layer is dominated by fast radical reactions, while the oxidation zone is dominated by oxidation of CO and H_2 (Seshadri & Peters, 1990). The inner layer and the oxidation zone form the so-called reaction zone, in which bulk of the energy is released. The thickness of this reaction zone, l_F, is quite thin, of the order of a millimeter, and the thickness of the inner layer is even thinner, approximately one tenth of the flame thickness. The laminar flame burning speed, s_L, at which the flame propagates into the fresh mixture and normal to the front, can also be calculated from the numerical simulations. Both the flame thickness and flame speed are thermo-chemical transport property (Peters, 2000), which depend primarily on the equivalence ratio, the temperature, and the pressure.

If the flame is stretched, the flame speed is different from the planar unstretched flame speed. The stretched flame speed is difficult to evaluate (Poinsot & Veynante, 2001). Clavin and Williams (1982) and Matalon and Matkowsky (1982) suggest a linear relationship between the stretched and unstretched flame speed based on asymptotic analyses, in the limit of small strain and curvature. The expression for the stretched flame speed is

$$s_L = s_L^0 - l_M K \tag{3.1}$$

where s_L and s_L^0 are the stretched and unstretched flame speed respectively; l_M is Markstein length; K is the stretch. The stretch K is defined by the rate of change of a flame surface, which contains effects from the strain rate and the curvature (Law & Sung, 2000; Poinsot & Veynante, 2001). The ratio of Markstein length to the laminar flame thickness l_F is called the Markstein number, which can be calculated with (Clavin & Williams, 1982; Matalon & Matkowsky, 1982)

$$\frac{l_M}{l_F} = \frac{1}{\gamma}\ln\frac{1}{1-\gamma} + \frac{Ze(Le-1)(1-\gamma)}{2\gamma}\int_0^{\gamma/(1-\gamma)} \frac{\ln(1+x)}{x}dx \tag{3.2}$$

Here, $Ze = E(T_b - T_u)/RT_b^2$ is the Zeldovich number, Le is the Lewis number of the deficient reactant, R is the universal gas constant, E is the activation energy. γ is a dimensionless temperature, which is defined as

$$\gamma = (T_b - T_u)/T_b \tag{3.3}$$

T_u and T_b are the temperatures on the unburnt and burnt side of combustion respectively. Lewis number is an important parameter, which compares the diffusion speeds of heat and mass,

$$Le = \alpha / D \tag{3.4}$$

where α is the thermal diffusivity, D is the mass diffusivity. Equation (3.2) shows that if Lewis number is smaller than unity, the Markstein length may become negative. In the wrinkled flame front with positive curvature (the flame front is convex with respect to the unburnt side), the flame speed of this part will be higher than s_L^0, and vice versa. This effect tends to enhance the flame wrinkle, and increase the flame surface rapidly. It can be used to explain the explosion of hydrogen-air mixtures, since its Lewis number is less than unity. This phenomenon is referred to as diffusion-thermal instabilities (Sivashinsky, 1977; Williams, 1985b).

3.2 Regimes of turbulent premixed combustion

Combustion takes place, in most combustion engines, within a turbulent flow field. Turbulence increases the reactants mixture consumption rate and hence heat releasing rate to much greater values than those of laminar combustion. This is preferable for decrease of the combustion engines size for a given energy output. In turbulent premixed combustion, the unburnt mixture enters into the mean turbulent flame zone in a direction normal to the mean front at a speed much higher than the laminar flame speed s_L. This speed is defined as turbulent flame speed s_T. Figure 3.3 shows an idealized steady premixed flame in a duct, with two zoom views of the flame at the bottom.

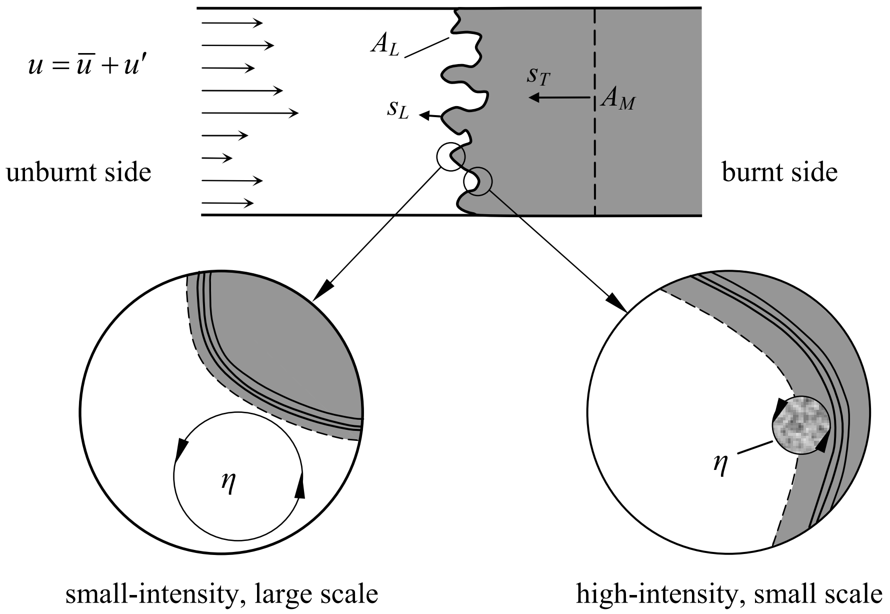

Figure 3.3 A schematic drawing of an idealized steady premixed flame in a duct.

Damköhler (1940) was the first one to analyze the early experimental data for turbulent burning velocity s_T. In his work, he specified two different regimes of turbulent premixed combustion: the small-intensity, large scale turbulence and the high-intensity, small scale turbulence. For small-intensity, large scale turbulence, Damköhler proposed that

$$s_T / s_L = A_L / A_M \tag{3.5}$$

where A_L is the total laminar flame front area, A_M is the mean turbulent flame area, as shown in Figure 3.3. Further, Damköhler proposed that the area ratio on the r.h.s. of (3.5) is proportional to $u'/s_L + 1$; thus, the turbulent flame speed can be expressed as

$$s_T \sim s_L + u' \tag{3.6}$$

For high-intensity, small scale turbulence, Damköhler assumed that turbulence only modifies the transport between the reaction zone and the unburnt zone with an enhanced equivalent diffusivity to replace the molecular kinematic viscosity. From the scaling relation for the laminar flame speed

$$s_L \sim (\nu / t_F)^{1/2} \tag{3.7}$$

the turbulent flame speed is estimated with

$$s_T \sim (\nu_t / t_F)^{1/2} \tag{3.8}$$

Here, ν and ν_t are the molecular and turbulent kinematic viscosity, respectively. From (3.7) and (3.8), a relation between s_T and s_L is obtained as

$$s_T / s_L \sim (\nu_t / \nu)^{1/2} \tag{3.9}$$

Peters (2000) identified the small-intensity, large scale and the high-intensity, small scale turbulence, with the corrugated flamelets regime and thin reaction zone regime (see Figure 3.4), respectively. The two zoom views in Figure 3.3 are schematic plotting of these two regimes. For small-intensity turbulence (left of bottom zoom view), the Kolmogorov scale is larger than the flame thickness, and the interaction between the flame front and the turbulence field is purely kinematic, i.e. turbulence can wrinkle the flame but can not disturb its local structure. For high-intensity turbulence (right of bottom zoom view), the Kolmogorov eddy scale is smaller than the preheat zone; hence, it can enters into the preheat zone, and enhances the transport of radicals and heat between the reaction zone and the unburnt gas.

A large number of experiments for measuring the turbulent flame speed have been conducted with different combustion configurations, such as the Bunsen flame, counter-flow flame, swirling flame and so on. Review articles on the turbulent flame speed are available in the literature, e.g. Bradley (1992). It is found that, at low turbulence intensity, the turbulent flame speed increase almost linearly with the turbulence level. If the turbulence levels are higher than some critical value, the turbulent flame speed, however, only increase slightly, and even quenching of the combustion may happen. This effect is known as turbulent flame speed bending in combustion literature (Bradley, 1992). In order to distinguish the influence of different turbulence level on the turbulent combustion, it is useful to classify the turbulent combustion into different regimes. To do this, a few dimensionless parameters are first introduced.

To simplify the analysis, it is general to assume equal diffusivities for all reactive scalars and the Schmidt number *Sc*, Lewis number *Le* and Prandtl number *Pr* unity.

$$Le = \frac{\alpha}{D} = 1, \qquad Pr = \frac{\nu}{\alpha} = 1, \qquad Sc = \frac{\nu}{D} = 1 \tag{3.10}$$

where ν, α and D are the momentum, thermal and mass diffusivity, respectively. In addition to this, relations for the laminar flame thickness l_F, reaction time scale t_F and laminar flame speed s_L are assumed based on the order analysis.

$$l_F = \frac{D}{s_L}, \qquad t_F = \frac{l_F}{s_L} = \frac{D}{s_L^2} \tag{3.11}$$

Then, the turbulent Reynolds number Re_l is expressed in terms of the turbulent fluctuation u' and turbulent integral length scale l as

$$Re_l = \frac{u'l}{\nu} = \frac{u'l}{s_L l_F} \tag{3.12}$$

The Damköhler number *Da*, the ratio of turbulent integral time scale t_I to the reaction time scale t_F, is expressed as

$$Da = \frac{t_I}{t_F} = \frac{l}{u'}\frac{s_L}{l_F} \tag{3.13}$$

The Karlovitz number compares the reaction time scale t_F to the Kolmogorov time scale t_η.

$$Ka = \frac{t_F}{t_\eta} = \frac{l_F^2}{\eta^2} \tag{3.14}$$

It is easy to derive a relation from (3.12) – (3.14) that

$$Re_l = Da^2 Ka^2 \tag{3.15}$$

Figure 3.4 shows a turbulent premixed combustion regime diagram in terms of length and velocity scale ratios in the log–log scale. This diagram is similar to those of Peters (2000) and Borghi (1988). It categorizes the turbulent premixed combustion into five regimes.

The *laminar flames regime* is located in the lower-left corner, which is separated from all turbulent flame regimes by line $Re_l = 1$. In *wrinkled flamelets regime*, the large eddies turnover velocity u' is less than the laminar flame speed, which does not exist in most of the practical applications.

In Figure 3.4, the line *Ka*=1 is called the Klimov–Williams criterion. Below this line, the flame thickness l_F is thinner than the Kolmogorov length scale. The turbulence eddies can only wrinkle the flame front and not able to disturb the reactive-diffusive laminar flame structure. This regime (*Ka*<1 and $u'/s_L > 1$) is called the *corrugated flamelets regime*, in which the flame front generally remains quasi-laminar.

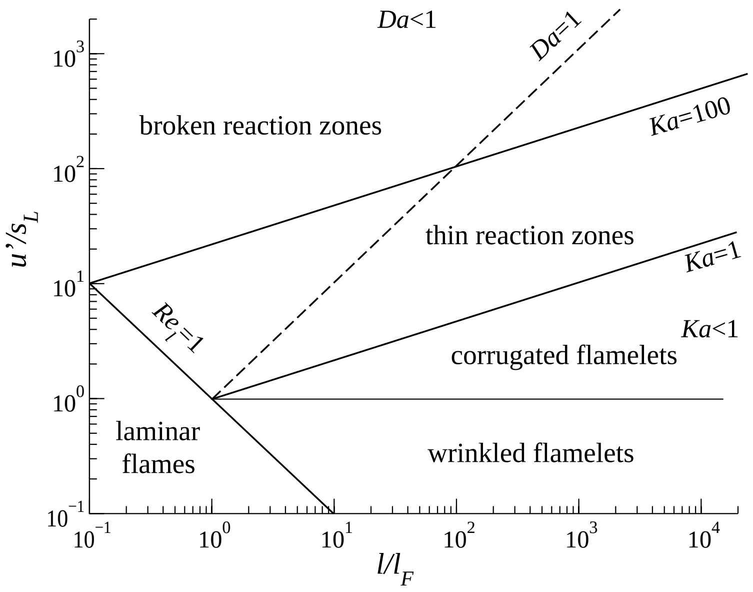

Figure 3.4 A regime diagram for premixed turbulent combustion.

The line *Ka*=100 is corresponding to the situation that the Kolmogorov length scale is equal to the inner layer thickness, which assumes the inner layer thickness is one tenth of the flame thickness l_F. The regime characterized by 1<*Ka*<100 and $Re_l > 1$ is called the *thin reaction zones*. Peters (2000) argued that in this regime, the Kolmogorov eddies can enter into the preheat zone but can not penetrate into the inner layer, since $l_\delta < \eta < l_F$, where l_δ denotes the thickness of inner layer. Due to this, this regime is also called '*thickened-wrinkled flame*' (Poinsot & Veynante, 2001). Above the line *Ka*=100, it is called *broken reaction zones*, in which both the preheat zone and inner layer are disturbed by the turbulence eddies, and thin flame could no longer be identified.

Figure 3.4 also shows the line *Da*=1, above which the turbulent mixing time is shorter than the reaction time, hence the overall reaction rate is limited by chemistry. This regime (*Da*<1) is often called the '*well-stirred reactor*'. In practical combustion engines, this regime is generally difficult to access, since complete fast mixing without quenching is almost impossible to achieve (Glassman, 1996). In theory analysis, however, it is useful, for example, it estimates the maximum overall energy release rate in a fixed volume.

3.3 Models for turbulent premixed combustion

As discussed in Section 2.1, turbulent flows are often calculated with averaged or filtered equations, in which those unclosed terms are modeled with the resolved variables. Unfortunately, the mean reaction rates are difficult to evaluate with the averaged or filtered Arrhenius expressions, based on the resolved variables (e.g. mean temperature and concentrations), because of the high nonlinearity of reaction rate. Due to this, the mean reaction rates are usually modeled from physical analysis. Many different turbulent combustion models have been proposed till now, and several recent reviews are available in literature (Bray, 1996; Brewster et al., 1999; Candel et al., 1999; Veynante & Vervisch, 2002). Here, some of the turbulent premixed combustion modeling methods is briefly reviewed. Since the development of RANS combustion models started much earlier than that of LES, the RANS combustion models are in a more mature state than LES combustion models, therefore, ideas of RANS combustion models are usually extended to LES framework with certain modification. In this section, models are explained in RANS framework, unless otherwise explicitly stated.

3.3.1 Eddy-break-up model

The EBU model was first devised by Spalding (1971). It is based on the argument that, at high Damköhler number, it is the turbulent mixing that controls the chemical reaction rates rather than the chemistry. The turbulent mean formation rate for products is expressed as

$$\bar{\omega}_p = C_{EBU}\bar{\rho}\,(\overline{Y_p^{"2}})^{\frac{1}{2}} \Big/ t_{EBU} \tag{3.16}$$

where $\overline{Y_p^{"2}}$ is the variance of the mass fraction of product. The EBU mixing time t_{EBU} is estimated from the turbulent kinetic energy k and its dissipation rate ε, thus

$$\bar{\omega}_p = C_{EBU}\bar{\rho}\frac{\varepsilon}{k}(\overline{Y_p^{"2}})^{\frac{1}{2}} \tag{3.17}$$

In this formulation $\overline{Y_p^{"2}}$ must be modeled. Based on similar argument, Magnussen and Hjertager (1977) proposed the eddy-dissipation-concept model (EDC).

The influence of chemistry is neglected, thereby these models represent fast chemistry limit only. The constants in the models have to be adjusted within a wide range for practical problems. EBU model tends to overestimate the reaction rate, especially in highly strained regions. Due to their simplicity, EBU model and its modifications, however, are attractive and have been widely used in many commercial CFD packages.

3.3.2 Probability density function model

The probability density function (pdf) models are based on one-point statistical analysis. If the probability of finding a variable at a location is known, then its mean value at this location can be determined. This idea is easily extended to take into account multiple variables. For example, the instantaneous reaction rate is a function of species mass fractions and temperature as

$$\omega = \omega(Y_1, Y_2 ....., T) \tag{3.18}$$

If the joint probability $p(Y_1, Y_2, ...T)$ for $Y_1, Y_2 ....., T$ in the range

$$\begin{cases} Y_1 \in (Y_1 - \tfrac{1}{2} dY_1, Y_1 + \tfrac{1}{2} dY_1) \\ . \quad . \quad . \quad . \quad . \quad . \\ T \in (T - \tfrac{1}{2} dT, T + \tfrac{1}{2} dT) \end{cases} \tag{3.19}$$

is known, then the mean reaction rate $\bar{\omega}$ can be determined as

$$\bar{\omega} = \int_{Y_1, Y_2, ...T} \omega(Y_1, Y_2, ...T) p(Y_1, Y_2, ...T) dY_1 dY_2 ....dT \tag{3.20}$$

This pdf statistical description of turbulent reaction flow has some theoretical advantages: the complex chemistry is treated exactly without applying assumptions such as ‘flamelet’ and ‘fast reaction’; it can be applied equally well to non-premixed, premixed, and partially premixed flames. The information of pdf may be extracted from experimental data or DNS. In general, two main ways are used to calculate the pdf: one is presumed pdf approach and another is pdf transport equation approach.

- **Presumed pdf approach**

Though a pdf function can take any shape and have multiple extrema, in many combustion cases, however, it is found that pdf functions show some common features; therefore it is reasonable to represent them with a special shape but with different controlling parameters. One of the most popular approaches is to assume the pdf function as a $\beta -$ function, and its controlling parameters are the mean and variance of the variable (Borghi, 1988). It has a form as

$$p(\phi) = \frac{\phi^{a-1}(1-\phi)^{b-1}}{\int_0^1 \phi^{a-1}(1-\phi)^{b-1} d\phi} \tag{3.21}$$

$$a = \tilde{\phi}\left[\frac{\tilde{\phi}(1-\tilde{\phi})}{\widetilde{\phi''^2}} - 1\right], \qquad b = \frac{a}{\tilde{\phi}} - a \tag{3.22}$$

The disadvantage of this presumed pdf method is that it is difficult to guess or measure joint pdf of multiple variables (Pope, 1985). A simple way is to assume that these variables are statistical independent. Thus, a joint pdf function, e.g. $p(\phi,\varphi,\gamma)$, can be expressed as

$$p(\phi,\varphi,\gamma) = p_\phi(\phi)p_\varphi(\varphi)p_\gamma(\gamma) \tag{3.23}$$

Unfortunately, this assumption does not hold in practical combustion situations, since variables, such as temperature and species mass fraction, are closely related in flames (Poinsot & Veynante, 2001).

- **Pdf transport equation**

In this approach, a transport equation for pdf is solved. This transport equation can be derived from several different ways (Pope, 1985; Vervisch et al., 1995). For a multi-species, density-weighted joint pdf, $\tilde{p}(\psi_1,\psi_2....,\psi_n)$, this transport equation (Pope, 1985; Candel et al., 1999) is

$$\begin{aligned}\bar{\rho}\frac{\partial \tilde{p}}{\partial t} + \bar{\rho}\tilde{u}_k\frac{\partial \tilde{p}}{\partial x_k} = & \underbrace{-\frac{\partial}{\partial x_k}\left[\overline{\rho(u''_k \,|\, \underline{Y}=\underline{\psi})}\tilde{p}\right]}_{\textit{Turbulent convection}} \\ & \underbrace{-\bar{\rho}\sum_{i=1}^{n}\sum_{j=1}^{n}\frac{\partial}{\partial \psi_i}\frac{\partial}{\partial \psi_j}\left[\overline{D(\frac{\partial Y_i}{\partial x_k}\frac{\partial Y_j}{\partial x_k} \,|\, \underline{Y}=\underline{\psi})}\tilde{p}\right]}_{\textit{Molecular mixing}} \\ & \underbrace{-\bar{\rho}\sum_{i=1}^{n}\frac{\partial}{\partial \psi_i}[\omega(\psi_1,\psi_2...,\psi_n)\tilde{p}]}_{\textit{Chemical reaction}}\end{aligned} \tag{3.24}$$

Here, the operator $\overline{Q\,|\,\underline{Y}=\underline{\psi}}$ corresponds to conditional averaging of variable Q for the sampling values ψ_i. The chemical reaction term in (3.24) is closed and does not include any modeling, so it can handle any complex chemical mechanism. In this respect, it is often argued that the transport pdf method has a considerable advantage over other turbulent combustion models (Peters, 2000).

The unclosed molecular mixing terms in (3.24), however, are difficult to model, since this approach is based on local one-point statistical description of quantities, but the spatial gradient in the unclosed term requires additional spatial information (Poinsot & Veynante, 2001). Another drawback of transport pdf approach is its high dimensionality, which limits the application of finite-volume and finite-difference techniques, since their memory requirements increase roughly exponentially with dimensionality. Generally, Monte–Carlo algorithms are used (Pope, 1985), in which memory requirements increase almost linearly with the dimensionality. However, in order to decrease statistical error, a large number particles should be present in each grid cell, which makes it a very time consuming process. Up to now, the transport equation method is only applied to relatively simple situations (Poinsot & Veynante, 2001).

Jones and Prasetyo (1996) presented a calculation of a premixed turbulent counter flow jet configuration, using a five-scalar joint pdf transport equation. Two models for closuring the unknown molecular mixing term in (3.24) were used and compared with each other. The chemistry was described by a four-step reduced reaction mechanism of Jones and Lindstedt (1988). A standard finite-difference method was used to calculate the flowfield with a $k-\varepsilon$ model, whereas the pdf transport equation was solved using a Monte–Carlo technique. It was shown that the agreement between the computation results and the measured data is good (except the carbon monoxide concentration).

3.3.3 Bray–Moss–Libby model

This model was proposed by Bray et al. (1977). It may be viewed as a presumed pdf model: the pdf of the progress variable c is assumed to be bimodal and only two flow states are considered: unburnt ($c=0$) or burnt ($c=1$). In addition to this statistical approach, it also employs a flamelet concept, which assumes that the flame front is infinitely thin. The BML model has revealed some important features of turbulent premixed combustion such as counter-gradient turbulent transport and flame induced turbulence generation (Poinsot & Veynante, 2001).

The pdf of the progress variable c at a given location is represented with two Dirac delta functions as

$$p(c,x,t)=\alpha(x,t)\delta(c)+\beta(x,t)\delta(1-c) \tag{3.25}$$

where α and β are the probabilities to find unburnt and burnt mixtures at local position x. The probability of finding the flame front (burning mixture) is zero, since BML model is based on the condition $Re \gg Da \gg 1$ and assumes that the flame is infinitely thin. The normalization condition should be satisfied

$$\alpha(x,t)+\beta(x,t)=1 \tag{3.26}$$

From the definition, a few relations can be obtained

$$\overline{\rho c}=\bar{\rho}\tilde{c}=\int_0^1 \rho c^* p(c^*)dc^* = \rho_b \beta \tag{3.27}$$

$$\bar{\rho}=\int_0^1 \rho p(c^*)dc^* = \alpha\rho_u+\beta\rho_b \tag{3.28}$$

where subscript u and b denote the unburnt and burnt side respectively. Using these relations, the Favre average of any quantity Q can be expressed as

$$\tilde{Q}=(1-\tilde{c})\bar{Q}_u+\tilde{c}\bar{Q}_b \tag{3.29}$$

Here, $\bar{Q}_u$ and $\bar{Q}_b$ are the conditional average of Q for given c value at 0 and 1. Thus, the scalar turbulent flux $\overline{\rho u'' c''}$ can be expressed as:

$$\overline{\rho u''c''} = \bar{\rho}(\widetilde{uc} - \tilde{u}\tilde{c}) = \bar{\rho}(\tilde{c}\bar{u}_b - \tilde{c}\tilde{u}) = \bar{\rho}\tilde{c}(1-\tilde{c})(\bar{u}_b - \bar{u}_u) \tag{3.30}$$

For a steady one-dimensional turbulent premixed flame propagating along the x-axis (positive x is pointing towards the burnt side), $\partial\tilde{c}/\partial x > 0$. From the often used gradient turbulent transport assumption (see (2.68)), it leads to $\overline{\rho u''c''} < 0$. However, from (3.30), the turbulent flux $\overline{\rho u''c''} > 0$, since $\bar{u}_b - \bar{u}_u > 0$. This conflicts with the gradient turbulent transport assumption. Thus, BML reveals the counter-gradient diffusion effect. DNS data (Wenzel & Peters, 2000) has shown that the turbulent mixing effect results in gradient diffusion, whereas the gas expansion effect results in counter-gradient diffusion.

In BML model, the mean chemical source is usually closed with three main approaches: one based on scalar dissipation rate, one based on flame crossing frequency and one based on flame surface density. More detailed description can be found in Poinsot and Veynante (2001) and the references therein.

3.3.4 Artificially thickened flame model

Unlike in the RANS, where the mean turbulent flame is solved, and therefore the solved flame is very thick, in LES the filtered instantaneous flame is solved, and its flame thickness is generally smaller than the LES mesh size. This leads to numerical problems in LES. One way to overcome this difficulty is to use the artificially thickened flame method, proposed by Butler and O'Rourke (1977).

From a dimension analysis of laminar premixed flame, the laminar flame thickness l_F, reaction rate R_c and speed s_L have relations as

$$s_L \propto \sqrt{\alpha R_c}\,, \qquad l_F \propto \frac{\alpha}{s_L} \propto \sqrt{\frac{\alpha}{R_c}} \tag{3.31}$$

where α is the thermal diffusivity. In artificially thickened flame approach, the flame thickness is thickened by a factor F, whereas the laminar flame speed is kept constant. This thickening is achieved by increasing α by a factor F whereas decreasing the pre-exponential constant of the chemical Arrhenius law (see (2.66)) by F. If factor F is large enough, the thickened flame front may be resolved on the LES grids.

In this method, the reaction rate is still calculated using the Arrhenius law; therefore various phenomena (quench, ignition *etc.*) may be accounted for without turning to sub-models. However, its inherent drawback is that the interaction between turbulence and combustion is altered because the Damköhler number is decreased by factor F. Because of this, the flame becomes more insensitive to turbulence motions (Poinsot & Veynante, 2001). In Colin et al. (2000), a subgrid scale wrinkling factor is derived to compensate this effect based on DNS of flame-vortex interaction.

3.3.5 Flamelet concept

Williams (1975) suggested that the turbulent flame can be viewed as an ensemble of locally stretched laminar flames, called flamelets, and this thin layer of flamelets is then embedded in an otherwise no reacting turbulent flow field. The turbulence and chemistry influence each other through this mechanism: the flamelet introduces heat expansion and flow acceleration across the flame front, which changes the turbulent flow fields on both side of flame front; on the other hand, the turbulent eddies convect and distort the flame front, but are not able to disturb the structure of flamelets. In this way, the calculation of turbulence and chemistry are decoupled.

The flamelet concept is build upon an assumption that turbulence can not disturb the structure of flamelets. From qualitative kinetic analysis, this requires that the Kolmogorov length scale should be larger than the flame thickness, i.e. the Karlovitz number is less than one. In Figure 3.4, the regimes suitable for flamelet concept, which include the corrugated flamelets and wrinkled flamelets regimes, are separated from other regimes with the line Ka=1, i.e. the Klimov–Williams criterion. However, many experimental observations and computational results (Poinsot et al., 1991; Shepherd et al., 2002; Baum et al., 1994; Buschmann et al., 1996; Sankaran & Menon, 2000) showd that this regime may be extended to large Karlovitz number. They found that, when Ka are moderate larger than 1, e.g. 14–17, the turbulent eddies can broaden the preheat zone and increase the heat and species diffusion, however these eddies do not penetrate the thin reaction zone because of the increased viscous dissipation by high temperature near the flame and the reaction zone is still thin. In this range, the primary effect of increasing turbulence is to wrinkle the flame front and so increase the reaction rate, but not to change the thin layer structure. Therefore, Peters (1999 & 2000) argued that the applicable region for flamelet concept can be extend to Ka<100, which is depicted in Figure 3.4.

To use the flamelet concept, the laminar flame structure is of great importance. Williams (2000) recently reviewed the flamelet structures of premixed, diffusion and partially premixed diffusion flames. In numerical simulations, the flamelet structure is obtained by a separated computation, in which flamelet equations describing the reactive-diffusive structure in the vicinity of the flame surface are solved. A detailed description of deriving the flamelet equations and extracting the profiles normal to the flame front from the results can be found in Peters (2000) and the references therein.

In flamelet approaches, the location of the flamelet in a turbulent flow field is denoted by a geometrical surface, which is in generally an iso-Z (mixture fraction) surface for diffusion flames, and iso-c (progress variable) or iso-G (signed distance function) surfaces for premixed flames. For partially premixed combustion, a flamelet model for diffusion flame and a flamelet model for premixed flame are usually used together as in Chen et al. (2000), where a Z-equation and a G-equation are solved simultaneously.

3.4 Premixed combustion modeling based on *c*-equation.

Several turbulent premixed combustion modeling approaches based on *c*-equation are described briefly in this section. The level set *G*-equation used in this thesis work will be described in detail in Chapter 4.

3.4.1 *c*-equation

In an adiabatic premixed combustion with one-step and irreversible chemistry, if the specific heat capacity of species is assumed constant, then the reactive species concentration and the temperature are all linearly related to a non-dimensional temperature c, known as reaction progress variable. It is defined as

$$c = \frac{T - T_u}{T_b - T_u} \tag{3.32}$$

The balance equation (Boger et al., 1998) for the progress variable c may be written as:

$$\frac{\partial \rho c}{\partial t} + \nabla \cdot (\rho \boldsymbol{u} c) = \nabla \cdot (\rho D \nabla c) + \dot{\omega}_c \tag{3.33}$$

$$= \rho s_d \, |\nabla c| \tag{3.34}$$

Here, D is the molecular diffusivity, $\boldsymbol{u}$ is velocity vector. Equation (3.34) is another form of c-equation written in terms of flame front displacement speed s_d. Appling the LES filter, it becomes

$$\frac{\partial \bar{\rho} \tilde{c}}{\partial t} + \nabla \cdot (\bar{\rho} \tilde{\boldsymbol{u}} \tilde{c}) + \nabla \cdot [\bar{\rho}(\widetilde{\boldsymbol{u}c} - \tilde{\boldsymbol{u}} \tilde{c})] = \overline{\nabla \cdot (\rho D \nabla c)} + \overline{\dot{\omega}_c} \tag{3.35}$$

$$= \overline{\rho s_d \, |\nabla c|} \tag{3.36}$$

The three terms on the l.h.s. of (3.35) are unsteady effects, resolved convective flux and unclosed transport flux, respectively. On the r.h.s. of (3.35), the two terms denote respectively filtered molecular diffusion and filtered reaction rate. The unclosed transport flux is usually modeled with a simple gradient expression:

$$\bar{\rho}(\widetilde{\boldsymbol{u}c} - \tilde{\boldsymbol{u}} \tilde{c}) = -\frac{\mu_t}{Sc_t} \nabla \tilde{c} \tag{3.37}$$

Several approaches are proposed to estimate the unclosed term on (3.36). A brief description of them is given in the following sections.

3.4.2 Flame surface density model

An approach to describe the unclosed term on (3.36) is based on the concept of filtered flame surface density. The flame surface density Σ (unity: m^2/m^3) describes the flame front convolutions. Both algebraic expressions (Boger et al., 1998) and transport equations (Boger et al., 1998; Hawkes & Cant, 2000 and 2001) have been proposed to calculate Σ. The one proposed in Hawkes and Cant (2001) is written as

$$\overline{\rho s_d \,|\nabla c|} = \rho_u s_L \Sigma \tag{3.38}$$

$$\begin{aligned} &\frac{\partial \Sigma}{\partial t} + \frac{\partial(\tilde{u}_i \Sigma)}{\partial x_i} + \frac{\partial}{\partial x_i}\Big((\overline{(u_i)_s} - \tilde{u}_i)\Sigma \Big) = \overline{(a_T)_s}\Sigma \\ &\qquad - \frac{\partial}{\partial x_i}\Big(\overline{(s_L N_i)_s}\Sigma \Big) + \overline{\left(s_L \frac{\partial N_i}{\partial x_i} \right)_s} \Sigma \end{aligned} \tag{3.39}$$

where the subscript *sg* represents the subgrid scale. The three terms on the l.h.s of (3.39) are the rate of change, the mean flow convection, and the subgrid convection respectively. On the r.h.s. there are the effect of fluid strain, a planar propagation term, and production of flame surface density related to the curvature and propagation effect.

The last four terms on (3.39) are unclosed and have to be modeled. Boger et al. (1998) argued that these terms may be easily extracted from DNS or experimental results, since they are physically well defined terms.

3.4.3 Turbulent flame closure model

In the so-called turbulent flame (or flame-speed) closure (TFC) model, the unclosed term on (3.36) is estimated based on a turbulent flame speed as

$$\overline{\rho s_d \,|\nabla c|} = \rho_u s_{sg} \,|\nabla \tilde{c}\,| \tag{3.40}$$

s_{sg} is the subgrid turbulent flame speed in LES framework.

The TFC model was first proposed by Zimont (1979), and has recently been applied and tested on some premixed combustion cases (Karpov et al., 1996; Zimont, 2000). Based on the Kolmogorov assumption of the equilibrium fine-scale turbulence and the assumption of the universal small-scale structure of the wrinkled flamelet sheet, Zimont (2000) proposed an expression for the turbulent flame speed s_T in RANS context. It is shown below

$$s_T = C u' (Da)^{1/4} \tag{3.41}$$

C is an empirical parameter, which has a value around 0.5. *Da* is the Damköhler number.

Flohr and Pitsch (2000), and Zimont and Battaglia (2003) have applied the TFC model in LES framework. In Flohr and Pitsch (2000), the subgrid turbulent flame speed s_{sg} is expressed as

$$s_{sg} / s_L = 1 + C (Re_\Delta Pr)^{1/2} Da^{-1/4} \tag{3.42}$$

where $Re_\Delta = u'_\Delta \Delta / \nu$. The subgrid turbulent velocity u'_Δ is estimated as

$$u'_\Delta = C_s \Delta (2 \tilde{S}_{ij} \tilde{S}_{ij})^{1/2} \tag{3.43}$$

where $\tilde{S}_{ij}$ is the filtered strain rate tensor has a similar form as (2.37), C_s is a model constant.

3.4.4 Flame wrinkling density model

This model is very similar to the flame surface density approach, but it is developed by the application of conditional averaging techniques to the turbulent flame interface. The flame distribution is represented by a flame wrinkle density scalar Ξ, which is the ratio between the turbulent flame surface and its projection in the propagation direction. A detailed derivation of this model in RANS framework may be found in Weller (1993).

A new flame wrinkling model in LES context is proposed by Weller et al. (1998) and then applied to study combustion instabilities in a jet engine afterburner (Fureby, 2000). Like the model used in RANS, it considers a regress variable *b* instead of progress variable *c*. *b* represents the unburnt gas mass fraction, which has a relation with *c* as $b = 1 - c$. A transport equation is obtained by filtering the conditional transport equation of *b*

$$\frac{\partial \bar{\rho}\tilde{b}}{\partial t} + \nabla \cdot (\bar{\rho}\tilde{\upsilon}\tilde{b}) - \nabla \cdot (\bar{\rho} D \nabla \tilde{b}) = -\rho_u s_L \Xi \, |\nabla \tilde{b}| \tag{3.44}$$

A transport equation for flame wrinkle density scalar Ξ is then proposed

$$\frac{\partial \Xi}{\partial t} + \widehat{\upsilon_s} \cdot \nabla \Xi = G\Xi - R(\Xi - 1) + (\sigma_s - \sigma_t)\Xi \tag{3.45}$$

where $\widehat{\upsilon_s}$ is the surface-filtered effective velocity of the flame. $G\Xi$ and $R(\Xi - 1)$ are the subgrid turbulent generation and removal rates, respectively. Expressions for $\widehat{\upsilon_s}$, $G\Xi$ and $R(\Xi - 1)$ are proposed by Weller et al. (1998). σ_t and σ_s are two resolved strain rates, which can be expressed with resolved quantities.

In addition to the transport equation for Ξ, Weller et al. (1998) even proposed a transport equation for the laminar flame speed s_L to account for the strain rate influence on the laminar flame speed though no rigorous validation is made.

$$\frac{\partial s_L}{\partial t} + \widehat{\upsilon_s} \cdot \nabla s_L = -\sigma_s s_L + \sigma_s s_L^{\infty} \frac{(s_L^0 - s_L)}{(s_L - s_L^{\infty})} \tag{3.46}$$

The information of the terms in (3.46) can be found in Weller et al. (1998).

Validation and development of the LES combustion models, based on flame surface density Σ and the flame wrinkling density Ξ, have been reported by Knikker et al. (2000).

Chapter 4

LES of turbulent premixed combustion using level set *G*-equation

In this thesis work, a so-called level set *G*-equation is used to describe the position of the thin premixed flame front. The level set *G*-equation is different from both the *Z*-equation and *c*-equation in many aspects. The background of the level set *G*-equation and its derivation in LES framework are described in this Chapter.

4.1 Level set *G*-equation

4.1.1 Background of level set *G*-equation

The well-known level set equation (Barth & Sethian, 1998), which has a general form as

$$\frac{\partial \phi}{\partial t} + F(x, \nabla \phi, k)\left|\nabla \phi\right| = 0 \tag{4.1}$$

has been widely used in large number of areas for tracking the motion of fronts, such as in the image science (Tsai & Osher, 2003), fluid interface problems (Sethian & Smereka, 2003), crystal growth (Sethian & Strain, 1992), flame propagation (Nilsson & Bai, 2000 and 2002; Peters, 1999), and semi-conductor manufacturing (Adalsteinsson & Sethian, 1999), to give just a few examples. In the level set equation (4.1), the zero level set $\phi = 0$ corresponds to the moving front, k is the curvature of the level set surface. It describes the front propagating along its normal direction with a speed F, which is a function of multiple variables like x, $\nabla\phi$, k. If the propagating front is also passively advected by an underlying flow field $\boldsymbol{u}$, then (4.1) can be rewritten as

$$\frac{\partial \phi}{\partial t} + F(x, \nabla \phi, k)\left|\nabla \phi\right| + \boldsymbol{u} \cdot \nabla \phi = 0 \tag{4.2}$$

The level set approach was introduced into the premixed combustion modeling field many years ago thanks to the pioneer works of Markstein (1964), Williams (1985a) and many others. Since the premixed combustion modeling methods based on level set approach generally use a scalar G to describe the flame front, the level set equation is also called level set G-equation or G-equation in the combustion literature.

Figure 4.1 shows an instantaneous flame surface, which is represented by the zero level set of quantity G

$$G(\vec{r},t)=0 \tag{4.3}$$

where $\vec{r}$ denotes the spatial position, $\vec{n}$ is the unit normal vector to the front and points into the unburnt zone, which is defined by

$$\vec{n}=-\nabla G/|\nabla G| \tag{4.4}$$

This zero level set divides the flow field into two zones: $G>0$ the burnt zone and $G<0$ the unburnt zone. Differentiating (4.3) with respect to t, one obtains

$$\frac{\partial G}{\partial t}+\nabla G\cdot\frac{d\vec{r}}{dt}=0 \tag{4.5}$$

The $d\vec{r}/dt$ is the propagation speed of the flame front and results from two contributions: the flow velocity $\boldsymbol{u}$, and the (burning) velocity of the flame-front normal to itself, $\vec{n}s_L$.

$$\frac{d\vec{r}}{dt}=\boldsymbol{u}+\vec{n}s_L \tag{4.6}$$

Substituting (4.4) and (4.6) into (4.5), the well-known G-equation is derived

$$\frac{\partial G}{\partial t}+\boldsymbol{u}\cdot\nabla G=s_L|\nabla G| \tag{4.7}$$

This equation is applicable to thin flame structures (Peters, 2000), which propagate with a well defined burning velocity s_L. It is suitable for the corrugated flamelets regime shown in Figure 3.4. Different from the c-equation and Z-equation, G-equation has several special properties. For example, it is a Hamilton–Jacobi type equation, and it is only well defined at the zero level set. A brief discussion of these special properties is given below.

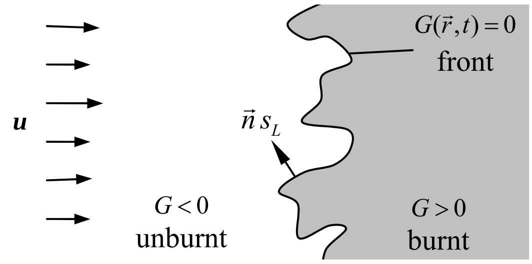

Figure 4.1 Sketch of an instantaneous flame front represented by scalar G.

4.1.2 Hamilton–Jacobi equation

The Hamilton–Jacobi equation has a general form as

$$\frac{\partial \phi}{\partial t} + H(x,t,\phi,\nabla\phi) = 0, \qquad \phi(x,0) = \phi_0(x) \tag{4.8}$$

It is an initial value problem. It is known that the solutions of it typically are continuous but with discontinuous derivatives, i.e. forming cusps, even when the initial condition is smooth (Jiang & Peng, 2000), and such solutions are in general not unique. The physically relevant solution of it is the so-called ‘viscosity solution’, which is a unique solution obtained upon the addition of an infinitesimal diffusive term to (4.8) (Crandall & Lions, 1983; Kerstein & Ashurst, 1988).

Several numerical methods can be used to obtain the approximate viscosity solution for Hamilton–Jacobi type equation, for example the high-order Godunov-type schemes (Osher & Sethian, 1988) and the high-order essentially non-oscillatory (ENO) and weighted ENO (WENO) schemes (Jiang & Peng, 2000; Osher & Sethian, 1988).

4.1.3 Front tracking and front capturing approaches

Since the *G*-equation is derived from (4.3) and (4.6), which both are only defined on the flame front (zero level set), the *G*-equation only has physical meaning at the flame front. The scalar *G* outside the flame front is not uniquely defined. Due to this, the *G*-equation may be viewed as a flame front tracking method (Qian, 1998). Front tracking approaches, such as Tryggvason et al. (2001) and Udaykumar et al. (1997), generally use a series of connected marker points located on the front to separate the flow field. The front characteristics such as curvatures can be extracted from this marker points. When a large number of marker points used to represent the front, the front tracking method can provide high accuracy. One major disadvantage of this method is that it has to handle the topological changes explicitly, i.e. to remove, add or reconnect the marker points according to some conditions, and this is more difficult in three dimensions than in two dimensions.

Contrary to the front tracking approach, the front capturing method is able to handle topology changes easily, and the codes developed for two dimensions problem can be converted to three dimensions easily (Sethian & Smereka, 2003). In equation (4.7), since the scalar *G* surrounding the flame front (zero level set) is not uniquely defined, it may be assigned arbitrarily without changing the physics of the problem, and at the same time keep the zero iso-surface of this assigned *G* field coincides with the original flame surface. By this way, the flame front becomes an iso-surface of a scalar, which is defined in the whole field, therefore the *G*-equation turns into a front capturing method. Chopp (1993) and Sussman et al. (1994) proposed to define the surrounding *G* field as a signed-distance function, which can be expressed in a first-order partial differential equation

$$\left|\nabla G\right| = 1 \tag{4.9}$$

4.1.4 Distance function

The signed-distance is a well defined physical quantity, which represents the shortest distance from a local point to the zero level set but with a sign: if this point lies in the $G > 0$ side, it is positive, otherwise, it is negative. However, in evolution of (4.7) (suppose it has been extended to be valid in whole field), *G* will not necessarily remain as the signed-distance, though the initial *G*-field maybe initialized to satisfy the signed-distance function (4.9) (Sethian & Smereka, 2003). Therefore, it is necessary to reshape the level set *G*-field to the signed-distance function but without change its zero level set every now and then. This reshaping is called signed-distance reinitialization, which was first exploited by Chopp (1993).

Several methods have been developed to perform reinitialization. One straightforward way is to calculate the shortest distance to the front directly. This method, however, requires explicitly knowing the position of the front, and is very time-consuming. Strain (1999) presented an efficient quadtrees method to compute global approximate distance, which belongs to this type of reinitialization approach.

Another way for reinitialization is by solving the Eikonal type equation (4.9) directly. Tsitsiklis (1995) combined the heap sorting method with a Dijkstra's network path algorithm (Dijkstra, 1959) to obtain the viscosity solution of the steady state Eikonal equation, based on a control-theoretic approach. Simultaneously, Sethian developed an efficient method, which is the so-called fast marching method, to perform reinitialization. It is based on high order upwind, finite difference schemes for hyperbolic conservation laws. More detailed information of fast marching method can be found in the recent review by Sethian (2001). Tsai (2002) argued that the fast marching method is not consistent for computing the distance to isolated points, e.g. its solution looks like diamond shaped polyhedra instead of perfect circles/spheres. To solve this problem, Tsai (2002) proposed a reinitialization algorithm by incorporating the upwinding-based stencil selection and the geometric interpretation.

An extension velocity concept related method was presented by Adalsteinsson and Sethian (1999), which can update the level sets according to a given velocity defined on the front in such a way that the signed distance function is maintained, and no reinitialization is needed. For example, in (4.1), the propagating speed *F* only has definition on the front. If an extension velocity F_{ext} valid for all the level sets can be constructed and it satisfies

$$F_{ext}\big|_{\phi=0} = F \qquad (4.10)$$

then (4.1) can be switched to

$$\frac{\partial \phi}{\partial t} + F_{ext}(x, \nabla\phi, k)\left|\nabla\phi\right| = 0 \qquad (4.11)$$

This equation is thus valid in whole level sets including the front level. It is straightforward to see that, if F_{ext} satisfies relation

$$\nabla F_{ext} \cdot \nabla \phi = 0 \tag{4.12}$$

then the solution of (4.11) will satisfy the signed distance equation naturally, suppose the initial level sets is a signed distance equation (Adalsteinsson & Sethian, 1999). In their work, Adalsteinsson and Sethian used the fast marching method to solve (4.12). In addition to these reinitialization approaches explained above, Sussman et al. (1994) introduced a different method for computing signed distance, based on solving the following partial differential equation:

$$\begin{cases} \dfrac{\partial \phi}{\partial t} = \operatorname{sgn}(\phi^0)(1-|\nabla \phi|) \\ \phi(x,0) = \phi^0(x) \end{cases} \tag{4.13}$$

where the sign function sgn( ) is defined as,

$$\operatorname{sgn}(\phi^0) = \begin{cases} 1 & if\ \phi^0 > 0 \\ 0 & if\ \phi^0 = 0 \\ -1 & if\ \phi^0 < 0 \end{cases} \tag{4.14}$$

The zero level set ϕ^0 denotes the front location. By iterating this equation till convergence, the result will approximate the signed distance function, and the zero level set of it is still the original level ϕ^0. Since (4.13) is a Hamilton–Jacobi type equation, the high order upwind schemes are preferred to discretize it, such as high order WENO scheme (Jiang & Peng, 2000). This reinitialization approach is a very useful method. It and its improvements (Russo & Smereka, 2000; Sussman & Fatemi, 1999) have been widely used with the level set method, for example in Nilsson and Bai (2000 & 2003), Peng et al. (1999), and as well as in this thesis work.

4.2 Deriving *G*-equation in LES framework

4.2.1 Previous work

A natural and general way to derive a governing equation for working in LES framework is by filtering the instantaneous equation directly, as we did to derive the filtered N–S equation (2.50) and *c*-equation (3.35). This way has also been taken by some researchers to derive *G*-equation in LES framework. Im (1995) applied the LES filtering to the instantaneous *G*-equation (4.7) and obtained

$$\frac{\partial \bar{G}}{\partial t} + \frac{\partial}{\partial x_j}\left(\bar{u}_j \bar{G}\right) = \frac{\partial}{\partial x_j}\left(\bar{u}_j \bar{G} - \overline{u_j G}\right) + \overline{s_L |\nabla G|} \tag{4.15}$$

Here, the two unclosed terms on the r.h.s. are subgrid flux term and propagation term, respectively. Im supposed that the contribution from these two terms can be represented by a turbulent flame propagating speed s_T, i.e.

$$\frac{\partial \bar{G}}{\partial t} + \frac{\partial}{\partial x_j}\left(\bar{u}_j \bar{G}\right) = s_T \left|\nabla \bar{G}\right| \tag{4.16}$$

where s_T is estimated by an algebraic formulation

$$s_T / s_L \approx 1 + C(u'/s_L) \tag{4.17}$$

Then, a dynamic modeling principle is used to determine the constant *C*.

Later, Im et al. (1997) revised this model by adding an additional diffusive term to the instantaneous *G*-equation (4.7) and modeling the two r.h.s. terms in (4.15) separately. Similar modeling approaches have been presented and used by Kim et al. (1999), Kim and Menon (2000), and Shinjo et al. (2003). For example, in Kim et al. (1999), equation (4.15) was modeled by

$$\frac{\partial \bar{G}}{\partial t} + \frac{\partial}{\partial x_j}\left(\bar{u}_j \bar{G}\right) = \frac{\partial}{\partial x_j}\left(\frac{\nu_t}{Sc_t}\frac{\partial \bar{G}}{\partial x_j}\right) + s_T \left|\nabla \bar{G}\right| \tag{4.18}$$

where ν_t is subgrid kinematic viscosity, Sc_t is the subgrid Schmidt number. In this formulation, the subgrid flux term is modeled with a gradient-diffusion concept. However, Peters (1999) and Oberlack et al. (2001) argued that this gradient-diffusion assumption cannot be used here, since it would result in an elliptic equation for $\bar{G}$ and contradict the parabolic character of the original *G*-equation.

Peters (1999) derived a *G*-equation, valid in both the corrugated flamelets regime and thin reaction zones regime, by only keeping the leading order terms in both regimes. These leading order terms, which have been identified by an asymptotic analysis, are the propagation term $s_L \left|\nabla G\right|$ in the corrugated flamelets regime and the curvature term $Dk\left|\nabla G\right|$ in the thin reaction zones regime; thereby it has a form as

$$\frac{\partial G}{\partial t} + \boldsymbol{u}\cdot\nabla G = s_L \left|\nabla G\right| - Dk\left|\nabla G\right| \tag{4.19}$$

where *D* is the molecular diffusivity, *k* is the curvature of an iso-surface of *G*. Appling the classical RANS averaging method, Peters obtained a modeling equation for the mean flame-front location

$$\frac{\partial \tilde{G}}{\partial t} + \tilde{\boldsymbol{u}}\cdot\nabla \tilde{G} = s_T \left|\nabla \tilde{G}\right| - D_T \tilde{k}\left|\nabla \tilde{G}\right| \tag{4.20}$$

This modeling equation derived in RANS framework has been extended to the LES framework without any modification, by some researchers, e.g. Pitsch and Duchamp (2002), and Duchamp and Pitsch (2002).

However, several researchers (Peters, 1999; Oberlack et al., 2001) have pointed out that for the derivation of a *G*-equation in RANS or LES framework, the traditional time averaging or spatial filtering procedure cannot be applied, since these two procedures require that *G* scalar has definition in entire field, which is not the fact.

Instead, Peters (2000) utilized a different averaging procedure to derive the modeling *G*-equation for the mean flame front in RANS. This averaging procedure is based on the probability density function of finding the flame surface at a particular location. Oberlack et al. (2001) found that the *G*-equation for premixed combustion admits some symmetries properties, such as the generalized scaling symmetry. However, the application of classical Reynolds averaging to *G* would lead to a contradiction to the generalized scaling symmetry property of *G*-equation; therefore, Oberlack et al. (2001) proposed a new averaging procedure to account for this generalized scaling symmetry, and derived a modeling equation for the averaged flame location. In the LES framework, Pitsch (2002) proposed a filter kernel that takes information only from the instantaneous flame surface. Thereafter, it is used to derive the *G*-equation for the filtered flame front location, which has a formulation as

$$\frac{\partial \tilde{G}}{\partial t} + \tilde{\boldsymbol{u}} \cdot \nabla \tilde{G} = \frac{\rho_u}{\bar{\rho}} s_{T,u} \left| \nabla \tilde{G} \right| \tag{4.21}$$

$$\frac{\partial \tilde{G}}{\partial t} + \tilde{\boldsymbol{u}} \cdot \nabla \tilde{G} = \frac{\rho_b}{\bar{\rho}} s_{T,b} \left| \nabla \tilde{G} \right| \tag{4.22}$$

In addition to the fact that *G*-equation is only valid on the instantaneous flame front, which precludes the application of usual spatial filtering, another phenomenon should also be addressed, that is the signed-distance function. As discussed above, the level set method is usually used together with the signed-distance function (4.9), which views the scalar *G* surrounding the front as the signed distance to the front. Since the signed distance function is well defined in the whole field, the usual filtering procedure can be applied on it; however, filtered scalar $\bar{G}$ does not satisfy the signed distance function anymore, since

$$\begin{gathered} \left|\nabla G\right| = 1, \quad \overline{\left|\nabla G\right|} = 1 \\ \bar{G} \neq G, \quad \left|\nabla \bar{G}\right| \neq \left|\nabla G\right|, \quad \left|\nabla \bar{G}\right| \neq 1 \end{gathered} \tag{4.23}$$

Similar relations have also been noticed and discussed in RANS time averaging procedure (Nilsson & Bai, 2003). For simplification, however, in most previous works (Chen et al., 2000; Pitsch & Duchamp, 2002; Duchamp & Pitsch, 2000), the filtered or averaged $\bar{G}$ is still assumed as the signed distance function, i.e.

$$\left|\nabla \bar{G}\right| = 1 \tag{4.24}$$

4.2.2 Present work

In this thesis work, we derive the *G*-equation in the LES framework directly, without recurring to the use of classical filtering or special designed filtering procedure. The derivation is purely based on the physical analysis. In Figure 4.2, the dashed line represents the instantaneous wrinkled laminar flamelet, and this laminar flame propagates at laminar flame speed s_L, to the unburnt gas and in the normal direction. In the corrugated flamelets regime, the Kolmogorov length scale is larger than the laminar flame thickness, and the interaction between the turbulent eddies and the advancing laminar flame is basically kinematic, i.e., the turbulent eddies only wrinkle the flame but not change the local flame structure.

In LES, turbulent eddies with length scale smaller than the filter size have been filtered out, therefore some small wrinkles of the flame front have been wiped out, i.e. the flame front becomes smoother and the area of flame surface decreases. In order to get the same consumption rate of the reactants, this smoother flame surface has to propagate at higher speed, s_{LES}. In Figure 4.2, the solid line shows schematically the smoothed flame.

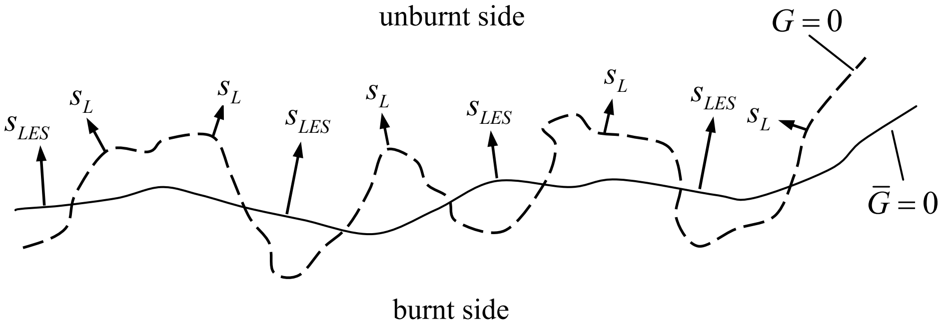

Figure 4.2 A sketch of the instantaneous laminar flame (dashed line) and the resolved smoothed LES flame (solid line).

Following the same process used to derive the instantaneous G-equation (4.7), an equation for the movement of this smoothed flame (located in the filtered flowfield) can be obtained

$$\frac{\partial \overline{G}}{\partial t}+\tilde{\boldsymbol{u}}\cdot\nabla\overline{G}=s_{LES}\left|\nabla\overline{G}\right| \tag{4.25}$$

Here, one point to be stressed is that $\overline{G}$ in (4.25) is not obtained from the general spatial filtering process. It is only a denotation of the smoothed flame front resolved in LES.

Similar to (4.7), (4.25) is only valid on the smoothed flame surface, $\overline{G}=0$. In this thesis, we define the surrounding $\overline{G}$-field as the signed distance to the smoothed flame surface,

$$\left|\nabla\overline{G}\right|=1 \tag{4.26}$$

In the G-equation based flamelet concept turbulent premixed combustion modeling approaches, the flamelet structure is often directly related to the physical distance to the instantaneous flame front (like the one used in this thesis work). However, $\overline{G}$ given by (4.26) is not the physical distance to the instantaneous flame front, but a distance to the LES smoothed flame front. This has a significant influence on predicting the minor species concentration. Its effect will be studied in Section 7.6, in which a subgrid scale wrinkling model is used to account for the difference between the physical distance and the $\overline{G}$ predicted by (4.26)

4.3 s_{LES} model

In addition to the effect of the difference between the physical distance and the $\overline{G}$ predicted by (4.26), another important effect has also to be accounted for, i.e. the enhanced propagating speed s_{LES}. Unlike the laminar flame propagation speed, which is a function of the local molecular transport of heat and mass between the preheat zone and the reaction zone, as well as the competition of different kinetic rates in the reaction zone, the subgrid burning speed s_{LES} strongly depend on the unresolved flame surface wrinkling. Flame surface wrinkling increases the burning area and thereby increases the propagation speed of the resolved flame surface.

In RANS framework, a similar term, s_T (it is generally called turbulent burning velocity) is defined from local mean quantities (Peters, 2000). Till today, a lot of models and expressions have been put forward to estimate s_T, for example it may be estimated with an algebraic expression (Peters, 1999), or with a dynamic process (Im, 1995).

A natural method is to extend those s_T models developed in RANS to LES directly. For example, in Duchamp and Pitsch (2001) the expression derived by Peters (1999) is applied to LES with some modifications. In this thesis work, the Damköhler derived model for the small-intensity, large scale turbulence (basically as the corrugated flamelet regimes) is used to estimate s_{LES}, which has a similar formulation as (3.6)

$$s_{LES} = s_L + u'_\Delta \tag{4.27}$$

where u'_Δ stands for the subgrid scale velocity fluctuation. u'_Δ is estimated as in Smagorinsky model

$$u'_\Delta = C_S \Delta \left(2\tilde{S}_{ij}\tilde{S}_{ij} \right)^{1/2} \tag{4.28}$$

C_S is a model constant and has to be adjusted for special case, Δ is the LES filter size, $\tilde{S}_{ij}$ is the resolved scale strain rate tensor. In the simulation of a lean premixed propane/air flame (described in detail in Chapter 7), it is found that C_S about 0.28–0.3 gives good agreement with the experimental data.

4.4 Flamelet library approach based on *G*-equation

In flamelet library approach, the turbulent flame is viewed as an ensemble of laminar flamelets, which are thin reactive-diffusive layers. If these layers are thinner than the Kolmogorov eddy size, their structures are not disturbed by the turbulent flowfield; hence they can be pre-calculated in a separate laminar flowfield calculation. In this section, the process for obtaining laminar flame structure is first explained, and then application of the structure to LES is described in detail.

4.4.1 Flamelet library generation

In this thesis work, the used laminar flamelet library for turbulent premixed combustion is obtained with the code developed by Mauss (1998), in which detailed chemical mechanisms, detailed transport and thermo-chemical data are applied. The system of transport equations for temperature and species are solved on the counter-flow configuration shown in Figure 4.3. In this configuration, fresh gases flows in against fresh gases, and two stretched flames are established. By this configuration, the effect of flame stretch and flame quenching is considered.

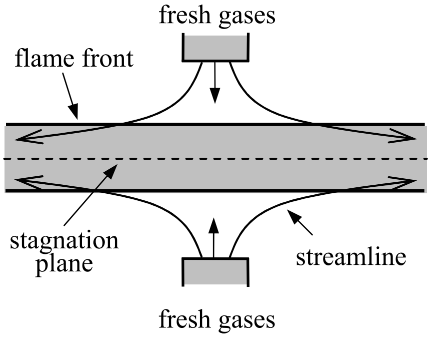

Figure 4.3 Counter-flow configuration.

After solving the transport equations, the laminar flame speed, temperature, species concentrations, and density distribution along the symmetric line, are obtained as functions of the physical coordinate. Specify a point of the physical coordinate as the flame position ($G=0$), these flame structure functions are then expressed as functions of *G* coordinate and the global flame stretch *k*. Since the intermediate species and some radical species usually have their maximal values in the inner layer, in this thesis work, we define the $G=0$ position at one of these radicals maximal concentration position, such as the CH_2O radical. The used flamelet library for a lean premixed propane/air flame is shown in Figures 3.1 and 3.2. In this thesis, these laminar structures are expressed as $Y_i(G,k), T(G,k), \rho(G,k)$, and so on. Since time is not explicitly included in the library as an independent variable, the present library approach is referred to as 'stationary flamelet library'. It is valid for fast chemistry.

LES result shows that mean flame structure (position, species concentrations) is not sensitive to the definition of the $G = 0$ position. This may be due to the fact that the laminar flame is much thinner than the used LES filter size.

4.4.2 Application of flamelet library in LES framework

The method for applying flamelet library in RANS framework is first described briefly. Figure 4.4 shows a sketch of some instantaneous flame fronts and the resolved time averaged flame front in RANS framework. On the right of Figure 4.4, it shows the pdf for finding instantaneous flame front at one point, which is denoted with a black dot on the left of Figure 4.4.

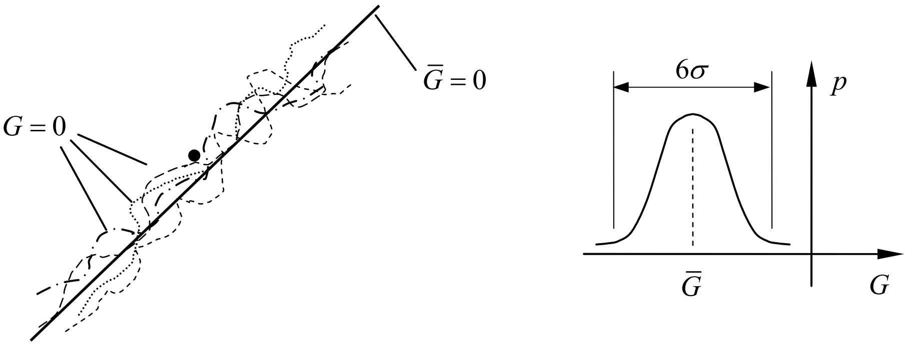

Figure 4.4 A schematic drawing of a turbulent premixed flame in RANS framework and the pdf of finding instantaneous flame front at one point.

If the pdf at one point is known, then a simple way to calculate the mean species concentration at one point is using formulation below (for simplicity, flame stretch is not included)

$$\tilde{Y}_i = \int_{-\infty}^{+\infty} \rho(G) Y_i(G) p(G) dG \Big/ \int_{-\infty}^{+\infty} \rho(G) p(G) dG \tag{4.29}$$

Generally, the shape of this pdf is presumed as a Gaussian type, i.e.

$$p(G) = \frac{1}{\sqrt{2\pi\sigma^2}} \exp\left(-\frac{1}{2}\left(\frac{G - \bar{G}}{\sigma} \right)^2 \right) \tag{4.30}$$

Here, $\sigma = \sqrt{G'^2}$ is the standard deviation of G, and $\bar{G}$ is the mean value of G. Both of them are schematically shown in Figure 4.4. The turbulent flame brush width (or time averaged mean flame thickness) may be estimated as 6σ. To close the problem, σ or the variance of G, σ^2, should provide. Till today, many models for estimating G variance in RANS framework have been presented, for example two algebraic expressions by Nilsson and Bai (2000), and Nilsson (2001).

$$\overline{G'^2} = C_v s_T^2 (\frac{k}{\varepsilon})^2 \tag{4.31}$$

$$\overline{G'^2} = (C_x x)^2 \tag{4.32}$$

A transport equation for *G* variance has also been derived by Peters (1999; 2000).

Applications of flamelet library approach based on level set *G*-equation, in RANS framework, are presented by Nilsson (2001) and Nilsson and Bai (2002), in which different s_T and *G* variance models have been tested, and additionally, a joint pdf for *G* and flame stretch is used to account for the effect of stretch on flame structure.

Extention of the laminar flamelet library to the LES framework is schematically shown in Figure 4.5. It shows a section of instantaneous flame and the corresponding smoothed LES flame, in a region of a filter size. As we deriving the *G*-equation for LES in Section 4.2.2, the laminar flame propagating speed s_L for instantaneous flame, is substituted by an enhanced propagating speed s_{LES} for the smoothed LES flame. The instantaneous flame surface area and the LES smoothed flame area are represented as A_T and A_m, respectively. To keep reactant consumption rate the same in both cases, a relation should be satisfied

$$\rho_u A_m s_{LES} = \rho_u A_T s_L \tag{4.33}$$

Here, the s_{LES} is assumed constant in the filter size region.

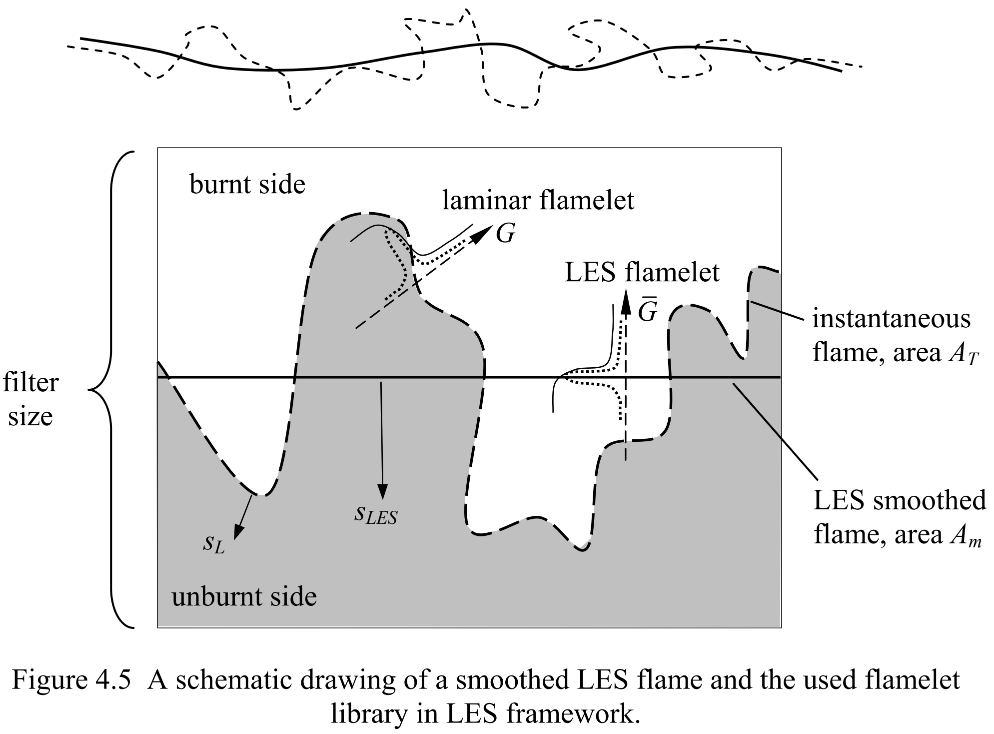

Figure 4.5 A schematic drawing of a smoothed LES flame and the used flamelet library in LES framework.

In Figure 4.5, a typical flamelet library for instantaneous flame is shown, where the solid curve represents density, major species, e.g. O_2, distribution along the normal direction of the instantaneous flame, whereas the dot line represents the distributions of intermediate species, e.g. CH_2O. A simple way to use the laminar flamelet in LES framework is assuming the flame structure of LES has the same profiles as that of instantaneous flame, i.e.

$$Y_i(\overline{G}) = Y_i(G), \quad \rho(\overline{G}) = \rho(G), \, ... \tag{4.34}$$

Now, let us consider the total mass in this filter size region calculated from two ways:

$$m_{ins} = \int \rho\left(G(x,y)\right) dxdy \tag{4.35}$$

$$m_{LES} = \int \rho\left(\overline{G}(x,y)\right) dxdy \tag{4.36}$$

Since the density profile has a shape like the step function (see Figure 3.2), the two total mass by (4.35) and (4.36) are determined by the area ratio between the one on unburnt side and the one on burnt side, which are

$$m_{ins.} = \int \rho\left(G(x,y)\right) dxdy \approx \rho_u \cdot S_{shadow} + \rho_b \cdot (S_{all} - S_{shadow}) \tag{4.37}$$

$$m_{LES} = \int \rho\left(\overline{G}(x,y)\right) dxdy \approx \rho_u \cdot S_{down} + \rho_b \cdot (S_{all} - S_{down}) \tag{4.38}$$

Here, S_{all} denotes the whole area of the box shown in Figure 4.5; S_{shadow} denotes the area in shadow below the instantaneous flame; S_{down} represents the area below the LES smoothed flame. As shown in Figure 4.5, it is easy to show that $S_{shadow} \approx S_{down}$. Hence, by (4.34), the total mass conservation is satisfied. Note that m_{LES} is proportional to the spatial filtered density (with a top-hat filter). Since other major species, e.g. O_2, CO_2, C_3H_8, have a step function like profiles as well, the spatial filtered (with a top-hat filter) species concentrations will not be sensitive to the details of the subgrid wrinkling.

Unlike the step function profile of major species, the profile of minor species are pulse-like: they only have value in a narrow region of the order of inner layer (around 0.5 mm), and outside of this layer, they are very low. The mass fractions of these minor species are mainly contributed from the narrow band region around the flame front. If we define the flame thickness as l_F, then the spatial filtered minor species will be proportional to the multiplication of l_F with the flame front area.

$$\tilde{Y}_{ins,\mathrm{CO}} = \int \rho\left(G(x,y)\right) Y_{\mathrm{CO}}\left(G(x,y)\right) dxdy \Big/ \int \rho\left(G(x,y)\right) dxdy \propto A_T l_F \tag{4.39}$$

$$\tilde{Y}_{LES,\mathrm{CO}} = \int \rho\left(\overline{G}(x,y)\right) Y_{\mathrm{CO}}\left(\overline{G}(x,y)\right) dxdy \Big/ \int \rho\left(\overline{G}(x,y)\right) dxdy \propto A_m l_F \tag{4.40}$$

In deriving (4.39) and (4.40), A_T and A_m are viewed as the length of flame surface, as in a two-dimensional planar area. Since A_T is much larger than A_m, the mass of CO obtained from (4.39) and (4.40) are very different.

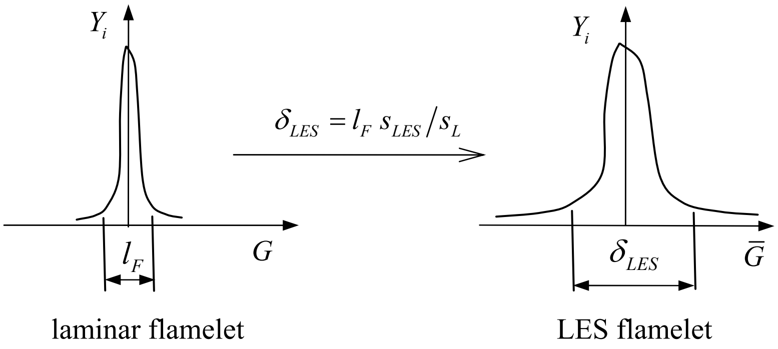

Figure 4.6 The relation between the laminar flamelet and the LES flamelet.

A way to remedy this problem is to increase the flame thickness of the local LES flamelet structure. From (4.39) and (4.40), it is found that the new thickness δ_{LES} should be A_T / A_m times l_F

$$A_T l_F = A_m \delta_{LES} \quad \rightarrow \quad \delta_{LES} / l_F = A_T / A_m \tag{4.41}$$

According to (4.33), a relation is obtained as

$$\delta_{LES} / l_F = s_{LES} / s_L \tag{4.42}$$

which is schematically explained with Figure 4.6.

Fortunately, the rescaled LES flamelet only changes the filtered minor species, but not the total mass and the major species. This is because the profiles of density and major species of the rescaled flamelet are still of step function shape, and hence, the arguments for deriving (4.37) and (4.38) are still valid.

The following is a summary of the flamelet library method used in this thesis.

- calculate a laminar flamelet library.
- calculate the density using the method described in Section 4.5 and couple it with the flowfield updating.
- during the flowfield calculation, save the instantaneous value of s_{LES} and $\bar{G}$.
- post-process the saved data to obtain the mean species concentration, mean temperature, and so on. In this step, the rescaled flamelet library (LES flamelet library, shown on the right of Figure 4.6) is used.

4.5 Filter function and explicit density filtering

In this thesis work, the SGS stress tensor is modeled with SSM, in which an explicit filter function is needed. The three types filter often used are the top-hat, Gaussian and the sharp Fourier cut-off filter (Piomelli, 1999). Formally, the filtering is applied from minus infinity to plus infinity, but in reality, the filter function should be truncated and discretized when applied in numerical simulation.

An approximate ‘Gaussian-type’ filter used in the simulations of Gullbrand et al. (2001) is used in this thesis work. On three-dimensional Cartesian grid system, it has the form:

$$\bar{\phi} = A\begin{pmatrix}\phi_{i-1}^{**}\\ \phi_{i}^{**}\\ \phi_{i+1}^{**}\end{pmatrix}, \qquad A = \frac{1}{6}(1\ \ 4\ \ 1), \qquad \phi_i^{**} = A\phi_i^{*}A^T \tag{4.43}$$

$$\phi_i^{*} = \begin{pmatrix}\phi_{i,j-1,l-1} & \phi_{i,j-1,l} & \phi_{i,j-1,l+1}\\ \phi_{i,j,l-1} & \phi_{i,j,l} & \phi_{i,j,l+1}\\ \phi_{i,j+1,l-1} & \phi_{i,j+1,l} & \phi_{i,j+1,l+1}\end{pmatrix} \tag{4.44}$$

where *i, j, l* are the index of grid cell. This discretized filter function $F()$ satisfies the normalization condition

$$\int_{-\Delta/2}^{\Delta/2}\int_{-\Delta/2}^{\Delta/2}\int_{-\Delta/2}^{\Delta/2} F(x_0 - x', y_0 - y', z_0 - z')dx'dy'dz' = 1 \tag{4.45}$$

and the realizability condition. The realizability condition is that the models should not give rise to physically unrealizable solutions, such as negative kinetic energy.

To apply this filtering process, the filter width should be set. Using a priori tests based on a DNS dataset of stably stratified shear flow, Chow and Moin (2003) showed that for a second order central difference scheme the filter width to grid spacing ratio (FGR) must be at least 4 to assure that the truncation errors are smaller than the SGS terms. An increase of FGR leads to an increase of the SGS terms, a smoothing-out of small scales and thereby smaller truncation errors. Given the third-order finite differencing scheme used in this thesis work (see Chapter 5), we choose to set the filter width to be two times of grid spacing, as commonly done in other LES applications.

The filtered continuity equation (2.49) contains a time dependent term $\partial\bar{\rho}/\partial t$. Since the instantaneous flame front is much thinner than the grid size, this term can be very large if the filtered density is calculated using *G* value at the grid point directly, i.e. $\bar{\rho} = \rho(G)$. For example, at one time step the grid point is on the burned side, its density is ρ_b, but at next time step, the flame front may cross the grid point, its density becomes ρ_u. This situation may be explained with a schematic drawing, Figure 4.7, in which the circles represent the grid cell center, where the density evaluated.

In the case shown in Figure 4.7, the maximum rate of density change is inversely proportional to the time step, that is

$$\left.\frac{\partial \bar{\rho}}{\partial t}\right|_{\max} = \frac{\rho_u - \rho_b}{\Delta t} \tag{4.46}$$

In addition to this, calculating density in this way is not consistent with the spatial filtering process, since $\bar{\rho}$ in the filtered continuity equation (2.49) represents a spatial averaged value, but not a local instantaneous value. In RANS this problem does not appear, since only the time averaged flame is solved, and the mean flame brush is much thicker than the grid size.

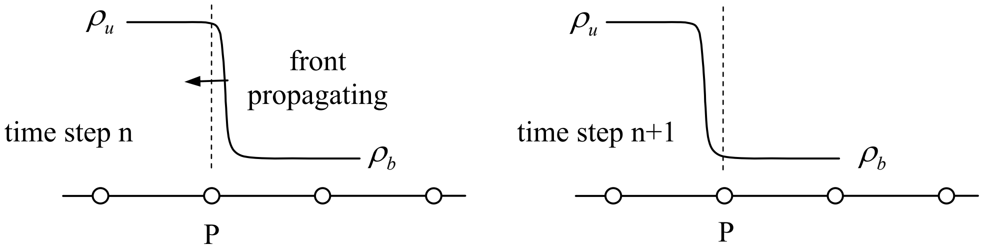

Figure 4.7 A schematic plot of flame front moving across a grid cell.

The velocity and pressure are coupled in the problem, thereby a false density change rate will result in a false pressure jump across the flame front. This is not good for the numerical stability. To remedy this, an explicit top-hat filter is applied to the density, with the filter width two times of grid size, i.e. $\bar{\rho} = \overline{\rho(G)}$.

$$\overline{\rho(x_0, y_0, z_0, t; \Delta)} = \frac{1}{\Delta^3}\int_{-\Delta/2}^{\Delta/2}\int_{-\Delta/2}^{\Delta/2}\int_{-\Delta/2}^{\Delta/2} \rho(x_0 - x', y_0 - y', z_0 - z', t; \Delta)dx'dy'dz' \tag{4.47}$$

This is a volume averaged density. In numerical simulation, the above formulation is approximated by subdividing the grid cells into a large number sub-cells, and then estimating the local density of every sub-cell using the flamelet library, $\rho(G)$; thus the filtered density $\overline{\rho(G)}$ is the mean value of these sub-cells' density. In this thesis work, a grid-cell is in general divided into $10 \times 10 \times 10$ sub-cells in three-dimensional problem. With this filtering procedure, the value of $\partial\bar{\rho}/\partial t$ is almost independent of the chosen time step, and it changes smoothly when flame front propagates across a grid cell. The effect of this method has been tested in a one-dimensional case, which is shown in Figure 4.8.

Suppose a flame front propagates from left to right, at a constant speed 5 m/s. Here, the horizontal axis show the index of grid cells, and the distance interval between them is the grid size, h=2 mm. ρ_u and ρ_b are 0.5858 kg/m^3 and 0.1793 kg/m^3, respectively, taken from a lean propane/air flame with equivalence ratio 0.6 and preheat temperature 600 K at atmospheric pressure. The time step Δt satisfies the Courant–Freidricks–Levy (CFL) condition, i.e.

$$\Delta t = \mathrm{CFL}\frac{h}{U} \tag{4.48}$$

Figure 4.8(a) shows a typical density profile with the explicit density filtering process, and its corresponding density changing rate is shown in Figure 4.8(b). From the movement of the curve in Figure 4.8(b), one can find a maximum value for $\partial\bar{\rho}/\partial t$, and a maximum integral value of it along the whole horizontal axis direction, which is expressed as

$$\Delta\dot{m} = \int \frac{\partial\rho}{\partial t}dx \tag{4.49}$$

This integration gives the difference of mass flux between the outflow and inflow during each time step, due to flame propagation. Adjusting the CFL number, a series of maximum values of $\partial\bar{\rho}/\partial t$ and its integral may be obtained. Table 4.1 lists the results obtained from two methods: one with the above explicit density filtering; another without this filtering.

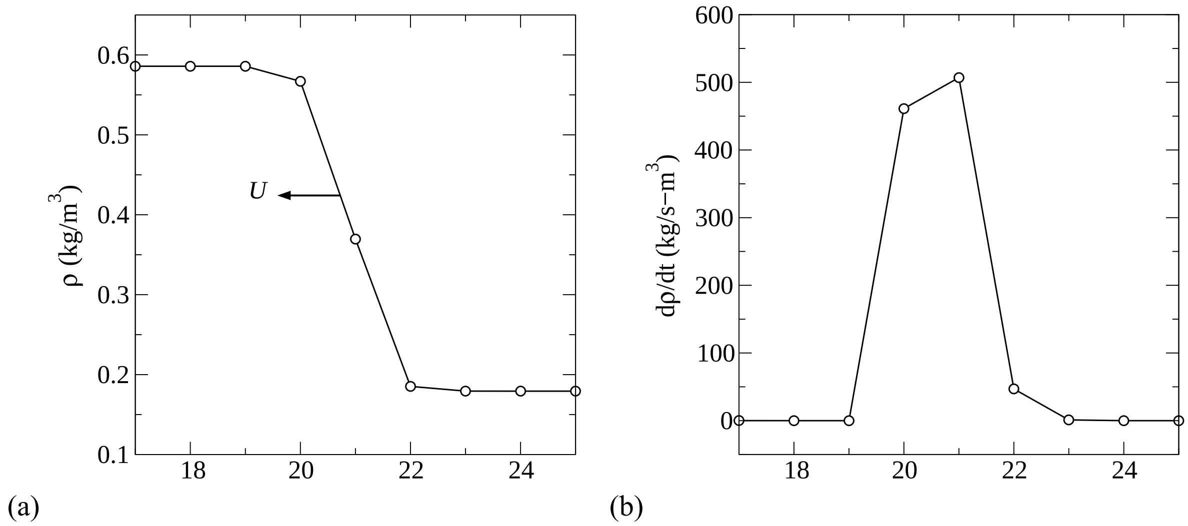

(a) (b)

Figure 4.8 A propagating flame front and its corresponding density changing rate.

It is seen that the values with explicit density filtering are almost independent of the time steps, which is physically right. Without explicit density filtering, both $\partial\bar{\rho}/\partial t$ and $\Delta\dot{m}$ depend on the time step chosen, which leads to wrong physical solution of the problem. The explicit density filtering method is good for the numerical stability and can remove most of the false pressure jump phenomenon across the flame front; thereby it is used in the premixed combustion simulations. A drawback of the method is the increased time consuming, about 20% more than that of calculation without filtering process.

Table 4.1 Maximum value of $\partial\bar{\rho}/\partial t$ (unity: kg/s-m^3) and $\Delta\dot{m}$ (unity: kg/s-m^2) at different time steps.

	CFL	0.01	0.02	0.05	0.07	0.1	0.2	0.5	0.7	1.0
with filtering	$\partial\bar{\rho}/\partial t$	516.8	516.7	514.4	511.4	508.1	508.0	507.7	507.4	493.2
	$\Delta\dot{m}$	2.07	2.067	2.057	2.046	2.033	2.033	2.033	2.032	2.033
no filtering	$\partial\bar{\rho}/\partial t$	4874	4843	4803	4720	4235	3751	1695	1384	998
	$\Delta\dot{m}$	9.774	9.75	9.65	9.5	8.52	7.54	3.45	2.83	2.03

Chapter 5

Numerical methods

In previous chapters a system of non-linear partial differential equations (PDE), for governing the flow field, are described. Analytical solutions to these non-linear partial differential equations are not possible for absolute majority flows. On the contrary, these PDE are usually discretized into a system of algebraic equations, and then solved numerically on a grid system. Due to the large amount of algebraic equations, an iteratively process is often used to solve these equations.

This chapter summarizes some aspects of the numerical methods used in this thesis work, including the discretization schemes, boundary conditions, solution algorithm and so on. Before doing these, the Favre filtering equations are repeated here,

$$\frac{\partial \overline{\rho}}{\partial t} + \frac{\partial \overline{\rho} \tilde{u}_j}{\partial x_j} = 0 \tag{2.49}$$

$$\frac{\partial \overline{\rho} \tilde{u}_i}{\partial t} + \frac{\partial \overline{\rho} \tilde{u}_i \tilde{u}_j}{\partial x_j} = -\frac{\partial \overline{P}}{\partial x_i} + \frac{\partial \overline{t_{ij}}}{\partial x_j} - \frac{\partial \tau_{ij}}{\partial x_j} \tag{2.50}$$

$$\tau_{ij} = \overline{\rho} \widetilde{\tilde{u}_i \tilde{u}_j} - \overline{\rho} \tilde{\tilde{u}}_i \tilde{\tilde{u}}_j \tag{2.53}$$

5.1 Grid system

The numerical method used in this thesis work is based on finite difference on a uniform, staggered Cartesian grid. A Cartesian grid is easy to generate and does not require much computational storage. In addition to this, high order discretization of PDE is relatively easier to construct on it than on other grid systems, such as body-fitted structured grid and unstructured grid. Local grid refinement technique is used to increase the grid resolution in the region of interest without increasing the total grid number greatly.

In a staggered grid, the velocity components and scalars are defined at different locations in a grid cell: velocity components are defined on the cell surface center and the scalars (e.g. pressure, density etc.) are defined on the cell center. As shown in Patankar (1980), staggered grid prevents the 'odd-even' decoupling between the pressure and velocity. Another advantage of the staggered grid is that no boundary condition of pressure is required.

5.2 Discretization schemes

A third order upwind scheme proposed by Kawamura and Kuwahara (1984) is used to discretize the convective terms in the momentum equations. The discretization scheme is

$$(u\frac{\partial\phi}{\partial x})_i=\begin{cases} u\dfrac{\phi_{i+2}-2\phi_{i+1}+9\phi_i-10\phi_{i-1}+2\phi_{i-2}}{6h} & u\geq 0\\ u\dfrac{-\phi_{i-2}+2\phi_{i-1}-9\phi_i+10\phi_{i+1}-2\phi_{i+2}}{6h} & u<0\end{cases}\qquad(5.1)$$

where *h* is the grid size, the subscript is index of grid cells. This third order scheme can be viewed as a combination of a fourth order central difference scheme and an additional term of third order,

$$u\frac{\partial u}{\partial x}=(u\frac{\partial u}{\partial x})_{4^{th}Cen}+\frac{1}{4}|u|h^3\frac{\partial^4 u}{\partial x^4}+O(h^4)\qquad(5.2)$$

The additional term (middle term on the r.h.s.) works as an artificial viscosity term, which dissipates the small scale energy. In this work, the SGS stress is modeled with SSM, which is described in Section 2.1.3. It is known that SSM is not absolutely dissipative, so it is usually used with a mixed model to provide enough dissipation. Here, the additional term in (5.2) can be used as an implicit mixed model. The effect of using truncation error as an implicit SGS model has been tested by Gullbrand et al. (2001).

All other spatial terms in the governing equations are discretized with fourth order central difference scheme.

$$(\frac{\partial^2\phi}{\partial x^2})=\frac{-\phi_{i-2}+16\phi_{i-1}-30\phi_i+16\phi_{i+1}-\phi_{i+2}}{12h^2}+O(h^4)\qquad(5.3)$$

The time derivative is discretized with a three time levels discretization,

$$(\frac{\partial\phi}{\partial t})=\frac{3\phi^{n+1}-4\phi^n+\phi^{n-1}}{2\Delta t}+O(\Delta t^2)\qquad(5.4)$$

where superscript *n* denotes the time level and Δt is the time step.

5.3 Boundary conditions

In this section, brief descriptions of high-order wall boundary, turbulent inlet condition, and convective outflow condition are given.

5.3.1 High-order wall boundary condition

At walls, the no-slip boundary condition is applied. In this thesis, the discretization of the governing equations is based on a Cartesian grid. It describes a curved surface boundary only approximately, if no special wall boundary treatment is used. In a low-order wall boundary treatment, a curve wall may be represented by piecewise step-walls. Gullbrand et al. (2001) developed a high-order wall algorithm for overcoming this drawback of Cartesian grid. It keeps the Cartesian grid at the wall, and applies the wall boundary condition at the exact wall location by using an interpolation/extrapolation procedure of the dependent variables. This high-order wall algorithm is described briefly below.

Three kinds of cells are defined, which are schematically shown in Figure 5.1. The ‘cut’ cells are those around the boundary and intersected with the boundary; the ‘active’ cells are within the flowfield and without intersection with boundary; the ‘wall’ cells are outside the flowfield and without intersection with boundary. In the calculations, the values of the dependent variables to the cut cells and some wall cells are determined from the values of active cells. For example, the velocity component at point P (defined at the cell’s surface center) is wanted. We draw a line normal to the boundary from P into the flowfield, which intersects with the boundary and grid cells at points X, C, B and A. The value for point P is then obtained by employing high order Lagrangian polynomial interpolation using the values of X, C, B and A. The values for points A, B and C are interpolated from the around active cells. At point X, the value is zero by the wall-boundary definition. This algorithm can be extended to provide wall boundary conditions for scalars such as species mass fraction, but the condition at point X should be changed to zero normal derivative.

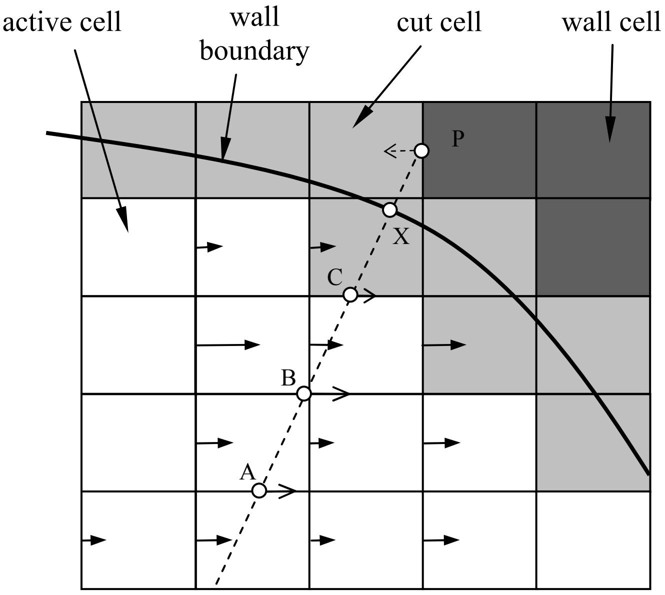

Figure 5.1 A sketch of the interpolation procedure in a high-order wall algorithm.

All coefficients used for interpolation/extrapolation are calculated only once, and then stored for later use. The effect of high-order wall boundary has been proven in many computations, such as in Gullbrand et al. (2001) and Wang et al. (2004a).

5.3.2 Turbulent inlet condition

LES requires a time dependent turbulent inflow condition since the simulated turbulent flow is time dependent. Such a ‘turbulent inflow condition’ is often absent from the measurements, thereby it must be generated in other numerical simulations or presumed following certain but limited measurement data.

Many inflow boundary conditions have been proposed and tested (Spalart, 1988; Lund et al., 1998; Klein et al., 2003). A simple method is to start the calculation with a laminar flow profile (without turbulent fluctuations); it evolves into ‘realistic’ turbulence after some distance downstream. This implies that the inlet must be located far away from the region of interest. An alternative way is to add some kind fluctuations to the laminar profile, for example white noise with certain scaling. More accurate turbulent inflow conditions can be obtained from an auxiliary simulation (Akselvoll & Moin, 1996) or by use of periodic boundary conditions (Spalart, 1988). Klein et al. (2003) presented a novel approach for generating artificial velocity data which reproduces the first and the second order one-point statistics as well as a locally given auto-correlation function. Pierce and Moin (1998a) presented a ‘body force’ method to generate equilibrium swirling inflow condition, in which an axial- and an azimuthal-body force are added to the momentum equations. The axial force represents the mean pressure gradient that drives the main flow; the azimuthal body force overcomes the drag from the walls and drives the azimuthal flow.

In this thesis work, a so-called ‘rescaled inflow library’ condition is used. First, the above ‘body force’ method (Pierce & Moin, 1998a) is used to generate inflow turbulence for the main test section, and the LES data at a middle cross section is stored to form a library of the instantaneous velocity. The velocity library, then, is rescaled to create the needed inlet flow instantaneous velocity that satisfies the measured statistics properties (the mean and the variances). For instance, if the original database from the velocity library u_{ori} has a mean value of U_{ori} and r.m.s velocity fluctuation u'_{ori}, the rescaled new inflow velocity u_{new} with a new mean value U_{new} and a new r.m.s. velocity fluctuation u'_{new}, can be calculated as the following:

$$u_{new} = U_{new} + (u_{ori} - U_{ori}) \frac{u'_{new}}{u'_{ori}} \tag{5.5}$$

This inflow condition reproduces the measured Reynolds normal stresses and turbulent kinetic energy, but not the shear stresses. To obtain physically realistic statistics at the inflow, the inflow library should contain sufficient number of time steps. 10 000 time steps are used in this work. When the LES time step exceeds 10 000, the inflow library is repeated from the starting first time step.

5.3.3 Outflow condition

A mass-conserving convective outflow condition is used in this thesis work. The same condition was used in the previous LES of a confined co-annular jet flow (Akselvoll & Moin, 1996), diffusion flames (Pitsch & Steiner, 2000), and premixed flames (Pitsch & Duchamp, 2002). The following equation is solved to obtain the convective outflow boundary condition:

$$\frac{\partial \tilde{u}_i}{\partial t} + U_{con} \frac{\partial \tilde{u}_i}{\partial n} = 0 \tag{5.6}$$

where U_{con} is the mean outflow velocity integrated across the outlet plane; n is the normal direction to the outlet plane. According to Akselvoll and Moin (1996), this condition had no visible effect on the flow statistics up to a short distance upstream of the exit.

In Section 6.3.1 (also cf. Wang & Bai, 2005), this convective outflow condition is compared with an often-used zero-gradient outflow condition, in which the gradient of the dependent variables are assumed to be zero in the main flow direction. The simulations of swirling flows show that results based on the convective flow condition are slightly closer to the experimental data than the results from the ‘zero gradient’ condition.

5.4 Solution algorithm

Using the algorithm (5.1), (5.3) and (5.4) to discretize the u moment equation, one obtains a equation

$$\begin{aligned} \frac{3(\rho u_1)^{n+1} - 4(\rho u_1)^n + (\rho u_1)^{n-1}}{2\Delta t} + D_j^u(\rho u_1 u_j)^{n+1} &= -D_1^c(\overline{P})^{n+1} \\ &\quad + \underbrace{D_j^c(\tau_{1,j})^{n+1} + D_j^c(\overline{t}_{1,j})^{n+1}}_{S^{n+1}} \end{aligned} \tag{5.7}$$

Here, D_j^u and D_j^c represent the third-order upwind and fourth-order central difference schemes, respectively. For convenience, the last two terms on the r.h.s. of (5.7) are denoted as S^{n+1}. At every time step, equation (5.7) has to be solved to a converged state. In this thesis, this is achieved by updating u_i^n to u_i^{n+1} in an iterative process

$$\begin{matrix} u_1^n \to u_1^m \to \cdots \to u_1^{n+1} \\ (\rho u_1)^{m+1} = (\rho u_1)^m + \Delta \rho u_1 \end{matrix} \qquad \begin{cases} m = 1, \cdots, M & \\ m = 1 & (\rho u_1)^m = (\rho u_1)^n \\ m = M & (\rho u_1)^m = (\rho u_1)^{n+1} \end{cases} \tag{5.8}$$

Thus (5.7) can be expressed as

$$\begin{aligned}&\underbrace{-\frac{3\Delta\rho u_1}{2\Delta t} - D_j^u(u_j\Delta\rho u_1) + S(\Delta\rho u_1)}_{L_u\Delta\rho u_1} - D_1^c(\Delta P)\\ &= \underbrace{\frac{3(\rho u_1)^m - 4(\rho u_1)^n + (\rho u_1)^{n-1}}{2\Delta t} + D_j^u(\rho u_j u_1)^m + D_i^c(\bar{P})^m - S({u_1}^m)}_{R_u}\end{aligned} \tag{5.9}$$

Three equations in this form can be obtained for the three momentum equations. For the continuous equation, a similar form can be written as

$$D_j^c(\Delta\rho u_j) = \underbrace{-\frac{3\rho^m - 4\rho^n + \rho^{n-1}}{2\Delta t} - D_j^c(\rho u_j)^m}_{R_m} \tag{5.10}$$

With the expressions of (5.9) and (5.10), the whole PDE system can be rewritten in a matrix form as (considering only the continuity and momentum equations)

$$L\Delta\Phi = R \tag{5.11}$$

Here, *L* represents the discrete operator matrix as

$$L = \begin{bmatrix} L_u & 0 & 0 & -D_1^c \\ 0 & L_v & 0 & -D_2^c \\ 0 & 0 & L_w & -D_3^c \\ D_1^c & D_2^c & D_3^c & 0 \end{bmatrix} \tag{5.12}$$

and $\Delta\Phi$ and *R* represent

$$\Delta\Phi = \begin{bmatrix} \Delta\rho u \\ \Delta\rho v \\ \Delta\rho w \\ \Delta P \end{bmatrix}, \qquad R = \begin{bmatrix} R_u \\ R_v \\ R_w \\ R_m \end{bmatrix} \tag{5.13}$$

$\Delta\Phi = \Phi^{m+1} - \Phi^m$ is the correction of the dependent variables between the iteration step *m* and *m*+1. *R* is residual of the system at the *m*:th iteration. In this thesis, a distributed Gauss–Seidel scheme (Brandt, 1977) is used to decouple the velocity field and the pressure. $\Delta\Phi$ is substituted by

$$\Delta\Phi = \begin{bmatrix} 1 & 0 & 0 & D_1^c \\ 0 & 1 & 0 & D_2^c \\ 0 & 0 & 1 & D_3^c \\ 0 & 0 & 0 & L_u \end{bmatrix} \Delta\Phi^* \tag{5.14}$$

where $\Delta\Phi^* = (\Delta\rho u^*, \Delta\rho v^*, \Delta\rho w^*, \sigma)$. If L_u, L_v and L_w are identical, from (5.11)–(5.14), one obtains

$$\begin{bmatrix} L_u & 0 & 0 & 0 \\ 0 & L_v & 0 & 0 \\ 0 & 0 & L_w & 0 \\ D_1^c & D_2^c & D_3^c & Q \end{bmatrix} \Delta\Phi^* = R \tag{5.15}$$

where $Q = (D_{xx}^c + D_{yy}^c + D_{zz}^c)$ and D_{xx}^c, D_{yy}^c and D_{zz}^c are central difference operators for the second spatial derivatives in the direction x, y, and z, respectively. In (5.15), the velocity and pressure are not coupled, and then the system of the discretized equations on the computational domain is solved with a point-wise, symmetric Gauss–Seidel relaxation scheme.

To accelerate the convergence, multigrid method is applied. It is known that the conventional iteration methods, such as point-wise Gauss–Seidel relaxation, are effective in reducing the high frequency errors, but are less effective in removing the low frequency errors. The low frequency errors have a character that their wave lengths are many times larger than the grid length. In multigrid method, a system of fine and coarse grids is used to reduce both high and low frequency errors.

On the finest grid level, the discretized governing equations are resolved iteratively. Those high frequency errors (relative to the finest grid length) are efficiently smoothed on this level, but those low frequency errors are still there. Then, the solutions on the finest level are transferred to the next coarser grid level. On that level, the low frequency error on the finest level becomes relatively high frequency (the ratio of wave length to grid length decreases), so it can be smoothed out efficiently. For even lower frequency errors, coarser grid levels can be used to smooth them out efficiently. Then the solution on the coarse levels are transferred back to correct the solution on the finest level. The multigrid process can be described in the following way.

Create a sequence of grid levels, by doubling the grid length in every direction of the Cartesian system, and denote the grid level by q; q=1 for the coarsest level and q=M for the finest level. Write the discretized system of equations on the finest level as

$$L^q \phi^q = R^q \qquad (q = M) \tag{5.16}$$

L^q is the discrete operator; ϕ^q is the dependent variable; R^q represents the residual. After some iterations, solution on the finest level is obtained, which is denoted as ϕ^q. Then, this solution is transferred to next coarser level by a restriction process. As the governing equations are nonlinear, the full approximate storage (FAS) scheme is used, in which both the residual and the solution have to be transferred. This can be written as

$$R^q = L^q I_{q+1}^q \phi^{q+1} + I_{q+1}^q (R^{q+1} - L^{q+1}\phi^{q+1}) \qquad (q < M) \tag{5.17}$$

where I_{q+1}^{q} is the restriction operator (from q+1 level to q level). The first term on the r.h.s. is the contribution from the restricted solution, and the second term on the r.h.s. is the restricted residual from finer level. After relaxations are made on this level, the solution is restricted to next coarser level. Repeat this until the coarsest level is reached. Thereafter, the solutions on the coarser level are prolongated to finer grid level.

$$\phi^{q+1} \leftarrow \phi^{q+1} + P_{q}^{q+1}(\phi^{q} - I_{q+1}^{q}\phi^{q+1}) \qquad (2 \le q+1 \le M) \tag{5.18}$$

Here, P_{q}^{q+1} is the prolongation operator (from q level to q+1 level). Repeat this prolongation till the finest level is reached.

5.5 Parallel computation

In the code for swirling flows simulation, Message Passing Interface (MPI) technique is used to parallelize the computation. At the interface boundary, variables in 6 grid cells in each Cartesian coordinate direction are exchanged between the two neighboring processors during the calculation. From many computation cases, it is found that the communication process takes about 5% of the total computation time.

5.6 Numerical discretization of level set *G*-equation

In this section, some aspects about the implementation of level set *G*-equation in LES are addressed in detail, including the WENO scheme used to discretize the level set and signed-distance equations. The two governing equations dealt with in this section are repeated below

$$\frac{\partial G}{\partial t} + \boldsymbol{u} \cdot \nabla G = s_{LES}\left|\nabla G\right| \tag{5.19}$$

$$\frac{\partial G}{\partial t^{*}} = \mathrm{sgn}(G^{0})(1 - \left|\nabla G\right|), \qquad G(r,0) = G^{0}(r) \tag{5.20}$$

Equation (5.19) is the governing equation for flame front movement, while (5.20) is for reinitializing the surrounding *G*-scalar to a signed-distance function. Here, t^{*} in (5.20) is not a physical time. Since both of them are Hamilton–Jacobi type equation, their unique ‘viscosity solution’ can be approached by using upwind schemes (Levy et al., 2002). A type of effective high-order upwind schemes is based on the ENO scheme.

5.6.1 WENO scheme

ENO scheme was first developed by Harten et al. (1987), whose key idea is to use the ‘smoothest’ stencil among several candidates to obtain high order accuracy fluxes at cell boundaries and at the same time to remove spurious oscillations near shocks (Jiang & Shu, 1996). A general framework for constructing high-order ENO schemes for Hamilton–Jacobi equations can be found in Osher and Shu (1991). WENO scheme was first introduced by Liu et al. (1994), which is a central scheme when the solution is smooth, whereas it is ENO schemes near the singularities of the solution. This is achieved by weighting the stencils of the base ENO scheme with the weights according to the local smoothness of the solution. For example, in Jiang and Peng (2000), a fifth-order WENO scheme was constructed based on the third order ENO. A review for the construction, analysis, and application of both ENO and WENO scheme is given by Shu (1997). Since in this thesis work, the discretization schemes for the filtered N–S equations are of third-order accuracy (see Section 4.2), a third-order WENO scheme (Jiang & Peng, 2000) based on a second-order ENO scheme is used to discretize the gradient terms in the above two equations.

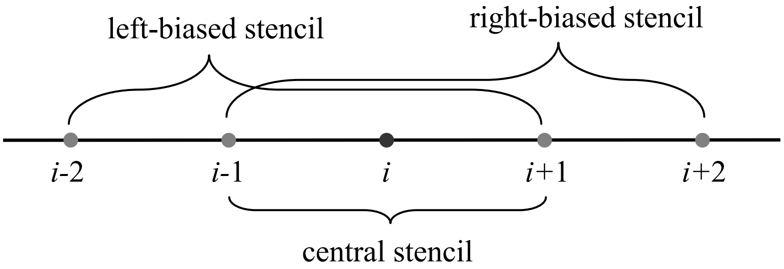

Figure 5.2 The stencils for third-order WENO scheme.

This third-order WENO scheme can be expressed as a central discretization scheme with an upwind biased corrector. In one dimensional, the approximation to gradient $\partial G/\partial x$ can be explained with Figure 5.2, in which the grid points are uniformly distributed with spacing h. Here, we introduce operator $\Delta^+[G_i]$ and $\Delta^-[G_i]$ as

$$\Delta^+[G_i] = G_{i+1} - G_i \tag{5.21}$$

$$\Delta^-[G_i] = G_i - G_{i-1} \tag{5.22}$$

The left-biased upwind approximation to $\partial G/\partial x$ is expressed as

$$\begin{aligned} G_{x,i}^- &= \frac{1}{2}\left(\frac{\Delta^+[G_i]}{h} + \frac{\Delta^-[G_i]}{h}\right) - \frac{b^-}{2}\left(\frac{\Delta^+[G_{i-2}]}{h} - 2\frac{\Delta^+[G_{i-1}]}{h} + \frac{\Delta^+[G_i]}{h}\right) \\ &= \frac{1}{2h}(G_{i+1} - G_{i-1}) - \frac{b^-}{2h}(-G_{i-2} + 3G_{i-1} - 3G_i + G_{i+1}) \end{aligned} \tag{5.23}$$

By symmetry, the right-biased upwind approximation to $\partial G/\partial x$ is

$$G_{x,i}^+ = \frac{1}{2h}(G_{i+1} - G_{i-1}) - \frac{b^+}{2h}(G_{i+2} - 3G_{i+1} + 3G_i - G_{i-1}) \tag{5.24}$$

In these two equations, b^- and b^+ are weights for the upwind contributions, estimated by

$$b^+ = \frac{1}{1+2r_+^2}, \qquad b^- = \frac{1}{1+2r_-^2} \tag{5.25}$$

where r_+ and r_- are coefficients used to determine the solution's 'smoothness' and they are defined as

$$r_+ = \frac{\varsigma + (\Delta^-\Delta^+[G_{i+1}])^2}{\varsigma + (\Delta^-\Delta^+[G_i])^2}, \qquad r_- = \frac{\varsigma + (\Delta^-\Delta^+[G_{i-1}])^2}{\varsigma + (\Delta^-\Delta^+[G_i])^2} \tag{5.26}$$

Here, ς is a small number used to prevent the denominators from becoming zero.

With the formulations of (5.23) and (5.24), the absolute value of gradient of G, and the convective term in (5.19) are calculated as

$$\begin{aligned} |\nabla G|^2 = \; & \max\left[\min(G_{x,i}^-,0)^2, \max(G_{x,i}^+,0)^2\right] \\ & + \max\left[\min(G_{y,j}^-,0)^2, \max(G_{y,j}^+,0)^2\right] \\ & + \max\left[\min(G_{z,k}^-,0)^2, \max(G_{z,k}^+,0)^2\right] \end{aligned} \tag{5.27}$$

$$\begin{aligned} \boldsymbol{u} \cdot \nabla G = \; & \max(u,0)\, G_{x,i}^- + \min(u,0)\, G_{x,i}^+ \\ & + \max(\upsilon,0)\, G_{y,j}^- + \min(\upsilon,0)\, G_{y,j}^+ \\ & + \max(w,0)\, G_{z,k}^- + \min(w,0)\, G_{z,k}^+ \end{aligned} \tag{5.28}$$

where $G_{y,j}^{\pm}$ and $G_{z,k}^{\pm}$ are biased upwind approximation to $\partial G/\partial y$ and $\partial G/\partial z$ in y and z direction, respectively, which can be estimated with similar formulations as (5.23) and (5.24).

5.6.2 Total variation diminishing Runge–Kutta scheme

For time discretization of (5.19) and (5.20), a so-called total variation diminishing (TVD) type Runge–Kutta scheme is used. The Runge–Kutta schemes are often used to discretize the rate of change term in the ordinary differential equations

$$\frac{\partial \phi}{\partial t} = L(\phi) \tag{5.29}$$

Generally, the Runge–Kutta methods have a form as that in Shu and Osher (1988)

$$\begin{cases} \phi^{(i)} = \sum_{k=0}^{i-1} \left(A_{ik}\phi^{(k)} + \Delta t B_{ik} L(\phi^{(k)}) \right), & i = 1, \ldots, m \\ \phi^{(0)} = \phi^n, \qquad \phi^{(m)} = \phi^{n+1} \end{cases} \tag{5.30}$$

Total variation of the numerical solution is defined as

$$TV(\phi) = \sum_i |\phi_{i+1} - \phi_i| \tag{5.31}$$

which is written in one-dimension. A TVD spatial discretization has a property that the total variation does not increase, i.e.

$$TV(\phi^{n+1}) \le TV(\phi^n) \tag{5.32}$$

for the first-order Euler time advancing method.

The high-order TVD Runge–Kutta time advancing scheme is designed to maintain the TVD property as (5.32) and at the same time to achieving high-order accuracy in time advancing. It is demonstrated in Gottlieb and Shu (1998) that it is always safer to use TVD type Runge–Kutta time discretization methods for hyperbolic problems, since non-TVD but linearly stable Runge–Kutta method may not eliminate oscillatory even with a TVD spatial discretization. Gottlieb and Shu (1998) proved that the optimal third-order three-stage TVD Runge–Kutta method has a form as:

$$\begin{cases} \phi^{(1)} = \phi^{(n)} + \Delta t L(\phi^{(n)}) \\ \phi^{(2)} = \frac{3}{4}\phi^{(n)} + \frac{1}{4}\phi^{(1)} + \frac{1}{4}\Delta t L(\phi^{(1)}) \\ \phi^{(n+1)} = \frac{1}{3}\phi^{(n)} + \frac{2}{3}\phi^{(2)} + \frac{2}{3}\Delta t L(\phi^{(2)}) \end{cases} \tag{5.33}$$

This formulation is implemented in this thesis work for time integration of (5.19) and (5.20).

Till now, the TVD type Runge–Kutta time discretization methods have been widely used in combination with the level set methods, for example in Tsai and Osher (2003), Barth and Sethian (1998), Duchamp and Pitsch (2002), and Peng et al. (1999).

5.6.3 Reinitialization process

- **Narrow band method**

By solving (5.19), the level sets are updated, and the zero level set is renewed. To reshape the surrounding *G*-field as a signed-distance function, equation (5.20) is then solved till a steady state. Both processes are very time consuming, if they are solved in the entire computational domain. Fortunately this computational work can be dramatically decreased by the so-called narrow band method, in which both updating and reinitializing processes are only done in a narrow band (or a tube) around the front surface. It is feasible because the entire *G*-field movement is only controlled by the advancing of the zero level set, which only requires a neighborhood grid cells around the zero level set, and the range of this neighborhood depends on the discretization schemes used for solving (5.19) and (5.20). Since this idea was first presented by Chopp (1993), it has been widely applied in the level set methods (Tsai & Osher, 2003; Sethian & Smereka, 2003).

In this work, since a third-order WENO scheme is used to discretize (5.19) and (5.20), the width of narrow band is chosen in the range of 5–6 grid cells at each side of the zero level set, in each coordinate direction. The *G*-value of those grid cells outside the narrow band are set to a large signed value. For one dimension problem, this can be explained with Figure 5.3.

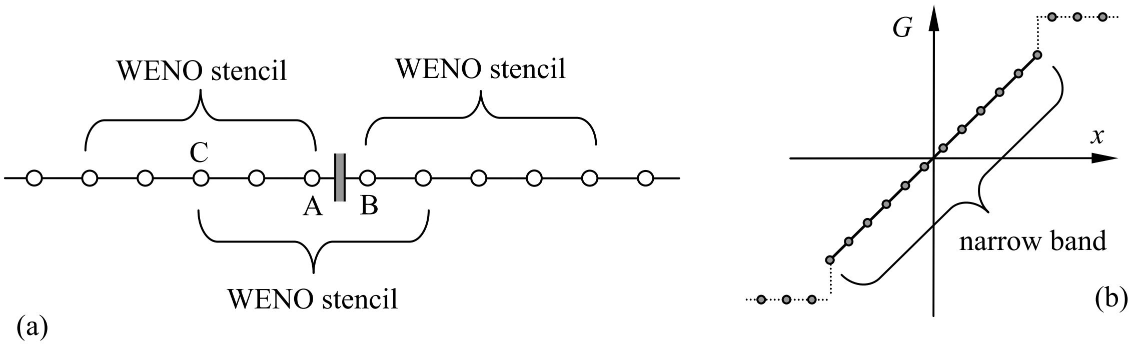

Figure 5.3 A schematic illustration of the narrow band method.

In Figure 5.3(a), in order to apply third-order WENO scheme on the front neighbor cell A, two grid cells are needed on both side (see Figure 5.2). Additionally, for preserving accuracy, the third-order WENO scheme should also be used to calculate the value on grid C. Hence, at least five grid cells are needed on the left side. This is also true for the right side. Figure 5.3(b) shows a result of the reinitialization with narrow band method: inside the narrow band, it satisfies a signed distance function; outside of it, it is set to a large constant value.

- **Sub-cell fix method**

During the signed-distance reinitialization, a key issue is to guarantee that the zero level set of the reinitialized *G*-field coincides with the original one. However, this is not always the fact, when one conducts reinitialization by solving the partial differential equation (5.20). This problem has been addressed by several authors, for example Russo and Smereka (2000), Sussman and Fatemi (1999), and Peng et al. (1999). One method to decrease this disturbance to the original front position is by use high order discretization schemes. Another possible way, as said in Sethian (2001), is to limit the using of reinitialization. This idea has been used in Hou et al. (1997) and Peng et al. (1999), in which the reinitialization was conducted at some time step interval instead of at every time step. In Peng et al. (1999), the reinitialization is triggered automatically under some conditions.

For numerical purposes, the sign function in (5.20) is not calculated by the definition as in formulation (4.14), but by a smoothed sign function (Sussman et al., 1994)

$$\mathrm{sgn}(G^0) = G^0 \Big/ \sqrt{(G^0)^2 + \varsigma^2} \tag{5.34}$$

It is shown that this sign function may suffer from a difficulty when the initial level set is far away from the signed distance function. To solve this problem, a modified sign function is proposed by Peng et al. (1999) as

$$\operatorname{sgn}(G^0) = G^0 \Big/ \sqrt{(G^0)^2 + |\nabla G^0|^2 h^2} \tag{5.35}$$

In Sussman and Fatemi (1999), a constraint is designed to prevent the disturbance to the original front position during reinitialization, which results in a transformed reinitialization equation.

A so-called sub-cell fix method is proposed by Russo and Smereka (2000). The main idea of it is to use a truly upwind discretization near the interface, which is consistent with the upwind property of (5.20), i.e. the information on the front can only transformed to outside, and no information can across the front. To do this, Russo and Smereka proposed to calculate the derivatives of those sub-cells (immediately by the front) with

$$\nabla G \approx \frac{G}{D^*} \tag{5.36}$$

where D^* is an approximation of the signed distance to the front, which is only needed to calculate once at the beginning of reinitialization. For more detailed information please turn to Russo and Smereka (2000). This sub-cell fix method is improved further with a simple modification to treat the anisotropic grids (Nilsson & Bai, 2003). Because of its simple formulation and good performance, this improved sub-cell fix reinitialization method is used in this thesis work.

Chapter 6

LES of turbulent swirling flows in a dump combustor

6.1 Swirling flows and vortex breakdown phenomena

Swirling flows are important and widely used in energy production devices such as gas turbine combustors, internal combustion engines, industrial burners and boilers, for example, in the EV burner and DLE burner, swirling flows are used to provide high mixing rate and to stabilize the flames, see Figure 1.2 and Figure 1.3. Due to their wide applications, they have attracted extensive research efforts for decades. Experimental (Billant et al., 1998; Panda & Mclaughlin, 1994), theoretical (Wang & Rusak, 1996; Fernandez & Ortega, 1999) and numerical (Kubo & Gouldin, 1975; Nejad et al., 1989; Weber et al., 1990) investigations of swirling flows have been reported.

The swirling motion at the inlet is often generated using guide vanes, inlet tangential flow injections or by other means. It is known that an internal recirculation zone (IRZ), which is often referred to as vortex breakdown phenomenon in fluid mechanics, appears when the strength of swirl is high enough. For the premixed combustion, especially the LP combustion, IRZ can hold the hot combustion products and radicals and enhance the flame anchoring to the recirculation zone. In the non-premixed combustion, IRZ promotes a more efficient fuel/air mixing and a higher intensity of combustion. Because of its important influence on the flame shape, flame stability and heat release rate, as well as emission, development and improvement of modern combustion chambers demand a deeper understanding of the fundamental physics and appropriate numerical simulations of turbulent swirling flows.

Experimental studies on the formation of IRZ have been carried out for different flow configurations, for example, vortex whistles and model cyclone separators (Chanaud, 1965), jet flows (Ribeiro & Whitelaw, 1980; Mehta et al., 1991; Huang & Tsai, 2001; Champagne & Kromat, 2000), and confined pipe flows (Kitoh, 1991; Weber et al., 1990; Ahmed, 1998). A recent review has been given by Lucca and O'Doherty (2001), who summed up seven different patterns of vortex breakdown, of which two forms, the bubble and the spiral type breakdown, are typically found in high Reynolds number turbulent flows. A complex and less understood phenomenon found experimentally in confined swirling flows is the unsteady and periodic motion of large-scale well-organized structures, coherent structures (Gupta et al., 1984; Gouldin et al., 1984; Coats, 1996; Paschereit et al., 1999). One example is the so-called low frequency precessing vortex core (PVC), which is frequently observed at high Reynolds numbers and high swirl numbers near the IRZ (Cassidy & Falvey, 1970; Gupta et al., 1984;

Gouldin et al., 1984). Since vortex breakdown is often very sensitive to external disturbances such as the introduction of the probe (Harvey, 1962), LDV technique is more preferable than those intrusive methods, such as hot-wire. However, because of the difficulty of the optical access, detailed LDV measurement in practical gas turbine combustors is seldom.

In addition to the experimental studies, many theoretical analyses have been carried out, which are mainly focused on the instabilities and the onset of vortex breakdown (Wang & Rusak, 1996; Lopez, 1994; Serre & Bontoux, 2002). Studies have been reported on the influence on swirling flows by different parameters such as the level of swirl, the inflow profiles (e.g. the Rankine vortex, the free vortex, or the solid-body rotation), the flow configurations (the shape of the swirl generator, the geometry of the confining walls) and Reynolds numbers, etc., see the recent review by Lucca and O'Doherty (2001) and the references therein.

Numerical simulation of swirling flows is a very important tool to assist experiments to gain deep understanding of the fundamental flow physics, since the experiments are often limited due to practical reasons to a few discrete positions and thereby do not provide a whole three dimensional structure. Numerical simulation of turbulent swirling flows is yet a challenging task.

In swirling flows large velocity gradient appears; the turbulent flow is highly anisotropic in the IRZ and decays quickly downstream. Several authors have applied conventional RANS models to simulate the free-jet and confined swirling flows (Weber et al., 1990; Kubo & Gouldin, 1975; Sharif & Wong, 1995; Jakirlic et al., 2000; Xia et al., 1998). It has been shown that the $k-\varepsilon$ turbulence model is inadequate for simulation of strong swirling flows (Kubo & Gouldin, 1975; Nejad et al., 1989). This is due to the fact that the $k-\varepsilon$ turbulence model is based upon the Boussinesq hypothesis; it does not take into account the effect of the rotational motion.

Weber et al. (1990) tested three turbulence models in a simulation of confined turbulent swirling flows: a $k-\varepsilon$ model, a RSM and an ASM. It was shown that RSM and ASM perform better than the $k-\varepsilon$ model. Modification of RSM simulations of swirling flows has been attempted recently. For example, Lu and Semião (2003) showed successful simulations of confined swirling flows by using an improved RSM model, in which an anisotropic dissipation rate model was used for calculation of turbulent kinetic energy and a non-linear model for the pressure-strain correlation.

A better approach to handle the anisotropic and highly dynamic character of turbulent swirling flows is the LES. With a fine spatial- and temporal-resolution, the dynamics of turbulent swirling flow such as the oscillatory PVC motion is hopefully captured in LES. Most previous LES have been focused on the so-called 'building-block' flows such as channel flows, boundary layer flows or free-jet flows (Piomelli 1999). Till now, only a limited number of LES of swirling flows has been reported in the literature (Pierce & Moin, 1998a and 1998b; Kim et al., 1999). One example is the work by Pierce and Moin (1998a), which showed a rather promising agreement between the numerical and the experimental results for a low swirl number case.

6.2 Experimental set up of confined swirling flows in a dump combustor

To validate the numerical methods for simulating the swirling flows, the simulations of confined swirling flows have been compared to an experimental test case by Wessman (1995). Some results are published in Wang et al. (2004a).

The experimental setup is shown schematically in Figure 6.1. It consists of a swirl generator, a long guiding pipe, a sudden expansion, a test section, and a constriction pipe. The test section geometry can be viewed as a simplified gas turbine combustion chamber, where swirl is introduced to increase the mixing rate and to stabilize the flame. Hereafter, the sudden expansion step height, H, is chosen as a typical length scale.

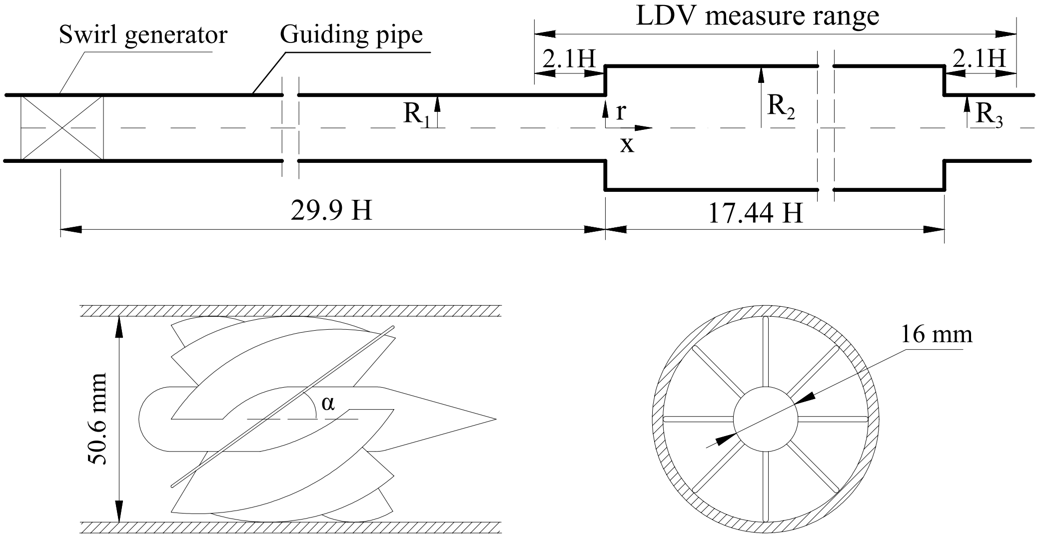

Figure 6.1 A schematic plot of the experimental rig. Top: from left to right, swirl generator, guiding pipe, sudden expansion, main test section, and constriction pipe outflow, where step height $H=R_2-R_3=R_2-R_1=23.8$ mm, $R_1=R_3=25.3$ mm, $R_2=49.1$ mm. Bottom: left, a side view of the swirl generator with the guide vane inclination angle α ; right, a cross section of the swirl generator.

This swirl generator consists of eight flat vanes with an inclination angle (α). Three different vane inclination angles are used, which are 26, 48 and 66 degrees, respectively, to generate different levels of swirl. The length of the guiding pipe is as long as 29.9H. It was shown that the pipe is long enough to give an adequate level of turbulence and more importantly a reasonable range of swirl numbers defined at the exit of the guiding pipe.

Two-component Laser Doppler Velocimetry (LDV) measurements were made in the test section. The measurements were made as radial profiles at different axial positions between $-2.1\mathrm{H} \le x \le 19.54\mathrm{H}$, where $x = 0$ is placed at the backward-facing step, as shown in Figure 6.1. Time averaged mean axial, radial and azimuthal velocity components, the variances and the Reynolds shear stresses along the radial direction at different axial positions were measured.

In this thesis work, the level of swirl is represented by the swirl number, defined as the ratio between the axial flux of the swirl momentum to the axial flux of the axial momentum multiplied by a reference tube radius (R_1), namely,

$$S = \int_0^R U U_\theta r^2 dr \Big/ R_1 \int_0^R U^2 r dr \tag{6.1}$$

Here, R is the local radius of the combustor at different axial positions. U and U_θ are the mean axial and azimuthal velocity components, respectively. The characteristic swirl number of an experimental case is evaluated at $x = -2.1\mathrm{H}$ position. Flows with different swirl numbers and Reynolds numbers were measured. In this work, three test cases with swirl number S=0.0, 0.33 and 0.43 respectively, are computed with LES; hereafter, these tests case are denoted as S0, S33 and S43, respectively.

Flow parameters for these three cases are given in Table 6.1. The Reynolds number is based on the inlet diameter and the inlet bulk velocity U_b. The u' is the root-mean-square turbulence velocity fluctuation; the integral length scale l is in the order of H; Re_l is the turbulent Reynolds number; λ is the Taylor micro-scale, estimated using $\lambda \sim l/\sqrt{Re_l}$. Taylor micro-scale represents the length scale in the inertial sub-range of the energy spectrum; it is desirable to resolve the Taylor micro-scale in LES.

Table 6.1 Experimental and Computational Cases. S: swirl number defined at $x = -2.1\mathrm{H}$; $S_{\max}$: maximum swirl number (at about x/H=2)

Cases	S	$S_{\max}$	Re	U_b (m/s)	u' (m/s)	l (mm)	Re_l	λ (mm)
S0	0	0	11700	1.59	0.1–0.3	10	150–450	0.5–0.8
S33	0.33	0.8	10000	1.57	0.1–0.5	10	150–750	0.4–0.8
S43	0.43	1	20000	2.72	0.1–1.0	10	150–1500	0.3–0.8

The computational domain is $-2.1\mathrm{H} \le x \le 17.44\mathrm{H}$, and the sudden constriction at x=17.44H is included in the computational domain. In the present LES, the grid resolution is about 2 mm in axial direction and 0.76 mm in other two directions (shown in Table 6.2); the CFL number is chosen to be 0.2, which gives a time step about 10^{-4} s. A total of 20 000 to 30 000 time steps is used to compute the time averaged mean flow field, which is equivalent to a time interval of 2–3s, about 20–150 integral time scale (the integral time scale is about 0.02s–0.1s).

6.3 Boundary conditions and grid resolution

6.3.1 Outlet condition

Two outflow boundary conditions have been tested: the ‘zero-gradient’ outflow condition and the ‘convective’ outflow condition (see Section 5.3.3). These two conditions are first compared in simulations of swirling flows in straight pipe. The diameter of the pipe is D=0.1224m; the inlet bulk velocity is 6.558m/s; and *Re* is 21 000. The inlet swirling flow is of solid body rotation type. Figure 6.2 shows the LES results, the distributions of the swirl number and the mean axial velocity along the axis of the pipe, for the studied eight cases (with two swirl numbers, two pipe lengths, two outflow conditions, respectively).

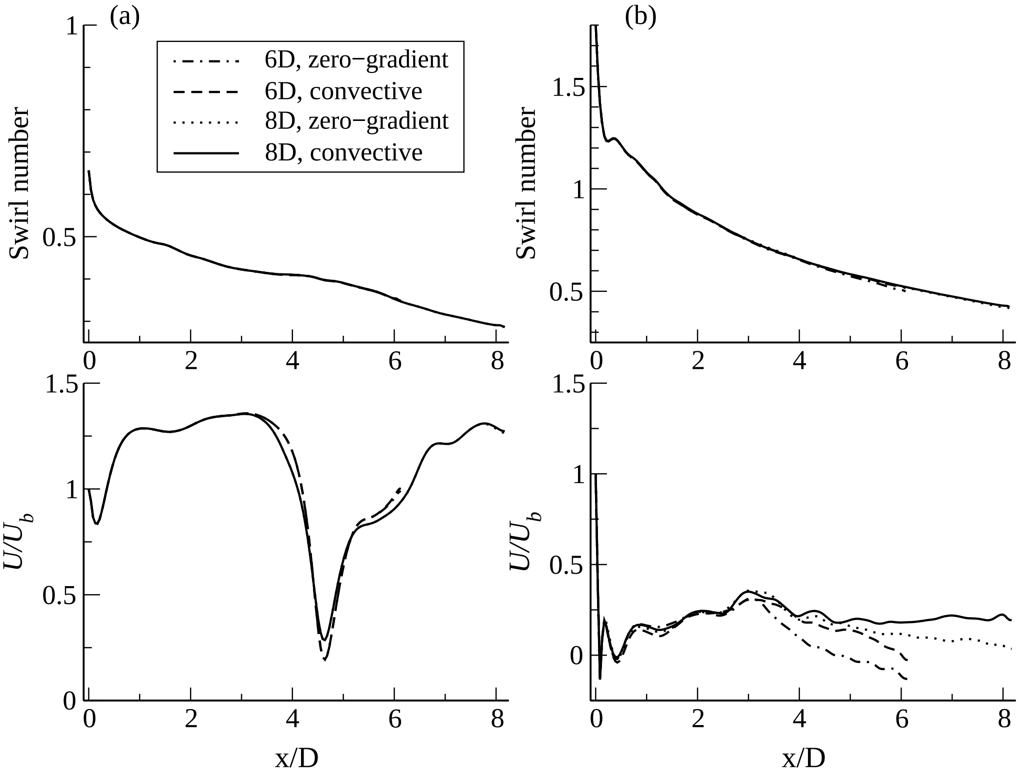

Figure 6.2 Distribution of the swirl number and the mean axial velocity along the axis of straight pipe. Pipe diameter D=0.1224 m, inflow velocity U_b=6.558 m/s. (a) S=0.65; (b) S=1.8.

It is shown that the length of the pipe has little influence on the upstream flow structure. In the low swirl number case (S=0.65, Figure 6.2(a)) the mean axial velocity is slightly affected in the downstream region, about 3D from the outlet. In the high swirl number case (S=1.8, Figure 6.2(b)) the influence of the pipe length is also limited to the downstream region about 3D from the outlet, although the difference in the axial velocity profile is larger than the low swirl case. Figure 6.2 shows also an important feature of swirling pipe flows, the decay of swirl number along the axial direction. The decay rate of the swirl number is not affected at all by the length of the pipe. For the low swirl number case, the two outlet conditions predict an identical decay rate of swirl number and an identical mean axial velocity. But for higher swirl number case, the calculated mean axial velocity profiles using two different outflow boundary conditions differ fairly significantly. The difference is larger in the downstream near the outlet. Certain effect of the outflow condition is still evident at 1D from the inlet.

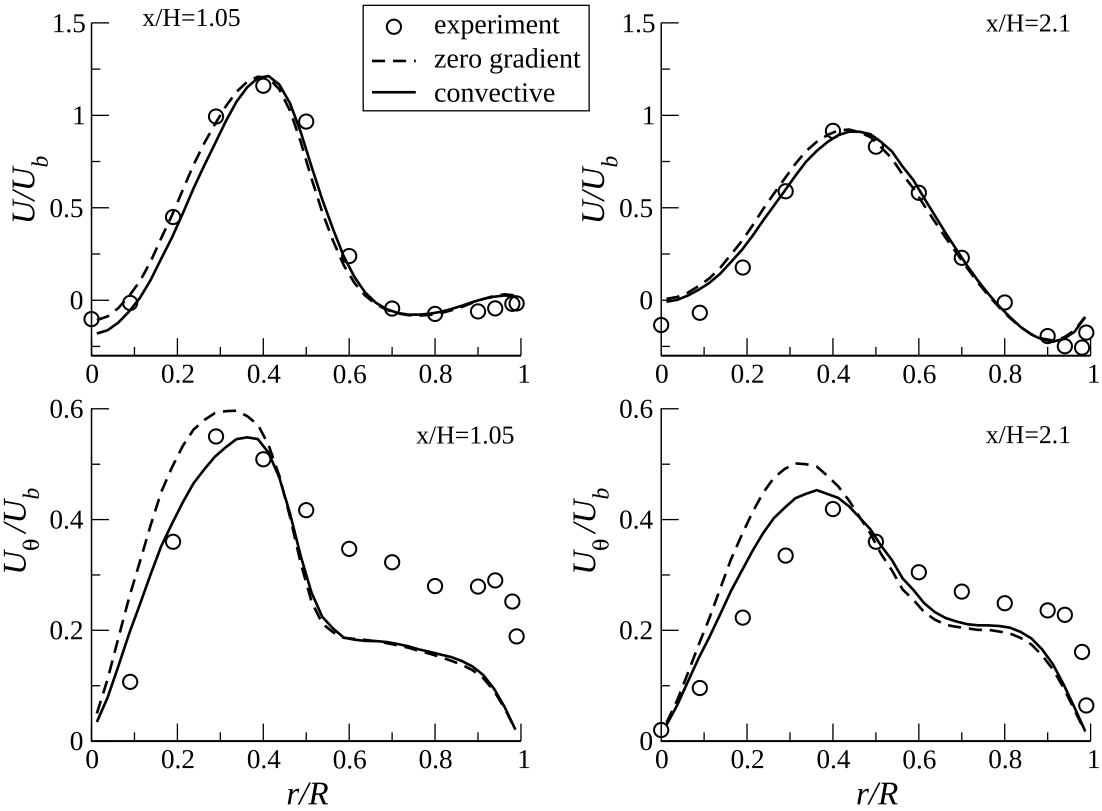

Figure 6.3 Radial profiles of time averaged axial and azimuthal velocity components at two axial positions of case S43, from the experiment and LES using two different outflow boundary conditions.

Then, these two outflow conditions are compared in the simulations of case S43, shown in Figure 6.3. The two outflow conditions predicted a nearly identical axial velocity at the two axial positions. However, the azimuthal velocity profiles calculated using different outflow boundary conditions are fairly different. The ‘convective’ outflow condition predicts a lower peak value of the azimuthal velocity, and gives a result that is a little closer to the experimental data. Thereafter, the ‘convective’ outflow condition is used in the following computations (unless otherwise explicitly stated).

6.3.2 Inlet condition

Correct representation of inflow turbulence is an important issue for LES. In this work, three different inflow conditions (see Section 5.3.2) have been investigated: 1) a non-fluctuation, i.e 'laminar inflow' condition; 2) a random-fluctuation condition; 3) a rescaled inflow library condition. In the random-fluctuation condition, a random fluctuation to the measured mean velocity profiles is superimposed. The amplitude of the random fluctuation of each velocity component is rescaled to match the measured variance of the velocity fluctuations. This condition is simple to implement, however, it does not give a correct physical representation of the turbulence energy spectrum of the inflow.

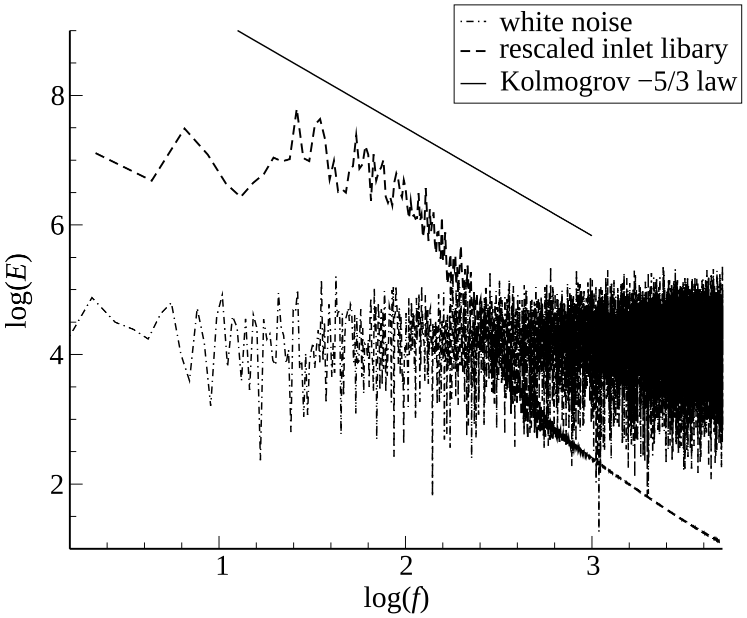

Figure 6.4 Eulerian energy time spectra of the random-fluctuation inflow and the rescaled turbulent inflow library.

The energy time spectra of the random-fluctuation and the rescaled inflow library conditions are plotted in Figure 6.4. The random-fluctuation produces an almost constant distribution of turbulent kinetic energy over all the time (and length) scales. This is in contradicting with the well-known turbulent flow theory, i.e. the turbulent energy cascade that describes the energy transfer between large scales and small scales. Since the rescaled inflow library condition is originated from the turbulent flow calculation, it has a more reasonable turbulent kinetic energy spectrum: most energy is contained in the large length scales (low frequency, f), and the turbulent kinetic energy becomes lower when the length scale decreases from the integral length scale. The Kolmogorov $-5/3$ power law in the inertial subrange is shown by a straight line.

These three inflow conditions, then, are used to compute the swirling flow case S43, respectively. Figure 6.5 shows the mean axial and azimuthal velocity profiles at two axial stations, *x*/H=1.05 and 2.1. The laminar inflow condition and the random fluctuation condition predicted approximately the same maximum axial velocity and the peak position as the experimental data at x/H=1.05. The rescaled turbulent inflow library condition gave a little different axial velocity. At *x*/H=2.1, the peak of the axial velocity is shifted towards the outer wall, which leads to a slightly different shape of IRZ. More significant difference between results from the three inflow conditions are seen in the azimuthal velocity profiles; the rescaled turbulent inflow condition shows a much better agreement in the azimuthal velocity distribution. The 'laminar inflow' condition and the random-fluctuation inflow condition yield similar results that differ from the results obtained using the rescaled turbulent inflow library condition. This shows that adding random fluctuations to the mean velocity profile is almost equivalent to not adding any fluctuations to the profile, which suggests that the random-fluctuation inflow condition is not adequate for LES of turbulent flows.

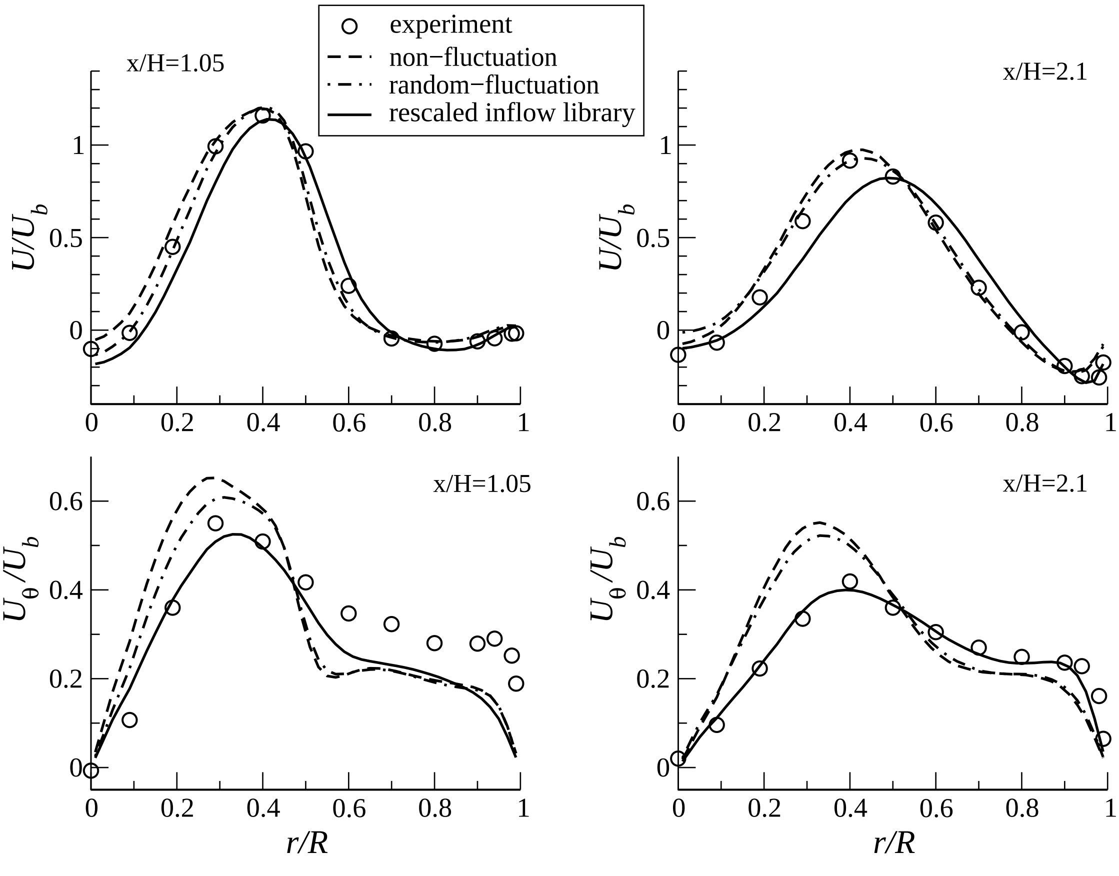

Figure 6.5 Radial profiles of the time averaged axial and azimuthal velocity at two axial positions of test case S43, from the experiment and LES using three different inflow boundary conditions.

The influence of these inflow conditions can also be seen in the distribution of the mean turbulence kinetic energy along the axis of the combustor, as given in Figure 6.6. The 'laminar inflow' condition has a zero turbulent kinetic energy at the inlet port. With this inflow condition the turbulent kinetic energy increases continually from zero value to a peak at about *x*/H=1.5, which is downstream of the measured location of the peak turbulent kinetic energy. Further downstream, turbulent kinetic energy decays very quickly. When approaching to the exit, turbulent kinetic energy increases again, as a result of the acceleration of the axial velocity and the existence of the shear flow caused by the contraction of the combustor geometry.

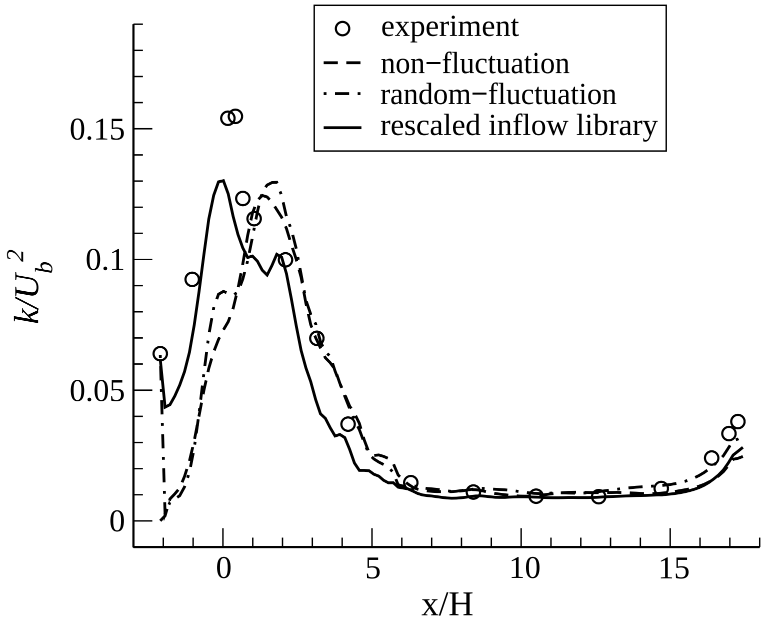

Figure 6.6 Turbulent kinetic energy distribution along the axis of the dump combustor of test case S43, from the experiment and LES using three different inflow boundary conditions.

Both the rescaled turbulent inflow library condition and the random-fluctuation condition introduce fluctuations in the inflow, with finite turbulent kinetic energy at the inlet. However, the random-fluctuations are damped out quickly. The turbulent kinetic energy falls to the same level as that obtained using the 'laminar inflow' condition within a very short distance. It is seen in Figure 6.6 that the two inflow conditions, the 'laminar inflow' condition and the random-fluctuation condition give very similar axial distribution of the turbulent kinetic energy, which is consistent with the fact that the two conditions predicted almost identical mean velocity in the flow field. The 'rescaled inflow library' condition also shows a decrease of turbulent kinetic energy in the guiding pipe near the inlet (*x*<0). This is likely due to a mismatch between the 'rescaled inflow turbulence' and the real physical flow and relative coarse grid resolution of wall boundary layers in the guiding pipe. Nevertheless, the decrease rate from the 'rescaled flow library' condition is smaller than that from the other two conditions. Further downstream, turbulent kinetic energy starts to increase, due to the shear layer downstream of the backward-facing step. At the shoulder of the backward-facing step wall ($x = 0$) turbulent kinetic energy at the combustor axis reaches its peak value. The sudden decrease of turbulent kinetic energy with the rescaled inflow library condition in $0<x/\mathrm{H}<2$ may be due to the lack of correct shear stresses components, $\overline{u'v'}$, $\overline{u'w'}$, $\overline{v'w'}$, in the inlet.

Another interesting observation can be made from Figure 6.6. The peaks of the turbulent kinetic energy calculated with the three inflow conditions do not differ significantly. The decay rates of the turbulent kinetic energy at downstream are also very similar. One may conclude that in turbulent swirling flows, since the production of turbulence is mainly in the shear layers in the IRZ, the inflow turbulence has only a limited effect on the overall turbulence structure in the flow field.

6.3.3 Grid resolution

Three grid resolutions are tested, as shown in Table 6.2. The computation domain is between $-2.1\mathrm{H} \le x \le 17.44\mathrm{H}$, which includes the contraction at the outlet. In order to improve the grid resolution and to keep the total grid points under an acceptable level, local refinements in all three coordinate directions are performed in Grid 2 and Grid 3 (see Table 6.2). When using Grid 3, Message Passing Interface (MPI) technique is used to parallelize the computation. The radial resolution of Grid 2 and Grid 3 is in the order of (or close to) the estimated Taylor micro-scale. The axial resolution is a little coarser due to computer limitations.

Table 6.2 Three grid resolutions have been tested

Grid	Grid points (million)	Grid sizes (mm) ($x \times y \times z$)	Local refinement
Grid 1	2.1	2.193×1.196×1.196	No refinement
Grid 2	2.9	1.973×0.764×0.764	$x \le 6\mathrm{H}$
Grid 3	6.4	1.292×0.764×0.764	$x \le 10\mathrm{H}$ (with MPI)

It is shown in Figure 6.7 that Grid 2 and 3 yield a better azimuthal velocity profile than Grid 1, due to the better resolution in the radial direction. The difference between the numerical results from Grid 2 and Grid 3 is, however, not substantially large although the fine grid (Grid 3) yields better agreement with the experimental data. Comparison of other mean velocity components and the velocity variance profiles gives a similar conclusion. Considering the computational effort, Grid 2 is preferred. Thereafter, Grid 2 is used in the following simulations, unless otherwise explicitly stated.

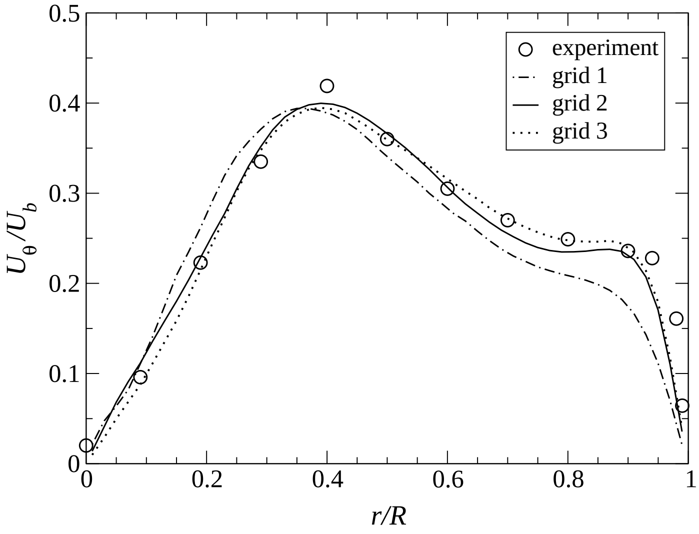

Figure 6.7 Time averaged azimuthal velocity profiles by different grid resolutions, *x*/H=2.1, case S43.

6.4 Flow structures of swirling flows

6.4.1 Flow structures of the non-swirl case

Figure 6.8 shows instantaneous streamlines of the non-swirl case at three cross sections (obtained from LES), one along the combustor axis and two across the axis. The instantaneous streamlines show a three-zone flow/turbulence structure: a core zone near the axis, a near-wall zone and in between a shear layer. In the near axis core region the streamlines follow fairly smoothly the combustor axis; the streamlines are nearly straight. Near the outer wall a long recirculation zone is found behind the sudden expansion, and in between there is a typical shear layer where different eddies are generated as a result of shear layer instability of Kelvin–Helmholtz type. Streamlines at the two cross sections show various eddies that roll up the fluid, which enhances the mixing process.

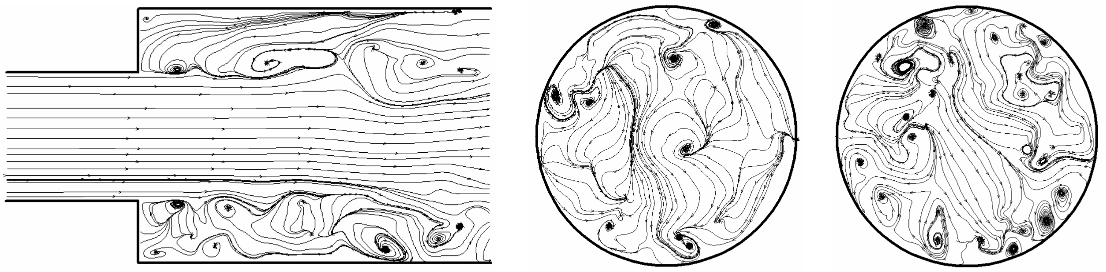

Figure 6.8 Instantaneous streamlines of the non-swirl case, at three sections obtained from LES: left, along the combustor axis; middle, across the combustor axis at *x*/H=1, and right, across the combustor axis at *x*/H=5.

Figure 6.9 shows the time averaged mean velocity profile, normalized by the bulk velocity at the inlet, along the radial direction at different axial positions. To give a clear picture of the global structure of the mean flow field we plot the mean profiles in the *x*–*r* plane (cylindrical coordinate system), in which the *x*-axis also gives the value of the shown quantities. The dashed lines denote the measurement positions and they are also the zero value level of the shown quantities. The scaling of the shown quantities is given in figures by the short lines in the upper left corner of the figures and the numbers above the short lines. Shown in Figure 6.9 are strong mean axial flows and negligibly small

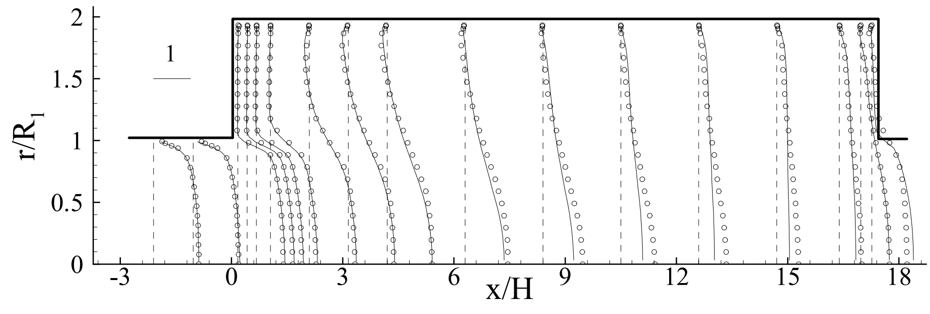

(a) U/U_b

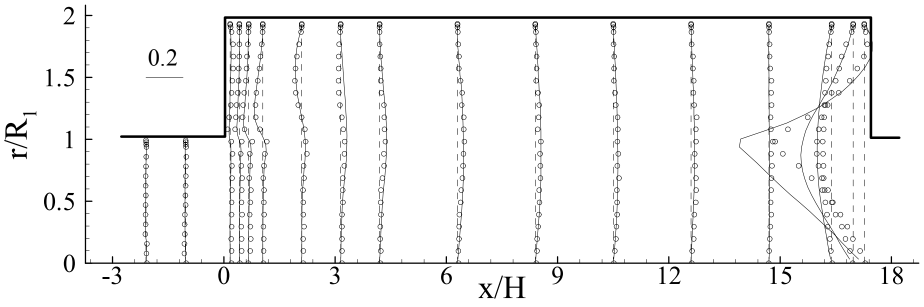

(b) U_r/U_b

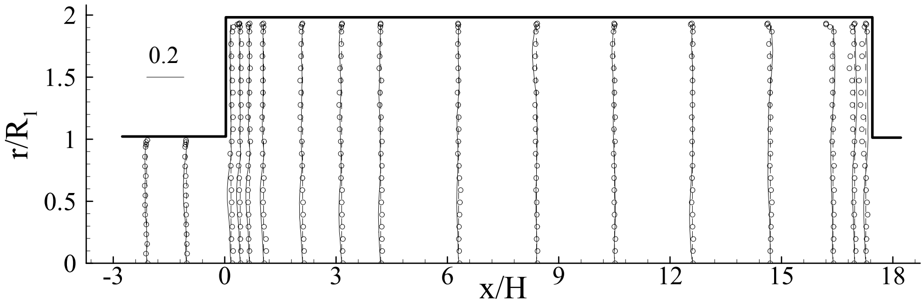

(c) U_θ/U_b

Figure 6.9 Time averaged mean velocity components of the non-swirl case. Solid lines, LES results; circles, measurement data; dashed lines represents both the zero level of the shown quantities and the measurement position; the scaling of the shown quantity is given by the numbers and the short line in the upper left corner of each figure. Note that the scaling of the radial and azimuthal velocity components is 5 times the scaling of the axial velocity component.

mean radial- and azimuthal- flows. The axial momentum spreads in the radial direction after the sudden expansion, and in the near axis core zone the axial velocity decays slowly; the numerically calculated mean axial velocity decays faster, which may be due to the lack of grid resolution at $x/\mathrm{H} > 6$ in Grid 2; in the near-wall zone near the sudden expansion a reversing flow exists. The numerical results agree rather well with the measured data. Near the outlet, due to the constriction of the combustor, a mean radial velocity is observed both in the experiments and LES. The influence of the constriction outflow is rather local (noticeable only in the downstream region $x/\mathrm{H} > 16$).

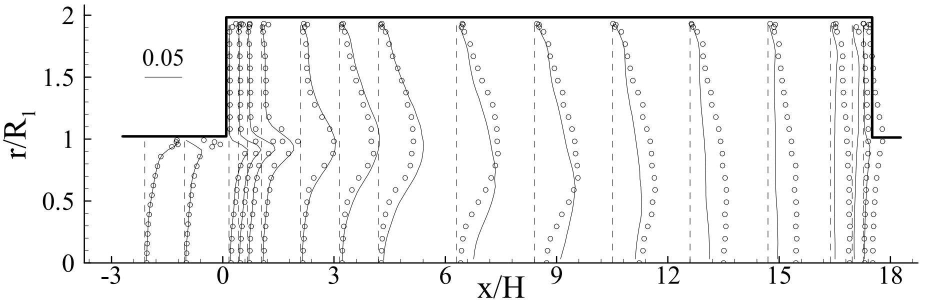

(a) $\overline{u'u'}/U_b^2$

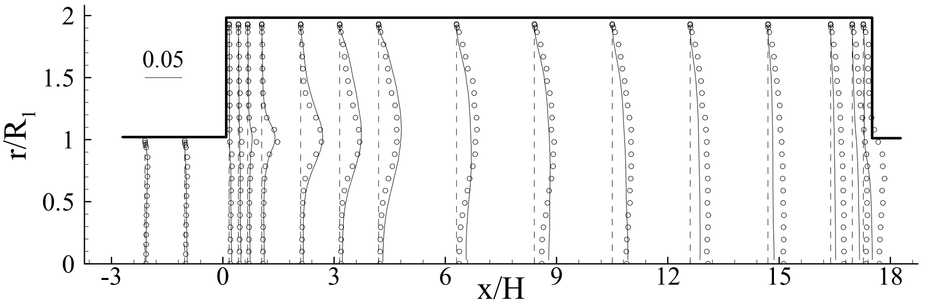

(b) $\overline{u_r'u_r'}/U_b^2$

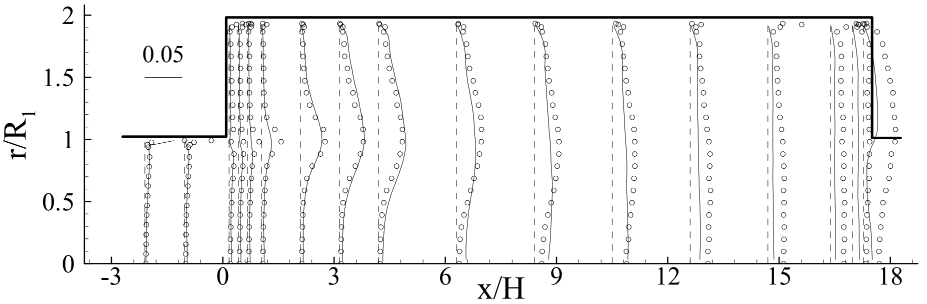

(c) $\overline{u_\theta'u_\theta'}/U_b^2$

Figure 6.10 Variances of velocity components of the non-swirl case. See Figure 6.9 for further caption.

Next, we examine the time averaged turbulent intensities and velocity correlations. Winckelmans et al. (2002) pointed out that the time averaged LES turbulent intensities and the velocity correlations may not be comparable to the time averaged counterparts of the experimental data or DNS data when the SGS models are based on a traceless formulation (for example the Smagorinsky model). The traceless type SGS models are useful for LES of incompressible (or low Mach number) flows since in simulation of these flows only the traceless (or deviatoric) part of the SGS stresses needs to be modeled, while the trace of the SGS stresses is lumped into a modified pressure. As a result, the reduced (deviatoric) turbulent intensities from both LES and DNS or experiments should be compared. The trace term is more pronounced if the filter and grid sizes are large, i.e. when very large eddy simulation (VLES) is performed. In the SSM used in the present work, the trace term is retained in the SGS stress. Therefore, we will examine the conventional turbulent intensity and velocity correlations in the following. These quantities have an apparent physical meaning and thereby more useful to delineate the turbulence structures at different swirl conditions.

Figure 6.10 shows the normalized variances of the three velocity components. Figure 6.11 shows the normalized Reynolds shear stresses, $\overline{u'u_r'}/U_b^2$ and $\overline{u'u_\theta'}/U_b^2$. As seen from Figure 6.10 and Figure 6.11, turbulence is mostly generated in the shear layer near the sudden expansion. From Figure 6.10(a), it is shown that although the near-wall turbulence intensity in the guiding pipe before the sudden expansion is under-predicted with the current grid resolution (Grid 2), the influence of the near-wall turbulence in the guiding pipe on the downstream flow is not substantial. This implies that the generation of turbulence in the shear layer after the sudden expansion is the dominant mechanism for the turbulence production in the present non-swirl case.

It is interesting to note that although the mean radial and the azimuthal velocity components are negligible in the entire flow field, the variances of the radial and the azimuthal velocity are significant. From Figure 6.10, a three-zone turbulence structure can be identified: a highly anisotropic turbulence production zone nears the sudden expansion, a decaying turbulence zone at far downstream, and in between a ‘return-to-isotropic-turbulence’ zone. In the first zone near the sudden expansion (the 3rd to 5th measured axial positions shown in Figure 6.9, $0<x/\mathrm{H}<0.8$), the flow shear stress ($\partial U/\partial r$) is the highest. The variance of the axial velocity is high; however, the variances of the radial and the azimuthal velocity components are negligible. In this zone turbulence is highly anisotropic. LES properly predicted the production of the variances (and the turbulent kinetic energy) in this zone. In the second zone slightly downstream (the 6th to 12th axial positions shown in Figure 6.10, $1<x/\mathrm{H}<10$) the variances/turbulent kinetic energy are further generated in the shear layer, and moreover, the variances of the radial and the azimuthal velocity components are significantly increased. This is because of the three dimensional vortex dynamics of turbulence eddies, which redistributes turbulent energetic fluctuations to all directions. Turbulence becomes more isotropic in this zone. In the far downstream zone, turbulence decays slowly. The two Reynolds shear stresses, $\overline{u'u_r'}/U_b^2$ and $\overline{u'u_\theta'}/U_b^2$, are generally low, as compared to the variances. Similar to the variances, the peak shear stress ($\overline{u'u_r'}/U_b^2$) is in the shear layer behind the sudden expansion where the major production of turbulence occurs. The shear stress decreases along the axial direction downstream. The outlet constriction has a very limited influence on the shear stresses. The LES results and the measurement data are in reasonably good agreement.

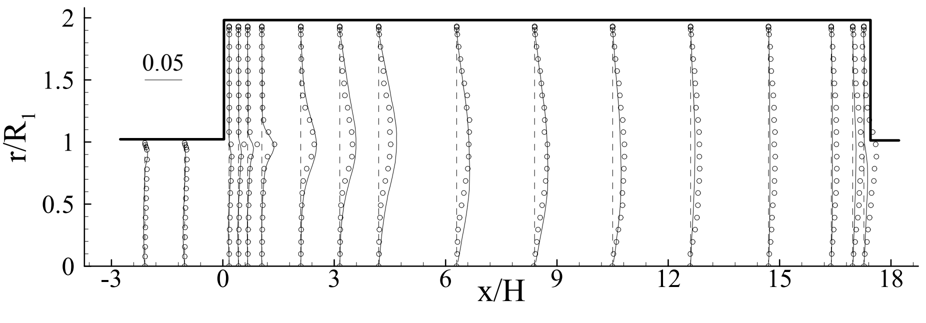

(a) $\overline{u'u_r'}/U_b^2$

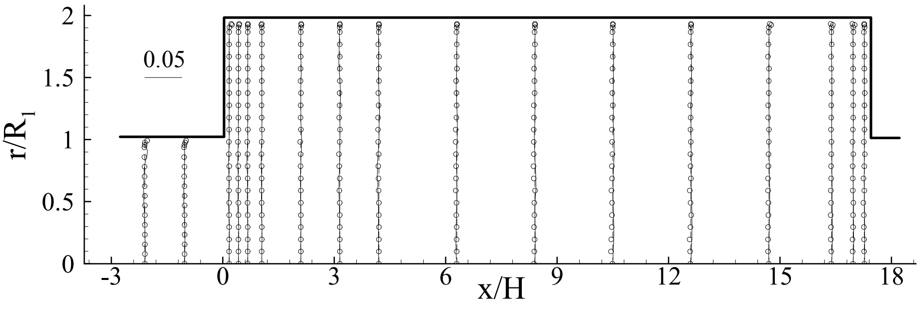

(b) $\overline{u'u_\theta'}/U_b^2$

Figure 6.11 Reynolds shear stresses of the non-swirl case. See Figure 6.9 for further caption.

6.4.2 Flow structures of the moderate swirl case

Instantaneous streamlines from LES for the moderate swirling flow case are shown in Figure 6.12. In the guiding pipe the streamlines are no longer straight lines. At a distance about *x/*H=3 downstream of the sudden expansion, the streamlines in the near axis core region show flow reversals, i.e., internal recirculation zones are generated as a result of the vortex breakdown. The internal recirculation zone, IRZ, is of bubble type whose shape is not axisymmetric. The shape and position of IRZ change with time. Streamlines at the first cross section show the large scale swirling flow motion that decays at further downstream (shown at the cross section *x*/H=5). The streamlines in these cross sections are un-smooth and wrinkled, which indicates the existence of different smaller eddies. The center of the large swirling flow, marked in the figure with a '+' sign, is generally off the combustor axis, which leads to a non-zero radial and azimuthal velocity component at the axis.

Time averaged mean velocity profile for the moderate swirling flow (S33) is shown in Figure 6.13. As compared with Figure 6.9, the difference between the swirling flow and non-swirling flow is primarily in the near axis core zone. In the swirling flow, the axial velocity component near the combustor axis is significantly lower than the counterpart of the non-swirl case. Around *x/*H=3, the mean axial velocity is about zero. LES correctly reproduced the measured axial velocity profile and the vortex breakdown as shown in the instantaneous streamlines. Significant difference between the swirling and non-swirling cases is also found in the azimuthal and the radial velocity components. The highest azimuthal velocity component is found in between the core

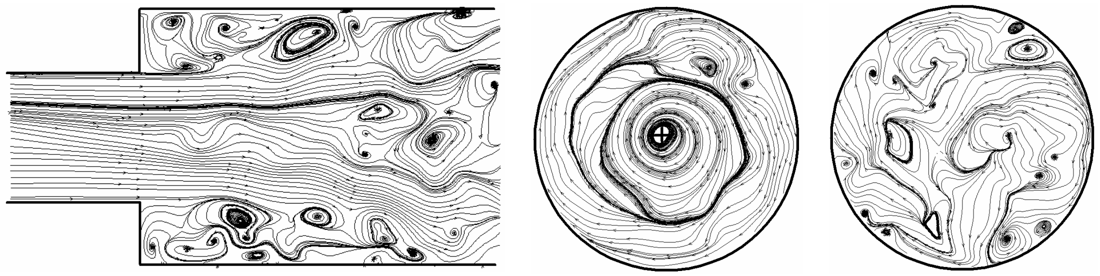

Figure 6.12 Instantaneous streamlines of the moderate swirl case, S33, at three sections obtained from LES: left, along the combustor axis; middle, across the combustor axis at *x*/H=1 and right, across the combustor axis at *x*/H=5.

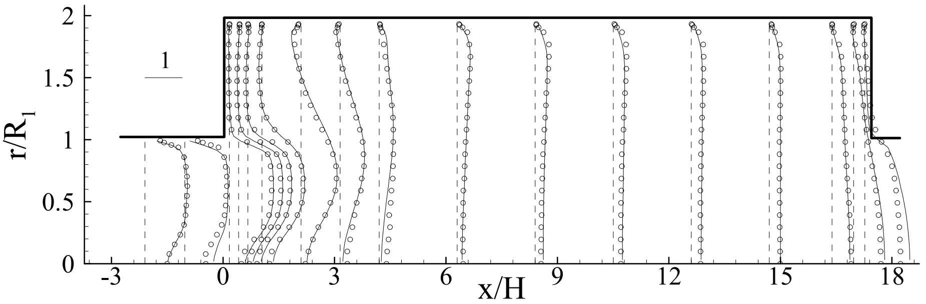

(a) U/U_b

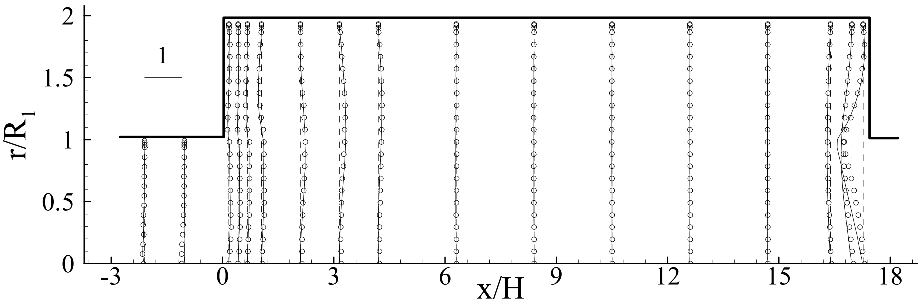

(b) U_r/U_b

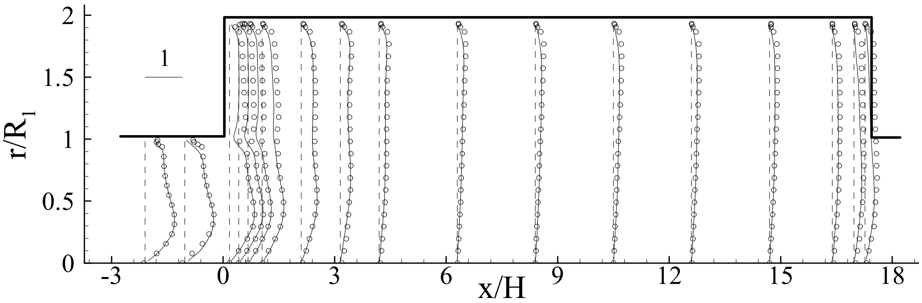

(c) U_θ/U_b

Figure 6.13 Time averaged mean velocity components of the moderate swirl case, S33. See Figure 6.9 for further caption.

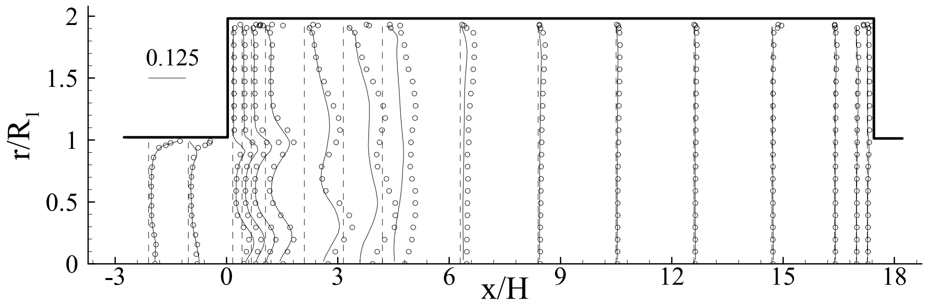

(a) $\overline{u'u'}/U_b^2$

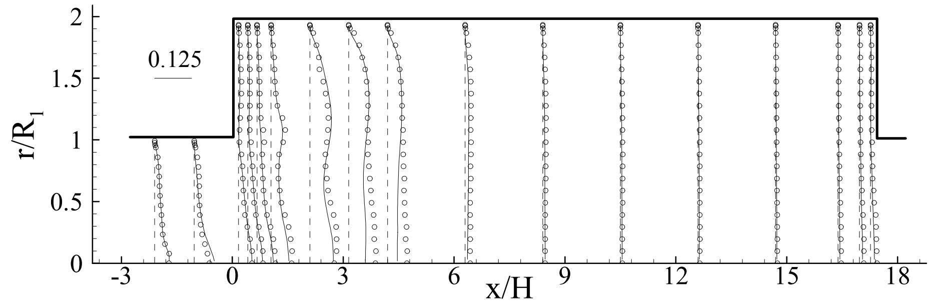

(b) $\overline{u_r'u_r'}/U_b^2$

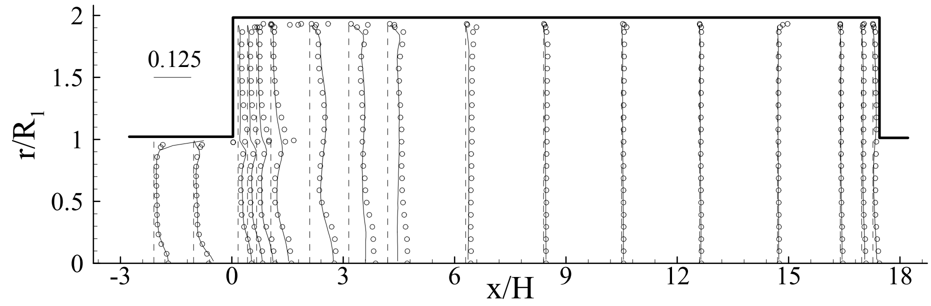

(c) $\overline{u_\theta'u_\theta'}/U_b^2$

Figure 6.14 Variances of different velocity components of the moderate swirl case, S33. See Figure 6.9 for further caption.

zone and the shear layer. In the shear layer large azimuthal velocity gradient exists. The constriction outflow has a rather local influence on the flow field, similar to the non-swirl case. LES predicted the azimuthal and radial velocity distribution fairly well, as compared with the experiments.

The variances of the three velocity components are shown in Figure 6.14. The three variances differ considerably, indicating high turbulence anisotropy. From the variance of the axial velocity component we note that turbulence is produced not only in the shear layer associated to the sudden expansion ($r/R_1 \sim 1$) but also near the axis of the combustor (here a strong velocity gradient exists). Compared to the non-swirl case, the variances of the radial and the azimuthal velocity components near the sudden expansion are higher. Another significant difference between the swirling and the non-swirling cases is in the decay rate of turbulence. In the swirling flow case, the decay of turbulence is faster.

The Reynolds shear stresses are plotted in Figure 6.15. Similar to the variances, there are two peaks in the shear stress profile along the radial direction. One is in the shear layer behind the sudden expansion and the other is near the axis vortex breakdown region. Production of turbulence occurs mainly in these two zones. The shear stress decreases rather quickly along the axial direction downstream. The outlet constriction has almost no influence on the shear stresses. LES predicted the distributions of the variances of the three velocity components, the fast decay rate and Reynolds stresses fairly well.

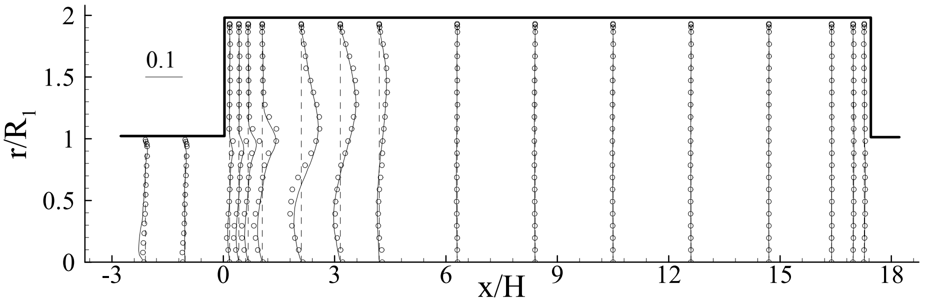

(a) $\overline{u'u_r'}/U_b^2$

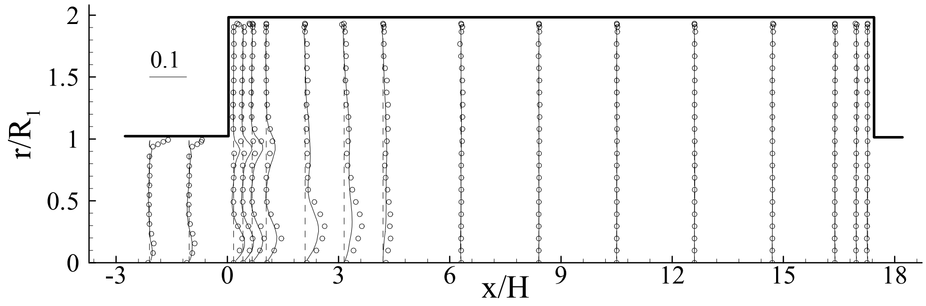

(b) $\overline{u'u_\theta'}/U_b^2$

Figure 6.15 Reynolds shear stresses of the moderate swirl case, S33. See Figure 6.9 for further caption.

In the guiding pipe (x/H<0) high level near-wall turbulence is observed in the experiments (see Figure 6.14 and Figure 6.15). The LES predicted near-wall turbulence is somewhat lower than the experimental data. This is believed to be mainly due to the lack of grid resolution in the wall normal direction. The contribution from the SGS terms to the turbulent intensities is not dominant (about 10%–20% at most). Similar trend has been observed for cases S0 and S43 (shown later). With finer near-wall grid resolution (e.g., 2–5 times finer in the radial direction), we expect that the current LES method to yield a better prediction of the near-wall velocity variances. However, this would require 8–20 times more grid points. In view of the limitation of computer capacity a full resolution of near-wall turbulence is difficult in the near future. Piomelli (1999) pointed out that approximate wall boundary conditions, or wall models, may be used; this, however, introduces further empiricism in LES. Similar to the non-swirl case, although the near-wall turbulence intensities are under-predicted with Grid 2, the turbulence intensities after the sudden expansion and in the vortex breakdown zone are reasonably well predicted, since the dominant source of turbulence production is in the vortex breakdown zone and the shear layer after the sudden expansion.

6.4.3 Flow structures of the strong swirl case

In the strong swirling flow case (S43) the instantaneous streamlines shown in Figure 6.16 indicates the occurrence of vortex breakdown already at *x/*H=1. The internal recirculation zone is found between *x/*H=1 and 4, much earlier and larger than the moderate swirl case (S33). The tendency that vortex breakdown occurs more upstream as the swirl number increases confirms the previous finding reported in the recent review by Lucca and O'Doherty (2001). In the internal recirculation zone different eddies are found and the shape of the internal recirculation zone is also bubble-like and highly irregular. The streamlines at the two cross sections show similar structure of the flow, a strong large scale swirling flow together with various eddies. The center of the large scale swirling flow is off the axis; at the axis, the radial and the azimuthal velocity components are typically non-zero.

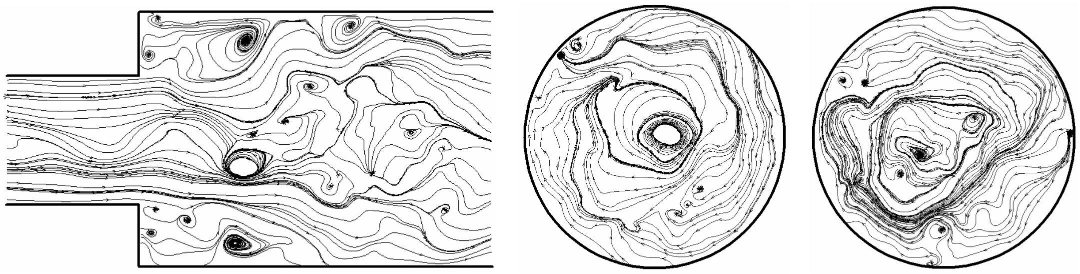

Figure 6.16 Instantaneous streamlines of the high swirl case, S43, at three sections obtained from LES: left, along the combustor axis; middle, across the combustor axis at *x*/H=1 and right, across the combustor axis at *x*/H=5.

The time averaged mean flowfield of strong swirl case has several important similarities and differences as compared with the moderate swirl case (see Figure 6.13 and Figure 6.17). In the region near the sudden expansion, the axial, radial and azimuthal mean velocity profiles show a similar flow structure: a near axis core zone, a corner recirculation zone near the combustor walls, and in between a shear layer. A major difference from the case of the moderate swirl is in the near axis core zone — with stronger swirl the IRZ size is larger and further upstream, as already seen in the instantaneous lines.

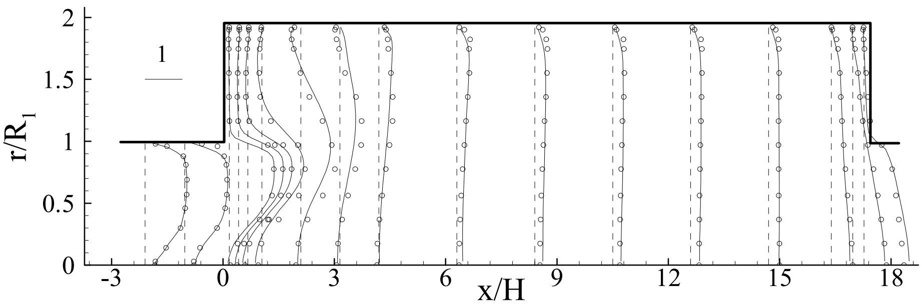

(a) U/U_b

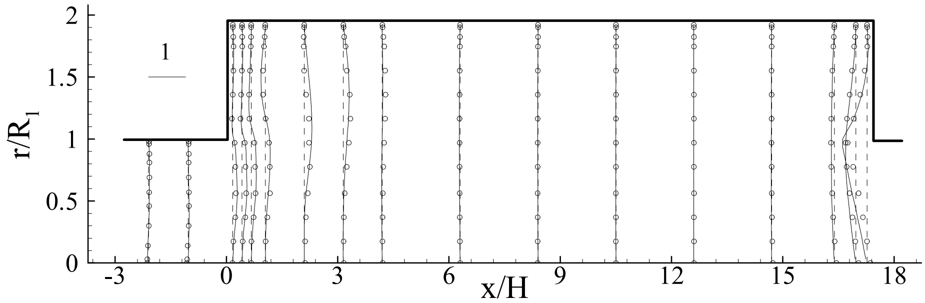

(b) U_r/U_b

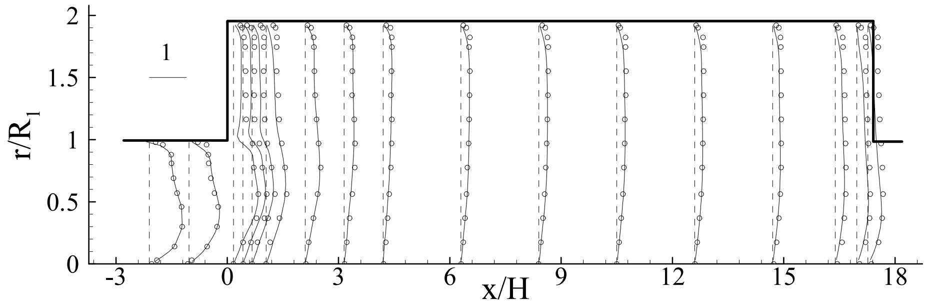

(c) U_θ/U_b

Figure 6.17 Time averaged mean velocity components of the high swirl case, S43. See Figure 6.9 for further caption.

Figure 6.18 and Figure 6.19 show the variances and the two Reynolds shear stresses. The turbulence structure is generally similar to the moderate swirl case. The production of turbulence is mostly in the second shear layer caused by the strong IRZ, in the region $1 \leq x/\mathrm{H} \leq 4$, where IRZ is located, turbulence eddies are highly energetic and anisotropic. Slightly downstream to this region, at x/H=6, both the LES results and the measurement data show that turbulence already decayed to a low level. Compared to the non-swirl case, the intermediate zone in which 'turbulence returns to more isotropic' is narrow and insignificant. The LES results and the measurement data of this rather strong swirl case are in fairly good agreement in the mean velocity, the variances and Reynolds shear stresses, in particular in the highly anisotropic zone behind the sudden expansion.

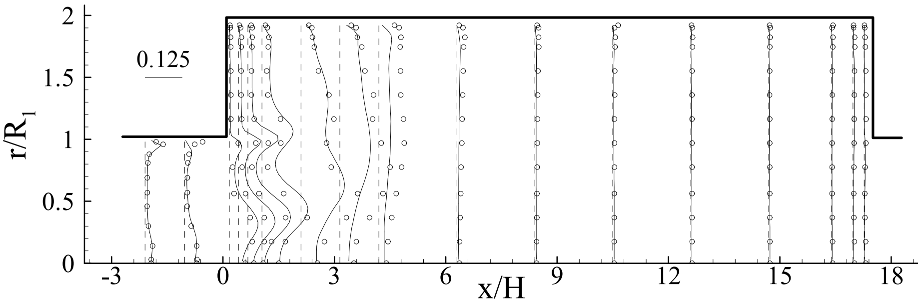

(a) $\overline{u'u'}/U_b^2$

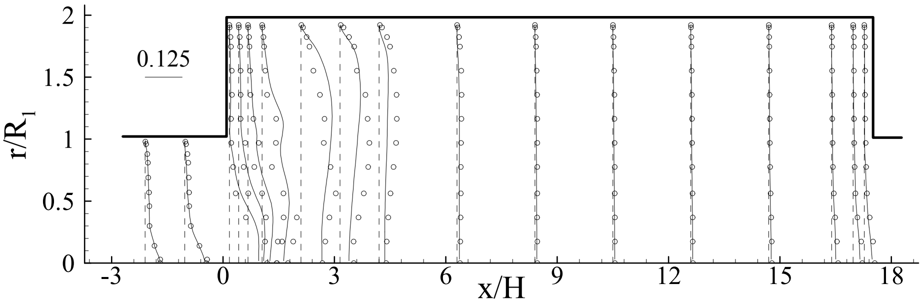

(b) $\overline{u_r'u_r'}/U_b^2$

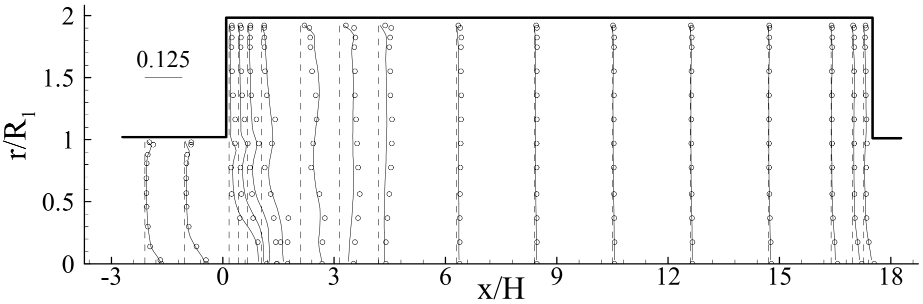

(c) $\overline{u_\theta'u_\theta'}/U_b^2$

Figure 6.18 Variances of different velocity components of the high swirl case, S43. See Figure 6.9 for further caption.

From the turbulence structure discussed above, it is clear that in LES of confined swirling flows, universally fine grid resolution has to be used along the radial direction to resolve not only the shear layers near the wall, near the edge of the sudden expansion, but also near the combustor axis where vortex breakdown occurs. This is quite different from the channel flow calculations where highly stretched grid can be used to resolve the wall boundary layer only.

6.4.4 Fast decay of turbulence in confined swirling flow

The fast decay of turbulence in confined swirling flows was also noticed in previous experiments (Kitoh, 1991; Nejad et al., 1989; Ahmed, 1998; Xia et al., 1998). The decay of turbulence in swirling free-jet flows (Ribeiro & Whitelaw, 1980; Huang & Tsai, 2001; Champagne & Kromat, 2000), on the other hand, is less pronounced as compared to the confined flows. Champagne and Kromat (2000) showed in a measurement of swirling coaxial jets that the axial and the azimuthal velocity variances increase monotonically throughout the whole measurement domain, up to *x/D*=10. This implies that the fast decay of turbulence in confined swirling flow is due to the combination effect of swirling motion and the wall friction.

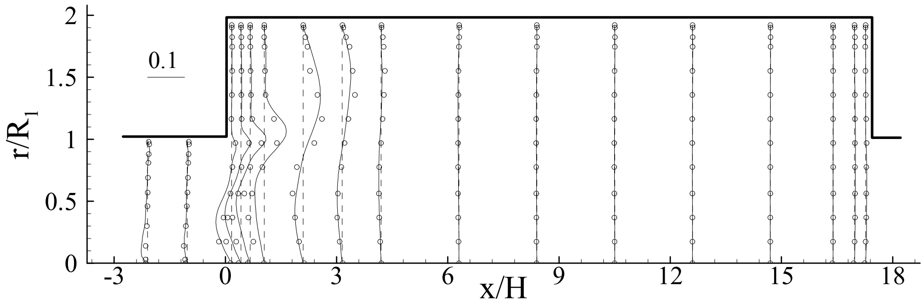

(a) $\overline{u'u_r'}/U_b^2$

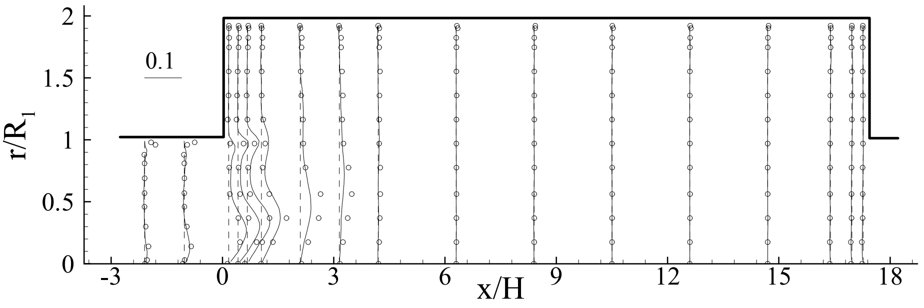

(b) $\overline{u'u_\theta'}/U_b^2$

Figure 6.19 Reynolds shear stresses of the high swirl case, S43. See Figure 6.9 for further caption.

By comparing the non-swirl confined case, the swirl confined case and the swirl free-jet case we may postulate a mechanism for the fast decay of turbulence in confined swirling flows. First, the swirling motion (the azimuthal flow) generates a centrifugal force that drives the flow to move outwards in the radial direction; the stronger outward radial flow transports the turbulent kinetic energy in the radial direction towards the wall faster; finally, turbulence near the wall is dissipated quickly by the wall viscous friction. The production of turbulence near the walls is not significant since the velocity and the velocity gradient near the wall are low.

In the free-jet flow there is no wall viscous dissipation, and in the non-swirl confined flow there is a lack of transport of turbulence in the radial direction towards the wall, which explains the slow decay rate of turbulence in both cases.

Due to the fast decay of turbulence, the three-zone turbulence structure found along the axial direction in the confined non-swirling flow is significantly altered. The highly anisotropic turbulence produced in the upstream shear layers near the sudden expansion and the IRZ decays so quickly that the ‘return-to-isotropic turbulence’ zone almost disappears. In combustion systems, this implies fairly different modes of combustion, mixing and heat transfer in different places of the combustor.

6.5 Precessing vortex core phenomenon

In swirling flow experiments (Wessman, 1995), it is found that the center of the IRZ is not often at the center of the circular pipe, but rotates about the axis of symmetry at a low frequency. This unsteady and periodic motion of large-scale well-organized structure is usually called precessing vortex core (PVC) phenomenon. To illustrate this phenomenon, iso-surfaces of the instantaneous streamwise vorticity obtained by LES are plotted in Figure 6.20 and Figure 6.21. From the iso-surfaces with a streamwise vorticity $\omega_x = -100 s^{-1}$, which is in the order of the characteristic angular speed in the guiding pipe, we note some important features of the flow field. In the guiding pipe the large-scale columnar vortices are clearly seen in the two swirl cases, while the non-swirl case shows an irregular turbulent structure. Slightly downstream, behind the sudden

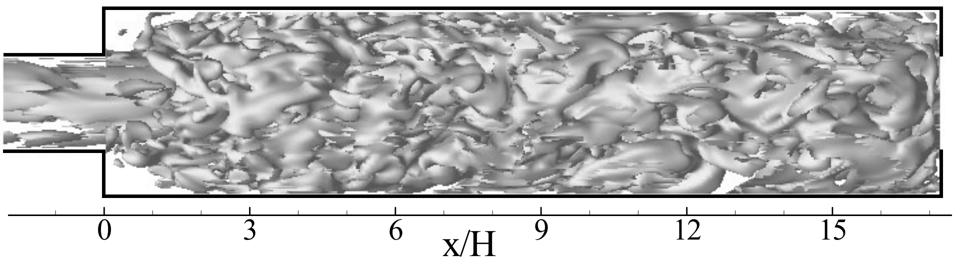

(a) S0

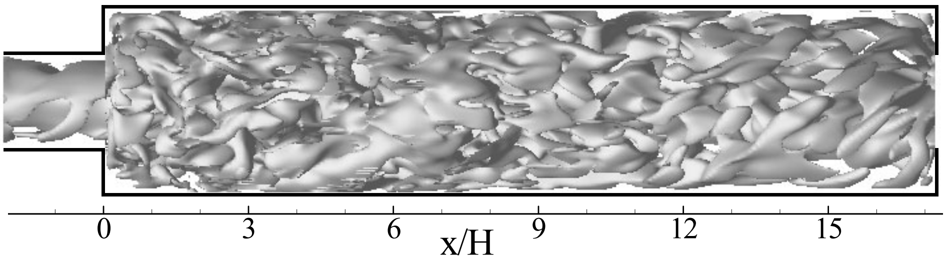

(b) S33

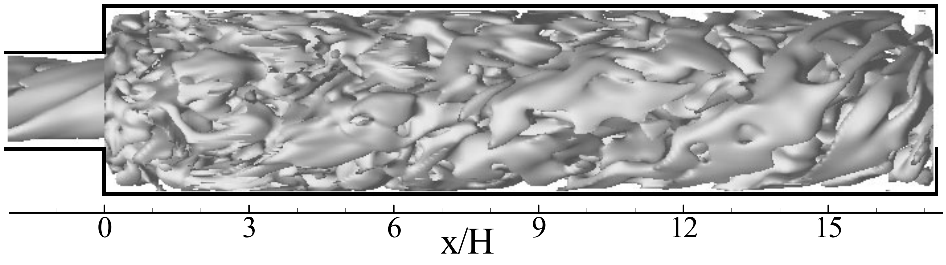

(c) S43

Figure 6.20 3-D iso-surfaces of the instantaneous streamwise vorticity obtained from LES, $\omega_x = (\nabla \times \vec{V})_x = -100 s^{-1}$, (a) S0, (b) S33 and (c) S43.

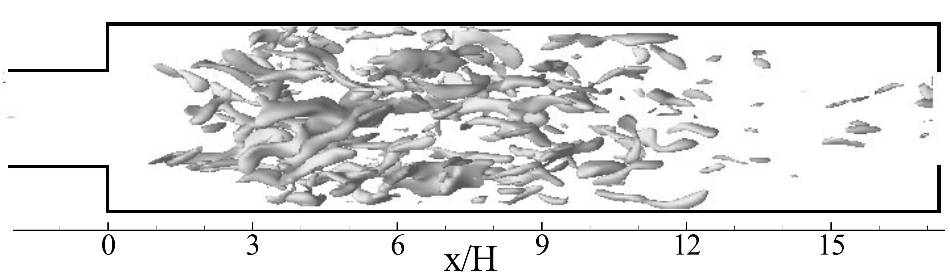

(a) S0

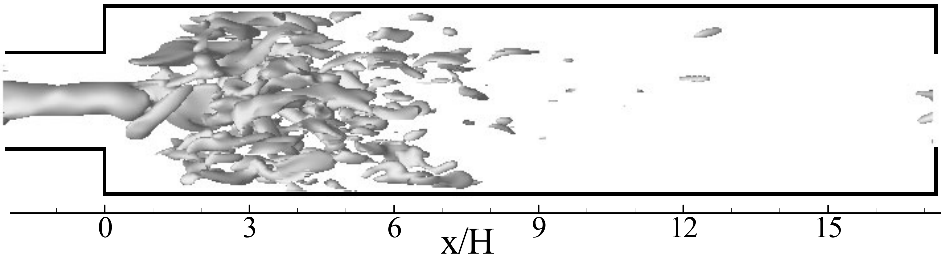

(b) S33

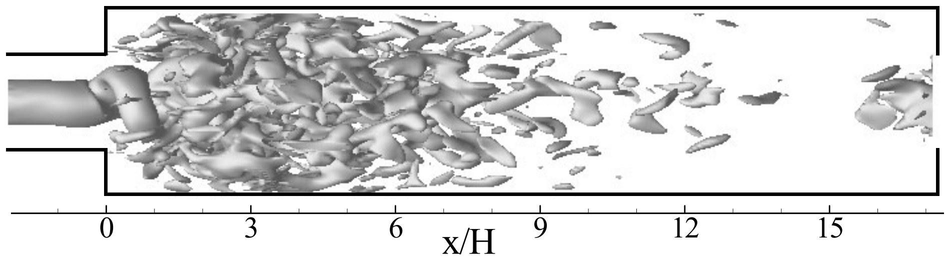

(c) S43

Figure 6.21. 3-D iso-surfaces of instantaneous streamwise vorticity obtained from LES, $\omega_x = (\nabla \times \vec{V})_x = -700s^{-1}$, (a) S0, (b) S33 and (c) S43.

expansion and in the IRZ, the iso-surfaces are of worm-like shape and the sizes are smaller; the orientations of these worm vortices are random. Far downstream, due to the fast decay of turbulence, larger scale vortices are seen. In the non-swirl case, the iso-vorticity surfaces are worm-like as well. In the two swirl cases, in particular the high swirl case–S43, the vorticity iso-surfaces are of two shapes, a columnar near the axis of the combustor, and a helical near the outer walls. The center columnar vortices are long in the axial direction; they are the large-scale swirling motion. The outer helical shape vortices are generated in the wall shear layer.

A higher level of the iso-vorticity surface, $\omega_x = -700s^{-1}$, Figure 6.21, further illustrates the turbulence structures. Two types of vortices can be distinguished, one is related to the random turbulence eddies and one is related to non-turbulent 'well-organized' coherent structures (Coats, 1996). The latter is seen in the swirling flow cases. For Case S33, the large-scale columnar vortex, which is mostly related to the mean swirling flow, starts from the guiding pipe and extends to *x*/H=3. Thereafter, it breaks down to worm-like vortices of smaller sizes. Further downstream, the large scale columnar vortex disappears, as a result of the decay of the swirl motion. Similarly, for Case S43 the large-scale non-turbulent columnar vortices started in the guiding pipe also extend to downstream, breakdown in the IRZ ($1 \le x/\mathrm{H} \le 4$) to smaller worm vortices. The vortices related to the turbulent eddies are mainly found in the upstream zone behind the sudden expansion and in the IRZ. They disappear in the far downstream because of the fast decay of turbulence, in particular in the two swirl cases.

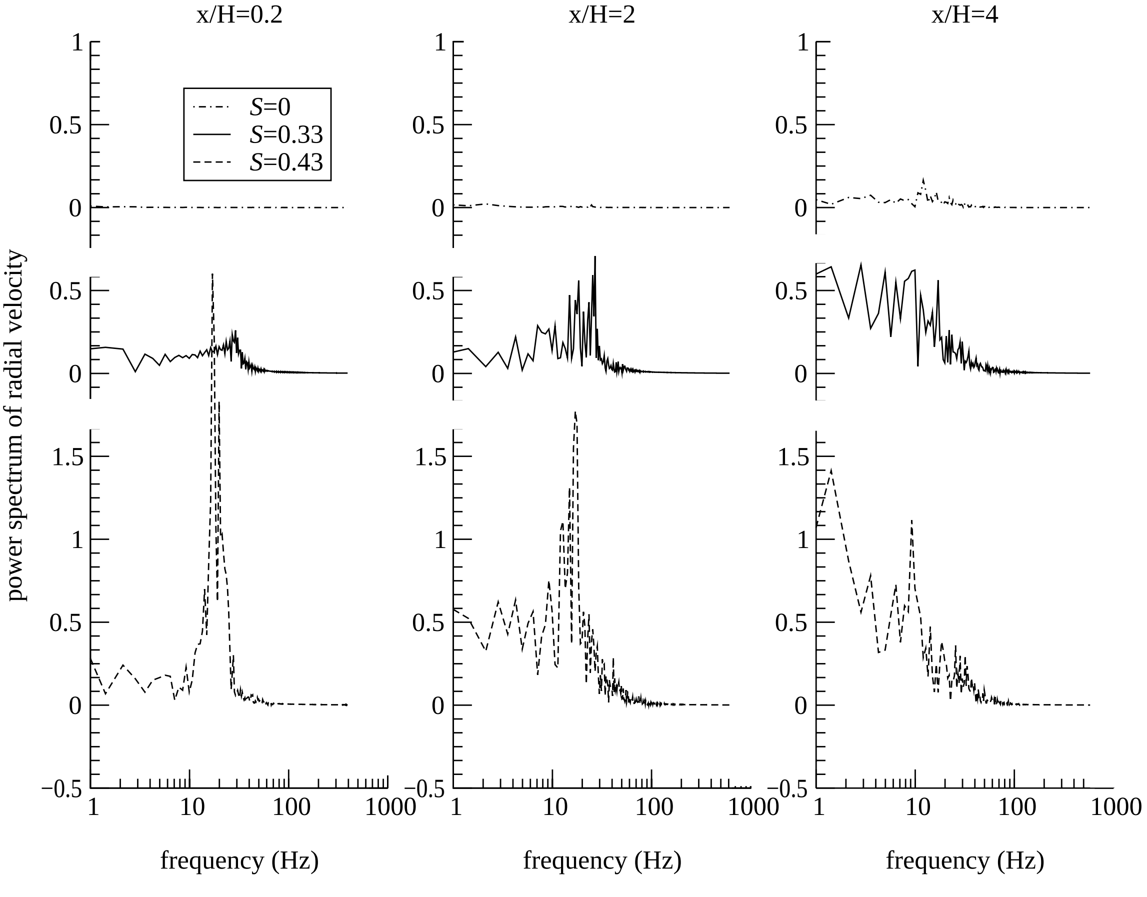

Figure 6.22 Power spectra of radial velocity fluctuations at different axial positions and *r*=0, obtained from LES.

When the center of the columnar vortices moves away from the axis of the combustor, the radial velocity component at the axis of the combustor is nonzero, thus, the radial velocity component can be used to describe the precessing of the columnar vortex core, PVC. Figure 6.22 shows the power spectra of the radial velocity component at different axial positions for the different test cases. The spectra were obtained from the LES data. The non-swirl case shows a rather low level of fluctuation which corresponds to the low value of the radial velocity at the combustor axis (see Figures 6.9 and Figure 6.10). For the moderate swirl case, S33, in particular at *x*/H=2, a peak of the power density spectrum is found at the frequency of f =25 Hz. The Strouhal number, $St = f R_1 / U_b$, is about 0.4. Further downstream no dominant frequency is found. For the high swirl case, S43, at *x*/H=0.2 and 2, a dominant frequency is clearly seen (about 18 Hz, with the Strouhal number about 0.17). This dominant frequency is still evidenced further downstream (*x*/H=4). In the LDV measurement, a similar low frequency (between 18 to 25 Hz) oscillation in the power spectra for the azimuthal/radial velocity, at *x*/H=1.05 and $r = 0$, was observed for the swirl cases. No low frequency oscillation was found for the non-swirl case. The PVC is related to the oscillatory motion of non-turbulent coherent structures, whose oscillation frequency is equal to the dominant frequency found in the spectra. As seen, as the swirl number increases, the oscillatory motion of the coherent structure becomes more pronounced.

The oscillatory motion of the PVC can couple with the premixed flame propagation in gas turbine combustors and it may cause not only the flame instability, but also the oscillation of the combustor structures and noise formation, depending on the level of the oscillation.

6.6 Sensitive study

In addition to the above inlet/outlet boundary conditions study, the influence of some other geometrical and flow parameters on the swirling flows have been assessed also.

6.6.1 Influence of inflow swirl velocity profiles

Two different swirl velocity profiles at the inlet are studied and compared to the ‘standard case’ S43. All the three cases have the same swirl number (*S*=0.43), the same axial velocity profile, but with different azimuthal velocity profile, as shown in Figure 6.23.

The boundaries of the corner- and the internal recirculation zones are shown in Figure 6.24. It is seen that S43B has the longest IRZ and the earliest vortex breakdown. Case S43A has the shortest IRZ and the latest vortex breakdown. The corner recirculation zone of Case S43A is also shorter than that of Cases S43 and S43B. This can be explained as the following: the radial pressure gradient is proportional to the outward centrifugal force generated by swirling motion, which is $\rho w^2 / r$. Since Case S43B has the largest $\rho w^2 / r$ near the axis of the combustor, its radial pressure gradient is the highest. This promotes a more favorable axial pressure gradient for the vortex breakdown to occur earlier. Additionally, a higher azimuthal velocity near the outer wall (as in Case S43A) tends to enhance the transport of the axial momentum in the radial direction towards the pipe wall, therefore the reattaching point of the corner recirculation zone is pushed upstream. This underlines the importance of inlet swirl velocity profiles on the control of the vortex breakdown region and the combustion instability.

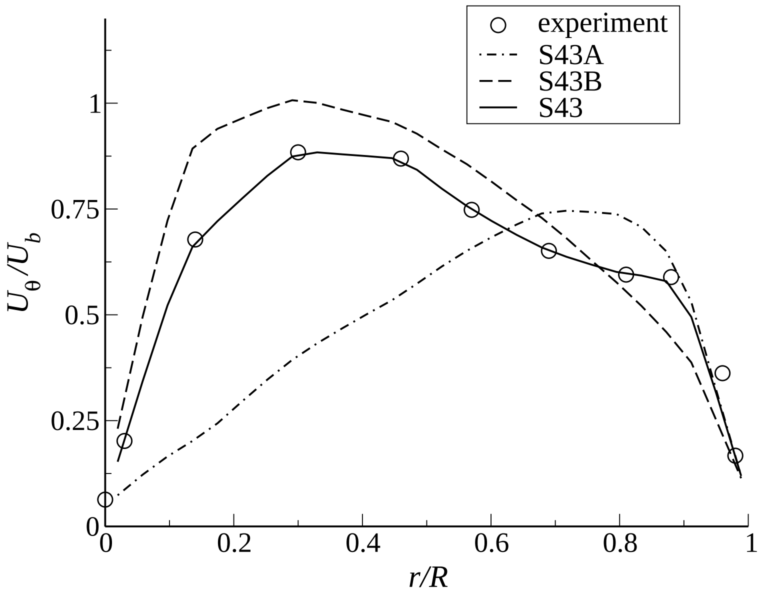

Figure 6.23 Three inflow swirl velocity profiles with the same axial velocity profile and the same swirl number of S=0.43.

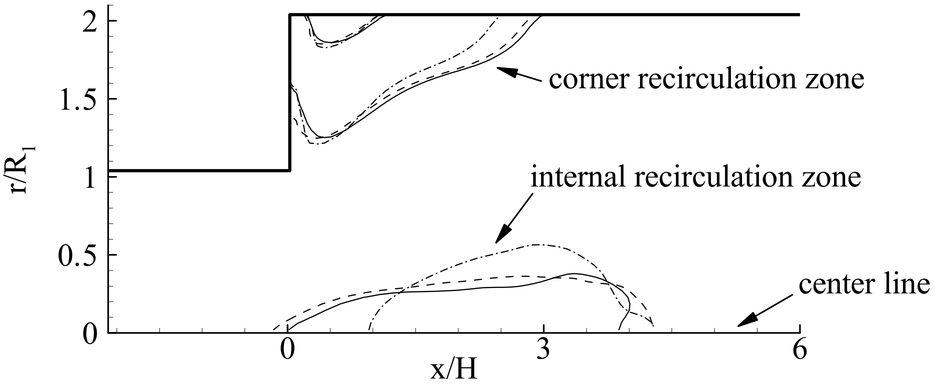

Figure 6.24 Boundaries of the recirculation zones. Solid line: S43; Dashed line: S43B; Dot-dashed line: S43A.

6.6.2 Effect of viscosity

In order to investigate the effects of viscosity on vortex breakdown, a series of swirling flows, with different Reynolds numbers, have been computed. These swirling flows are confined in a circular pipe of radius of 62 mm, and the inlet is of radius of 48 mm, without contraction at the outlet. The change of Reynolds number is made by adjusting the molecular viscosity of the fluid, and at the same time, maintaining the inlet velocity profile. Four Reynolds numbers are studied, which are 100, 1000, 10 000 and 100 000 respectively. In order to find out the critical swirl number (at which vortex breakdown starts to occur) at each Reynolds number, flows with different swirl numbers are computed.

The minimum axial velocities at different Reynolds numbers are shown in Figure 6.25. It is seen that the minimum axial velocity along the pipe axis decreases monotonously as the swirl number increases. When the swirl number is higher than the critical swirl number, the flow starts to reverse. For the case Re=100, the flow is laminar, and the critical swirl number is about 0.66. The critical swirl number decreases to 0.36 after increasing Reynolds number to 1000. Increasing Reynolds number even further, the critical swirl number does not change substantially. This is due to the fact that viscous dissipation on the flow kinetic energy is weak at high Reynolds number flows; the flow is easier to develop into the vortex breakdown structure. When the Reynolds number is large enough, the viscosity effect is negligible; the flow and turbulence structures are insensitive to the change of Reynolds number.

One may note that since there is a backward-facing step at the inlet, these cases has much lower critical swirl number for the onset of vortex breakdown than the straight pipe cases shown in Figure 6.2, although these cases have the same axial inflow profile (plug flow) and azimuthal velocity profile (solid body rotation). This is due to the fact that the geometry expansion introduces an axial velocity deceleration and hence pressure increasing in the axial direction, which is in favor of the onset of vortex breakdown.

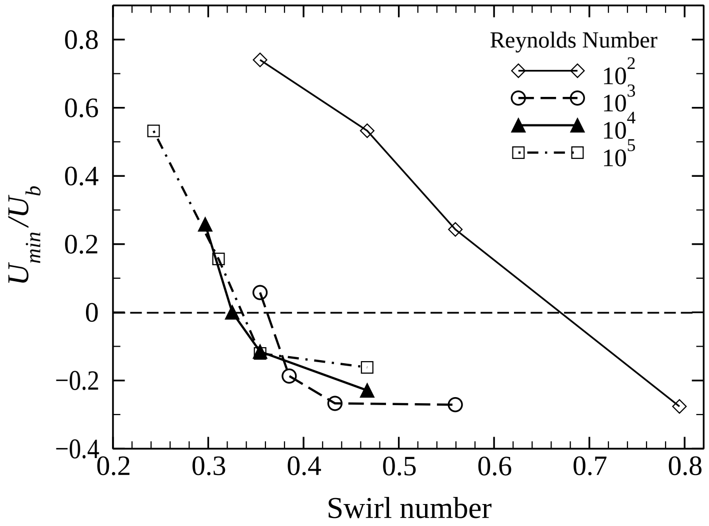

Figure 6.25 Minimum axial velocity along the central line at different swirl numbers and Reynolds numbers.

6.6.3 Influence of outlet geometry

One may expect that the outlet geometry has an important effect on the flow structure as the outflow condition does. To confirm the effect of the outlet geometry, two different outlet configurations are studied: one with a geometry contraction at outlet, i.e. the previous case S43; another one without geometry contraction at outlet. In both cases, the computational domain is $-2.1\text{H} \le x \le 17.44\text{H}$.

Figure 6.26 shows the mean axial and the azimuthal velocity profiles at two axial positions. As seen, the discrepancy between the two outlet geometries is rather small at these rather upstream axial positions, particularly in the axial velocity profiles. At far downstream, the effect of the outlet geometry is more noticeable, as seen in the axial velocity variation along the axis of the combustor, shown in Figure 6.27. Due to the fact that the outlet area decreases as a result of the geometry contraction, the flow is accelerated quickly at the outlet. As shown in Figure 6.27, the agreement of the calculated mean axial velocity (with contraction geometry) with the experimental data is good.

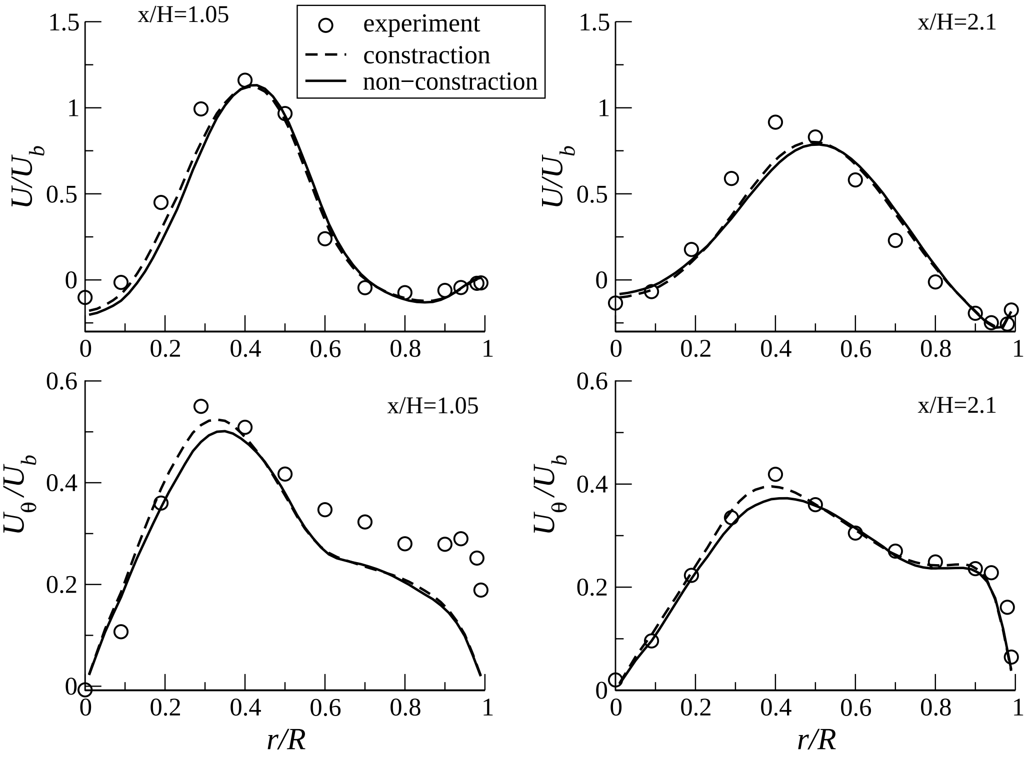

Figure 6.26 Radial profiles of time averaged axial and azimuthal velocity components at two axial positions of test case S43, from the experiment and LES using two different outlet geometry configurations.

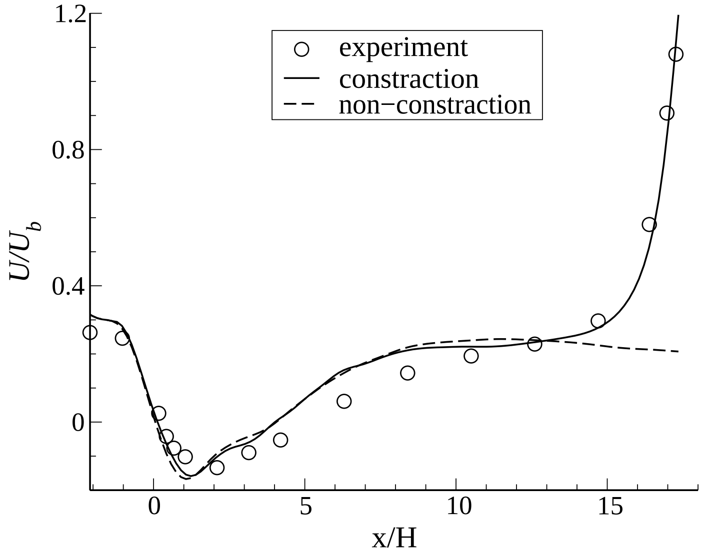

Figure 6.27 Time averaged axial velocity component along the axis of the dump combustor of test case S43, from the experiment and LES using two different outlet geometry configurations.

Chapter 7

LES of turbulent lean premixed flame in a jet engine afterburner

7.1 Experimental set up of a turbulent lean premixed propane/air flame

To assess the performance of level set flamelet library approach, simulations of premixed flames have been compared to an experimental flame. This experiment was conducted in Volvo Aero Corporation (Sjunnesson et al., 1991), and named as VR–1.

In this thesis work, one of VR–1 lean premixed flames is chosen to be simulated. It is a bluff body stabilized lean propane/air turbulent premixed flame, which is schematically shown in Figure 7.1. The combustion chamber is a simple rectangular channel with a channel height of 120 mm and width of 240 mm. The propane/air mixture has an equivalence ratio of 0.6 and inlet temperature 600K. Mixture enters the chamber from left at a mass flow rate 0.6 kg/s. The unstretched laminar flame speed is s_L=0.76 m/s (Nilsson & Bai, 2002). The flame holder is of prismatic triangular shape, with the side length H=40 mm. The inflow velocity is about 36 m/s with a Reynolds number about 85000 based on the inflow condition and height of the combustion chamber.

The velocity, temperature, and mole fractions of species O_2, CO_2 and CO were measured using Laser Doppler Anemometry (LDA) and gas analysis equipment. Details about the experiment can be found in Sjunnesson et al. (1991). Based on the measurement data and the laminar flame calculation we estimated that the flame is in the corrugated flamelet regime, with a Karlovitz number about 0.1–0.7. The used coordinate system is shown in Figure 7.1, with the origin of the coordinate at the center of the back side of the flame holder.

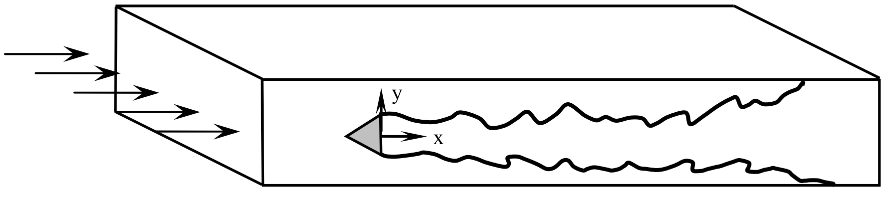

Figure 7.1 Sketch of the experimental set up.

7.2 Boundary conditions and grid resolution

7.2.1 Boundary conditions

No-slip boundary condition is applied along all solid walls. For scalars, such as density and *G*, zero-gradient condition is used. A mass-conserving convective outflow condition is applied (see Section 5.3.3). Rescaled inflow library condition, which is explained in detail in Section 5.3.2, is used here. In the experiment, the mean axial and vertical velocities (in the x and y directions respectively, shown in Figure 7.1) and their fluctuations were measured at several positions by LDA. The data at $x = -100\,\text{mm}$ station are used to rescale the turbulent inflow library extracted from a separate turbulence calculation of a rectangular channel. Like the library used for swirling flows, 10 000 sections are stored in the library to get steady statistic properties at the inflow.

7.2.2 Grid resolution

Due to the limitation of the computation resource and the large computation domain of VR–1 case, very fine grid resolution is not affordable. Several grid independence tests have been conducted. By comparing the convergence of the mean temperature and mean flow velocities with respect to the refinement of grid resolution, it was shown that the grid with 300, 120, 120 grid points in the streamwise, span-wise and transverse directions, respectively, is satisfactory. The grid size is about 1–3 mm.

7.3 Qualitative analysis

7.3.1 Mean flame position

Figure 7.2 compares the calculated time averaged mean flame position with the measured value, which was derived from the measured CO peak values (Sjunnesson et al., 1991). As seen, the LES data is in good agreement with the experimental data.

7.3.2 Turbulent flame brush thickness

The thickness of the time averaged mean flame brush may be estimated using the standard deviation of *G*,

$$l_{F,t} \sim \left(\overline{G'^2}\right)^{1/2}\Big|_{\overline{G}=0} \tag{7.1}$$

evaluated at the time averaged mean flame front, $\overline{G} = 0$. Figure 7.3 shows the development of the mean flame thickness along the streamwise direction. No experimental data is shown, since it is not available in the experiment report. Three fit curves are also drawn in Figure 7.3.

It is seen that near the immediate downstream of the flame holder, the mean flame thickness increases almost linearly. Far downstream the increase of the mean flame thickness is proportional to square root of x. This tendency is in good agreement with the Taylor theory of turbulent diffusion of passive surfaces in isotropic turbulence, as discussed by Lipatnikov and Chomiak (2002) in detail. For the range between, i.e. 2<x/H<10, both fit curves show big discrepancy.

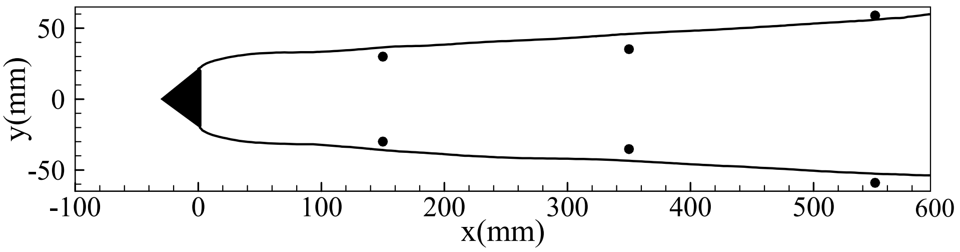

Figure 7.2 Mean flame position calculated (solid line) and derived from the experiment (dots).

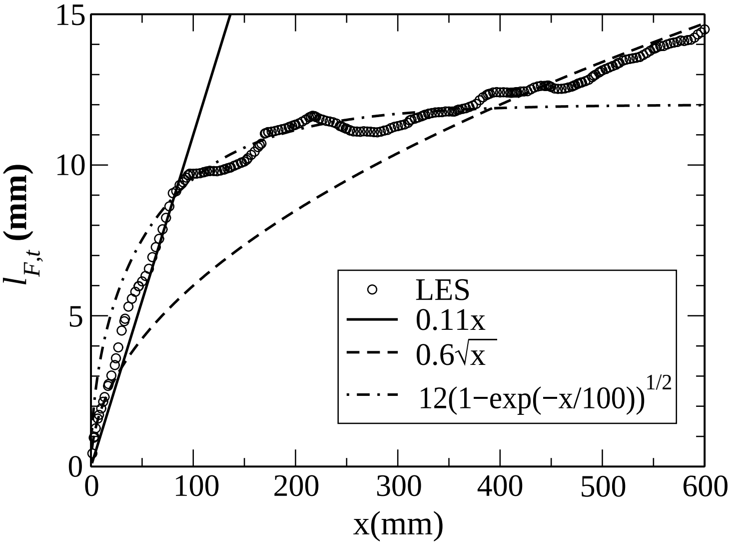

Figure 7.3 Development of the thickness of the mean turbulent flame brush along the streamwise direction.

Peters (2000) proposed a transport equation for the time averaged variance of *G*. Assuming that the time averaged mean flow velocity (U) and the turbulent properties at the integral scale (characteristic length and time, l_0 and t_0) are constant after the flame holder, one can show that the balance between terms for the convection, generation and destruction of the *G*-variance leads to an approximation of the thickness of the mean flame brush

$$l_{F,t} \sim a l_0 \left(1-\exp\left(-bx/Ut_0\right)\right)^{1/2} \tag{7.2}$$

From the experimental data, the mean flow velocity is about 50 m/s (typical flow speed in front of the flame surface). The characteristic length and time scale at the integral scale are about 40 mm and 4 ms, respectively. Using a model constant a=0.3 and b=2, one obtains the third fit curve, the dash-dotted line in Figure 7.3. The transport equation for the G-variance yields good agreement with the mean flame brush thickness calculated from LES in the intermediate region.

7.3.3 Flame surface and turbulence structure

Figure 7.4 shows typical instantaneous stream-wise vorticity iso-surfaces and the associated wrinkled flame surface. In front of the flame holder, the level of the vorticity is relatively low. Turbulence is significantly generated in the shear layer after the flame holder as shown in Figure 7.4(a) and 7.4(b), where high velocity gradient exists near the flame front, with high vorticity level.

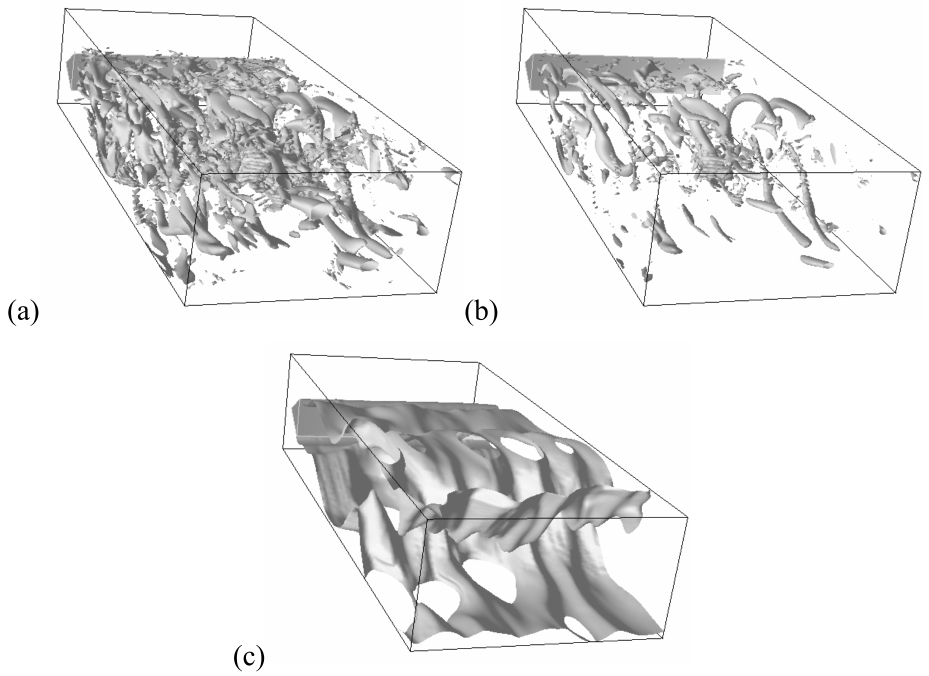

(a) (b)

(c)

Figure 7.4 Instantaneous streamwise vorticity iso-contours: (a) $\omega_x = 500\,\mathrm{s}^{-1}$; (b) $\omega_x = 1000\,\mathrm{s}^{-1}$; (c) instantaneous flame surface, G=0, at the resolved grid scale.

In the hot post-flame region the vortex size is larger since heat release increases the molecular viscosity. The vortex is highly an-isotropic: vortices downstream of the flame holder are long in the streamwise dimension, with different vortex filaments clearly seen in Figure 7.4. The flame surface reflects the vortex structure; in particular, the wrinkling in the span-wise direction is obviously related to the structure of the streamwise vortex. The ‘holes’ on the flame surface are the locations where the flame is attached to the combustion chamber walls.

7.4 Velocity field

Figure 7.5 shows the mean streamwise velocity distribution along the center line. It is shown that a large size reverse flow zone is attached to the flame holder, which is good for flame stabilization. The predicted length of central circulation zone is about two times of flame holder width, which is a little shorter than the experimental result. The profiles of the mean streamwise velocity *U* at 3 transverse stations, where LDA measurement data are available, are shown in Figure 7.6. The overall agreement between experimental and computational results is good.

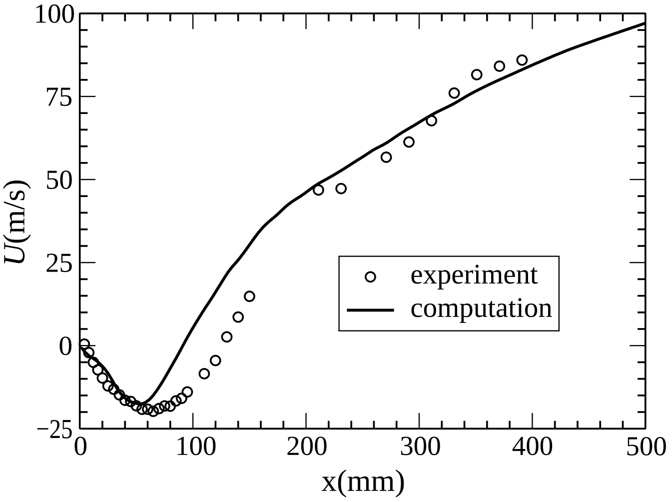

Figure 7.5 Mean streamwise velocity distribution along the center line.

7.5 Major species and temperature

The mean major species and temperature distributions are closely related to the mean flame thickness and mean flame position. Once they are properly simulated in LES, the mean major species field and temperature are also properly simulated. The time averaged CO_2 and O_2 mole fractions at three transverse stations are plotted in Figure 7.7 and Figure 7.8 respectively. Figure 7.9 shows the mean temperature predicted at the three transverse stations. The agreements of the mean velocity and major species from LES with the measurement are reasonably good.

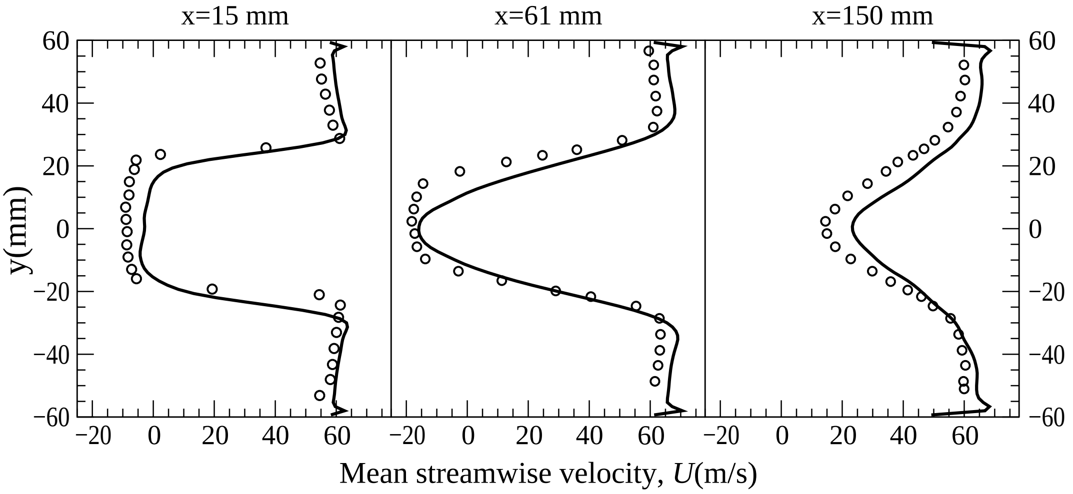

Figure 7.6 Mean streamwise velocity profiles at three transverse stations. Lines: computation; Circles: experiment.

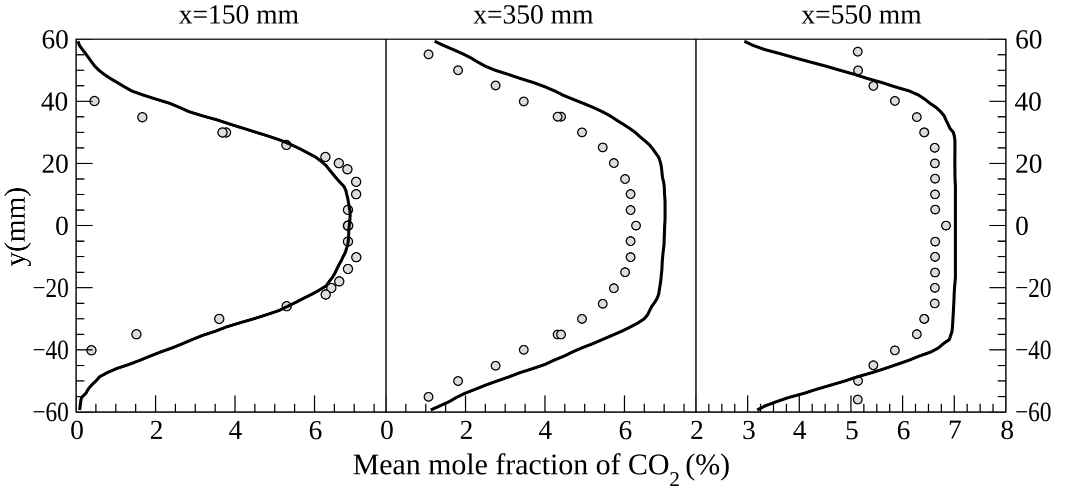

Figure 7.7 CO_2 mole concentration at three stations. Lines: computation; Circles: experiment.

From Figures 7.7–7.9, it is seen that the big discrepancy exists in the near wall region at the x =550 mm station, where the flame is about to attach the wall. The mean temperature and major species are very sensitive to the position of reattachment point. A little difference of flame position will move some part of the flow field from unburnt zone to burnt zone, or vice versa. In addition to this, neglected history effect and radiation in this used stationary flamelet library method may contribute also to this disagreement.

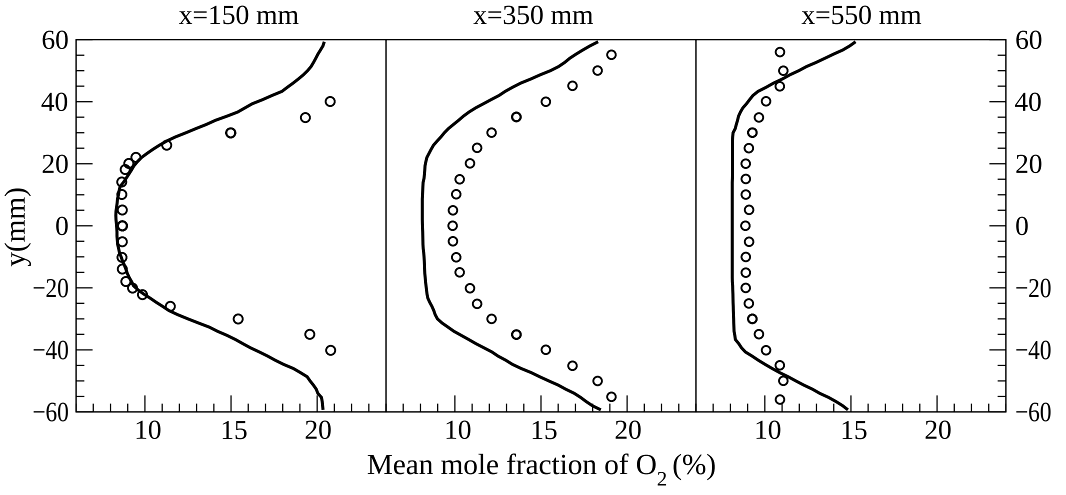

Figure 7.8 O_2 mole concentration at three stations. Lines: computation; Circles: experiment.

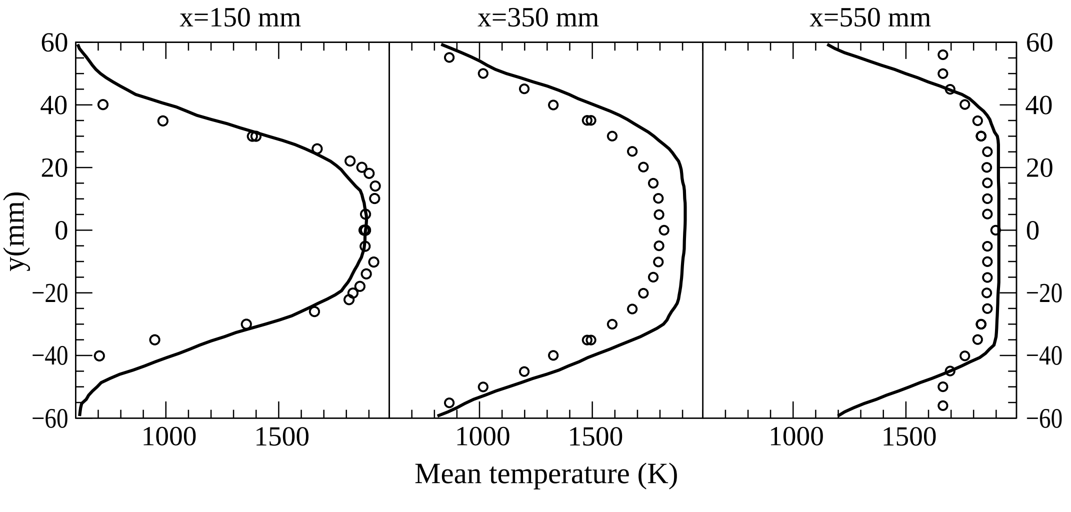

Figure 7.9 Mean temperature profiles at three stations. Lines: computation; Circles: experiment.

7.6 Intermediate species CO

An important effect of SGS eddies is the significant enhancement of the flame surface density in the SGS scales, which can increase the time averaged mean concentration of minor species in the mean flame brush, as already discussed by Nilsson and Bai (2002). From other point of view, the predicted distance to the flame front (resolved *G* value in LES) is quite different from the distance to the real flame front (with SGS wrinkle). If one uses the resolved *G* as the parameter to calculate CO concentration from the Flamelet Library directly, it will give a much lower value than real one.

This effect has been studied in the RANS framework previously (Peters, 2000; Nilsson & Bai, 2002), here, similar idea is used in LES. As already illustrated in Section 4.4.2, the distance to the flame is rescaled by a factor, ξ. In this work, the ratio s_{LES}/s_L is used to estimate ξ. Figure 7.10 shows a typical probability density function of the factor, ξ, which is evaluated in the immediate grid cell of the instantaneous flame front, on the unburnt side, and at the streamwise position x=150 mm. As seen, the value of the SGS wrinkle effect factor varies in the range of 1–20. Its mean value is about 5.5.

Figure 7.11 shows the mean CO mole fraction calculated using two different methods, with and without the inclusion of SGS wrinkling. As seen, the effect of SGS wrinkling is rather strong. With SGS wrinkling, the present flamelet model gives results in closer agreement with the experimental data than those obtained without the SGS wrinkling, although certain discrepancy exists in the peak CO value and the spatial location of the CO peak. But at the center post flame zone, CO changes only slightly. For major species and temperature, both methods (with and without SGS wrinkling model) predict almost the same value. It illustrates that SGS wrinkling only influences the intermediate species concentration around the mean flame position significantly.

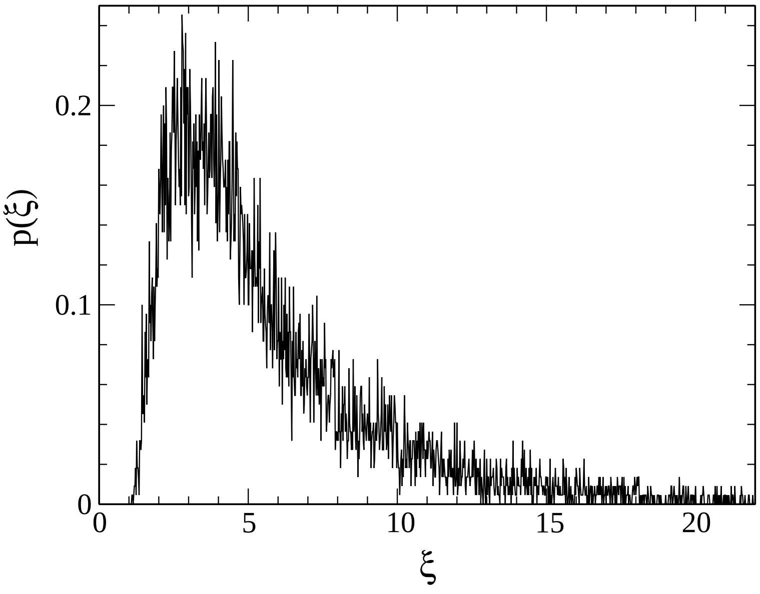

Figure 7.10 PDF of the SGS wrinkle factor at the $\overline{G}=0$ (on the unburnt side) and x=150mm.

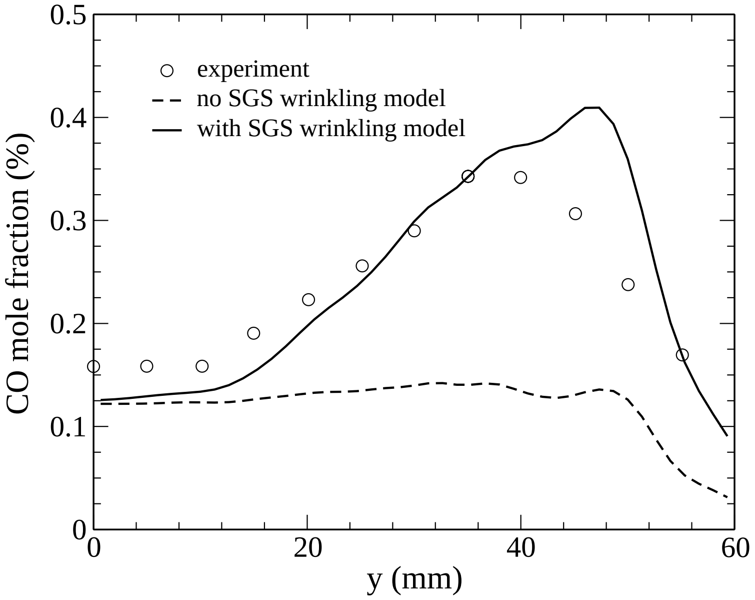

Figure 7.11 CO mole fraction (at $x = 350\,\mathrm{mm}$ station) calculated with and without the inclusion of SGS wrinkling model.

Chapter 8

Study flame/eddy interaction using level set approach

From the LES results presented in Chapter 7, one may note that the unresolved SGS eddies can affect the flame surface area significantly, and this has an important impact on the distribution of intermediate species, as well as the propagation of the resolved flame front. A fundamental question is how fine the LES grid should be used to have a satisfactory result without heavily depending on the SGS flame wrinkling models. To answer this one needs to examine the asymptotic behavior of flame wrinkling as the 'resolution' of the LES filter size and grid size decrease to the DNS level. This could be carried out by sequential LES. However, it would demand excessively long computational effort that is beyond the time scale of this thesis work.

A feasible approach to investigate the effect of small unresolved SGS eddies on the wrinkling of premixed turbulent flame, is to apply *G*-equation to study a 2-D flame propagation problem of flame front in a 'prescribed turbulence' field. A related work has been reported previously by Denet (1998).

8.1 The prescribed turbulence field

The flow field is assumed to consist of eddies of *N* different scales, whose instantaneous velocity component is

$$\begin{cases} u(x,y,t) = \sum_{i=1}^{N} a_i \cos(2\pi y / l_i + \varphi_i) \cos(2\pi t / \tau_i + \psi_i) \\ v(x,y,t) = 0 \end{cases} \tag{8.1}$$

The subscript *i* denotes the *i*-th eddy, and its velocity, length and time scale are a_i, l_i and τ_i, respectively. The largest eddy is the first one. Among these eddies, certain relations are assumed,

$$l_i = l_1 / i \tag{8.2}$$

$$l_i = a_i \, \tau_i \tag{8.3}$$

In (8.1), φ_i and ψ_i are random phase angles associated with *i*-th eddy. Further, we assume that energy transfer within different eddies follow the energy cascade theory, i.e., the dissipation rate at different scales is equal, thereby a scale relation is held:

$$a_i^3 / l_i = a_1^3 / l_1 \tag{8.4}$$

$$\tau_i / \tau_1 = \left(l_i / l_1\right)^{2/3} \tag{8.5}$$

Since the transverse velocity component $v(x,y,t)$ is zero, no over-hang (multiple crossings) happen, so the G-field can be represented by

$$G(x,y,z,t) = x - h(y,t) \tag{8.6}$$

Substitute (8.6) into the G-equation (4.7), one obtains a height-equation (or h-equation)

$$\frac{\partial h}{\partial t} = u - s_L\left(1 + \left(\partial h / \partial y\right)^2\right)^{1/2} \tag{8.7}$$

Here the flame speed is the laminar flame speed since all the flame wrinkles are considered in the simulation. The h-equation can be made non-dimensional using $h^* = h / l_1$, $y^* = y / l_1$, $l_i^* = l_i / l_1$ and $t^* = t / \tau_1$. Introducing a Gibson length scale l_G at which the eddy turnover velocity is equal to the laminar flame speed s_L (Peters, 2000), the normalized h-equation has the form:

$$\frac{\partial h^*}{\partial t^*} = \frac{u}{a_1} - \left(\frac{l_G}{l_1}\right)^{1/3}\left(1 + \left(\partial h^* / \partial y^*\right)^2\right)^{1/2} \tag{8.8}$$

$$\frac{u}{a_1} = \sum_{i=1}^{N} l_i^{*1/3} \cos\!\left(\frac{2\pi y^*}{l_i^*} + \varphi_i\right)\cos\!\left(\frac{2\pi t^*}{l_i^{*2/3}} + \psi_i\right) \tag{8.9}$$

To capture the cusps developed by this Hamilton–Jacobi type equation, a high order WENO scheme is used to discretize equations (8.8) and (8.9).

8.2 Flame/single-scale eddy interaction

To study the effect of a single-scale eddy, the flow field is assumed to consist of one eddy scale, i.e., (8.9) is rewritten as

$$\frac{u}{a_1} = l_i^{*1/3} \cos\!\left(\frac{2\pi y^*}{l_i^*} + \varphi_i\right)\cos\!\left(\frac{2\pi t^*}{l_i^{*2/3}} + \psi_i\right), \qquad i = 1,2,....,20 \tag{8.10}$$

Figure 8.1 shows a typical wrinkled flame front calculated with a single eddy scale ($l_1 = l_G$ and N=1 in equations (8.8) and (8.9), respectively, or i=1 in (8.10)). The calculation was initiated from a planar initial flame and continued a sufficient long time till a periodic flame development is reached. The figure shows a wrinkled flame surface with one small wrinkle scale embedded to a large wrinkle scale. The flame surface evolves in time with cusps in several locations.

To quantify the effect of small eddies on the flame wrinkling, a scalar, the flame surface area ratio, is defined. It is the ratio of the flame surface area wrinkled by the eddies to the non-wrinkled smooth flame surface area, calculated by

$$\xi_n = \frac{1}{T}\int_{t_0^*}^{t_0^*+T}\int_0^1 \left(1+n(\partial h^* / \partial y^*)^2\right)^{1/2} dy^* dt^* \tag{8.11}$$

If n=1, ξ_1 is the flame surface area ratio of the 2-D flame (flame surface degenerated to a flame line). An estimation of the 3-D flame surface wrinkling is given by ξ_2, which is based on the assumption that the wrinkling behavior in the z-direction is similar to the y-direction. In the above formulation, time averaged quantity is used to indicate the characteristic flame surface area ratio. t_0^* and T should be large enough to eliminate the effect of initial field and to obtain convergence in the time averaging calculations.

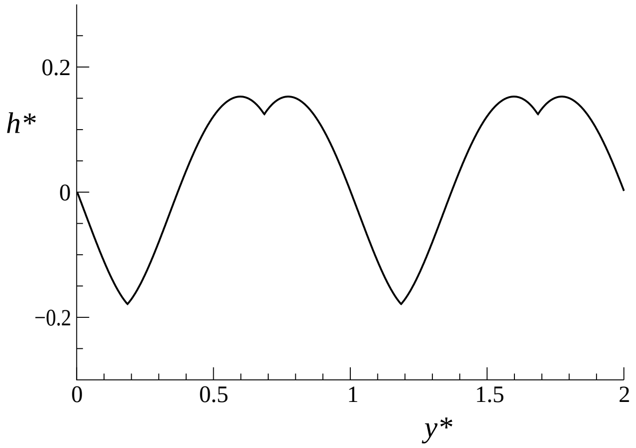

Figure 8.1 A typical flame front shape by a single eddy scale.

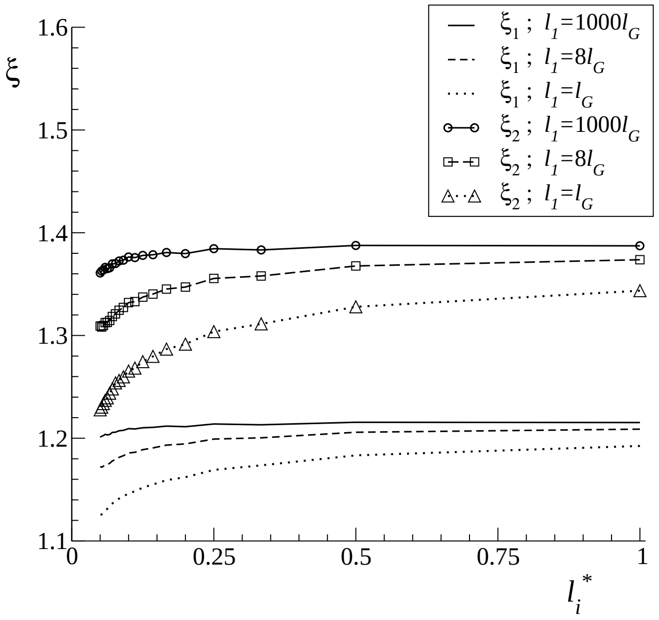

Figure 8.2 Flame surface area ratio from one single eddy scale at different l_1 / l_G ratio.

For the case i=1 and $l_1 = l_G$, it is shown that $\xi_1 = 1.19$ and $\xi_2 = 1.34$. This shows a 20-30% increase of the flame surface area due to eddy wrinkling.

Different l_1 / l_G ratio and eddy scales are investigated. The results are shown in Figure 8.2. It is found that, for constant l_1 / l_G ratio, the larger the eddy size ($l_i^* = l_i / l_1 = 1/i$) the larger the wrinkled flame surface area. It is shown that increasing the ratio of l_1 / l_G and keeping l_i^* constant leads the flame wrinkling to grow monotonically.

8.3 Flame/multiple-scale eddy interaction

To study multiple-eddy scales effect on the flame wrinkling, more test cases are studied. Figure 8.3 shows a typical wrinkled flame front calculated with 20 eddy scales ($l_1 = l_G$ and N=20 in equations (8.8) and (8.9), respectively), in which, t_0^* was chosen sufficiently long, so that the influence of the initial flame surface position is negligible and the flame shape is typical. The figure shows a highly wrinkled flame surface with different wrinkle scales. The flame surface evolves in time with cusps in several locations. The shape of the flame front is fundamentally different from the single-scale eddy flame.

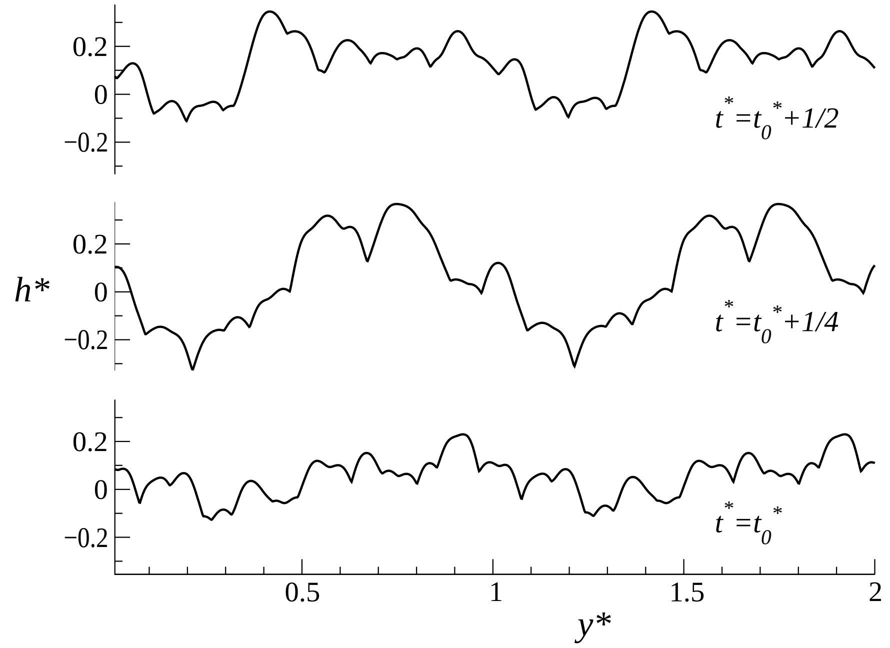

Figure 8.3 Instantaneous flame fronts simulated using h-equation with 20 different eddy scales.

To examine the asymptotic behavior of the flame front wrinkling as the eddies become smaller, the eddies are successively removed from the presumed turbulence field. This is done using (8.12):

$$\frac{u}{a_1} = \sum_{i=n}^{20} l_i^{*1/3} \cos\left(\frac{2\pi y^*}{l_i^*} + \varphi_i\right) \cos\left(\frac{2\pi t^*}{l_i^{*2/3}} + \psi_i\right), \quad n = 1, 2, ..., 20 \tag{8.12}$$

In this formulation, it is assumed that eddy scales $i \in [1, n-1]$ are resolved and removed from the flow filed, and eddy scales $i \in [n, 20]$ are the remaining eddies (to model the unresolved SGS scales). In analogy to the LES system, the filter size Δ is l_n. By successively removing the large eddies (i.e. increase n in (8.12)), the filter size, Δ, decreases continually, hence a series of flame surface area ratio is calculated. This process is schematically shown in Figure 8.4.

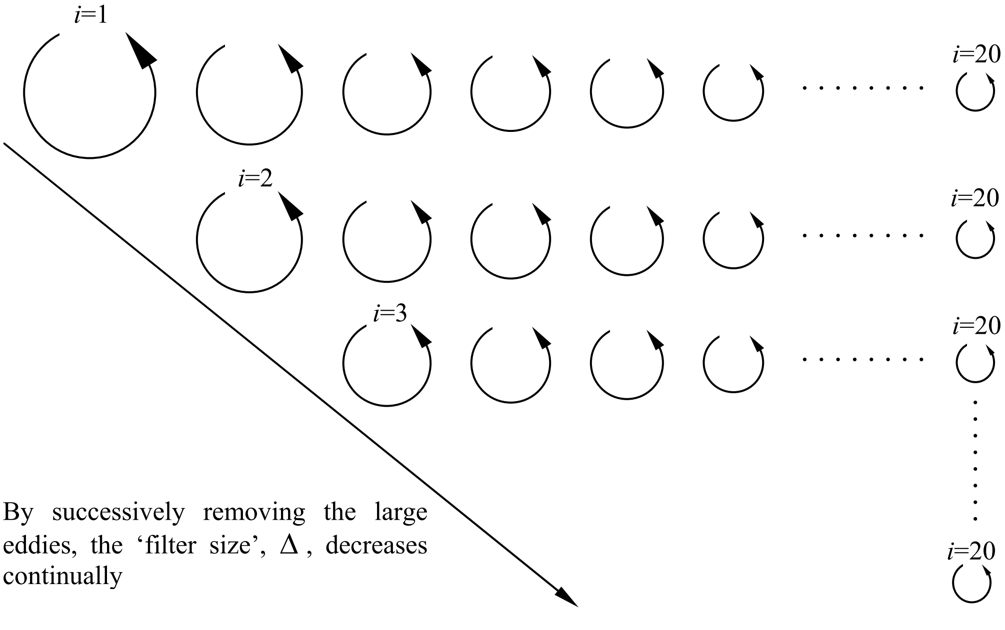

Figure 8.4 A schematic illustration of the process of decreasing filter size.

Figure 8.5 shows the mean flame surface area ratio (averaged over 15 000 time steps) as a function of the spatial filter size, Δ. Three test cases are plotted in Figure 8.5. In the case $l_N = 50l_G$ the smallest eddy is much larger than the Gibson scale. In the case $l_N = 0.05l_G$ the largest eddies are on the order of Gibson scale. In the third case the Gibson scale is in between the largest and the smallest eddies ($l_1 = 8l_G, l_N = 0.4l_G$). As seen, ξ for the case with $l_N = 0.4l_G$ is higher than that for the other two cases. It indicates that eddies of Gibson scale are most effective in wrinkling the flame surface. This result confirms the argument of Peters (2000).

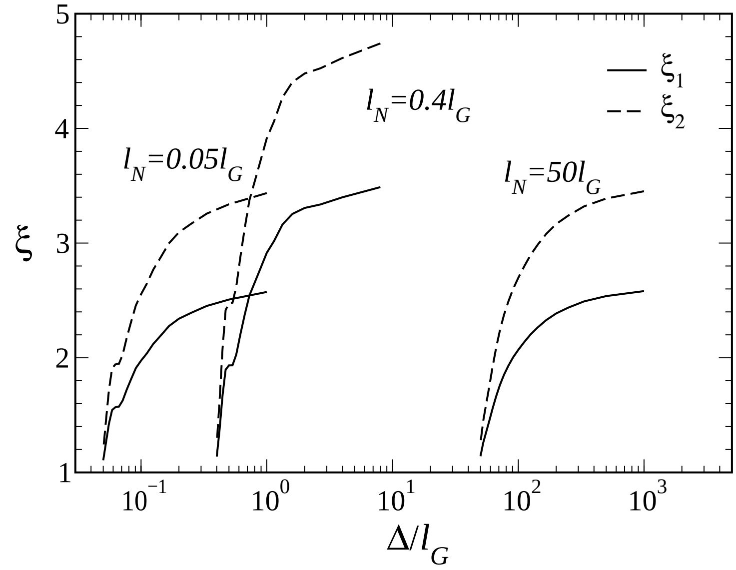

Figure 8.5 Flame surface area ratio as a function of the resolved large eddy scale Δ.

As expected, when the filter size decreases, the wrinkled flame surface area ratio decreases monotonically. More interestingly, the results show that when Δ is large, $d\xi / d\Delta$ is small, which implies that rather fine grid resolution and filter size are needed to resolve most of the flame surface area ratio. For example, to resolve 50% of the ξ for the case of $l_N = 0.4 l_G$, 90% of the eddies have to be resolved.

8.4 Discussions

It should be pointed out that in real flames wrinkling of flame front is due to several different physical mechanisms such as flow/eddy convection, diffusion-thermal instability, hydrodynamic instability, buoyancy effect, etc. (Williams, 1985b). Since the turbulence field is presumed here, the heat release and density change are not included in the model. Thus, the diffusion-thermal and hydrodynamic instability mechanisms and buoyancy effects are not considered in the model. The present results show mainly the effect of convection of turbulence eddies on the flame. It is shown that small eddies would exert significant effect on the flames. In practical flames this effect may be different. This issue is not clear yet and more theoretical and computational efforts are needed.

An obvious conclusion from the study presented in this chapter is that, the level-set approach indeed can model, rather sensitively, the flame wrinkling by eddies.

Chapter 9

Summary of papers and proposal for future work

9.1 Summary of papers

- **Paper 1**

  Wang P., Bai X.S., Wessman M. and Klingmann J. Large eddy simulation and experimental studies of a confined turbulent swirling flow. Physics of Fluids, vol. 16(9): 3306–3324, 2004.

Laser Doppler velocimetry (LDV) measurement and large eddy simulation (LES) were used to study confined isothermal turbulent swirling flows in a model dump combustor. The aim was to gain deeper understanding of the flow and turbulence structures in dump combustors and to examine the capability of LES for prediction of turbulent swirling flows. A refractive index matching technique is used in the LDV measurement to improve the near-wall data. A high-order finite difference scheme on Cartesian grids with a scale-similarity subfilter scale model is used in the LES. Turbulent inflow boundary conditions with different energy spectra, different outflow boundary conditions, and grid resolutions are tested in the LES. Three test cases with different swirl numbers and Reynolds numbers are studied in the measurements and the simulations. The Reynolds numbers range from 10 000 to 20 000, and the swirl number is varied from 0 to 0.43. With appropriate inflow, outflow boundary conditions, and fine grid resolution, the LES results are in fairly good agreement with the LDV data. The experimental and numerical results show that turbulence in the dump combustor is highly anisotropic behind the sudden expansion and in the internal recirculation zone near the axis of the combustor. Turbulence decays rapidly along the streamwise direction downstream, and the structure of turbulence depends highly on the level of inlet swirl. At low swirl numbers, turbulence is primarily generated in the shear layer behind the sudden expansion; at high swirl numbers the near axis flow becomes very unstable and vortex breakdown occurs. The shear layer near the axis of the combustor caused by vortex breakdown generates most of the turbulent kinetic energy. Large-scale motions (coherent structures) are found in the near axis vortex breakdown region. A helical flow in the guiding pipe breaks down near the sudden expansion to form a large bubble-like recirculation zone whose center moves slowly around the axis. Downstream of the bubble the core of the rotational large scale azimuthal flow motion is off the combustor axis and rotates around the axis at a frequency about 18–25 Hz (Strouhal number about 0.17–0.4). As the swirl number increases the coherent structure becomes more evident, and the internal recirculation zone moves upstream. LES successfully simulated the vortex breakdown, the internal recirculation zones and the anisotropic turbulence structures for all the swirl numbers considered.

- **Paper 2**

  Wang P., Bai X.S. Large eddy simulation of turbulent swirling flows in a dump combustor: a sensitivity study. International Journal for Numerical Methods in Fluids, accepted for publication, 47: 99–120, 2005.

  Large eddy simulations (LES) of confined turbulent swirling flows in a model dump combustor are carried out. The simulations are based on a high order finite difference method on a Cartesian grid, with the sub-grid scale stress tensor modeled using a scale-similarity model. One aim of this work is to study the physics of the flow and to evaluate the performance of LES method for simulation of the major features of turbulent swirling flows—the vortex breakdown, the highly anisotropic and fast-decaying turbulence structure. Comparisons of LES results with experimental data are made. The LES results are shown to be in reasonably good agreement with the experimental data if appropriate inflow and outflow boundary conditions are imposed. Influences of inflow/outflow conditions, combustor geometry, and inlet swirl profile as well as the Reynolds numbers, on the vortex breakdown and turbulence structures, are investigated subsequently. It is found that, at very high swirl levels, the influence of the outflow conditions is significant, not only at downstream near the outlet, but also at far upstream. At low Reynolds numbers, the onset of vortex breakdown is fairly sensitive to the change of Reynolds number; however, at high Reynolds numbers it is rather insensitive to the Reynolds number changing. The different inlet conditions are shown to have an important effect on the flowfield, whereas the 'random-fluctuation' inlet condition is almost equivalent to the 'laminar' inflow condition, since the random-fluctuations enforced at the inlet are unphysical and damped out quickly.

- **Paper 3**

  Wang P., Bai X.S. Large eddy simulation of turbulent premixed flames using level-set G-equation. Proceedings of the Combustion Institute, vol. 30: 583–591, 2004.

  Level-set *G*-equation and stationary flamelet chemistry are used in large eddy simulation (LES) of a propane/air premixed turbulent flame stabilized by a bluff body. The aim was to study the interaction between the flame front and turbulent eddies, and in particular to examine the effect of sub-grid scale (SGS) eddies on the wrinkling of the flame surface. The results indicated that the two types of turbulence eddies, the resolved large scale eddies and the unresolved SGS eddies, have different effects on the flame. The fluctuation of the flame surface, which is responsible for the broadening of the time averaged mean flame brush by turbulence, depends on the large resolved turbulence eddies. Time averaged mean flow velocity, temperature and major species concentrations mainly depend on the large scale resolved eddies. The unresolved SGS eddies contribute to the wrinkling at the SGS level and play an important role in the enhancement of the propagation speed of the resolved flame front. In addition, the spatially filtered intermediate species such as radicals and the spatially filtered reaction rates strongly depend on the small SGS eddies. The asymptotic behavior of flame wrinkling by the SGS eddies, with respect to the decrease in filter size and grid size, is investigated further using a simplified level-set equation, *h*-equation, in a model shear flow. It was shown that to minimize the influence of the SGS eddies on the flame wrinkles, rather fine grid and filter size may have to be used.

- **Paper 4**

  Wang P., Bai X.S. Large eddy simulation of premixed turbulent flames by G-equation. Proceedings of the Third Mediterranean Combustion Symposium, Marrakech, Morocco, pages: 951–959, June 8–13, 2003.

A Flamelet Library approach and a level-set *G*-equation are used to model the premixed turbulent combustion in the large eddy simulation (LES) framework. The resolved flame front is modeled using an iso-surface of the scalar *G* field, which is computed using the *G*-equation and the distance function equation. Some aspects about the implementation of the level-set *G*-equation are addressed. An explicit top-hat filter has been applied to the density for smoothing its change with time; thereby remove the pseudo pressure jump across the flame front. To validate the numerical scheme, detailed comparisons between the experimental and computational results on an afterburner configuration are presented. The overall agreement is promising: the mean flame position, the velocity and the major species concentrations are in reasonable agreement. LES successfully predicted the fluctuations of the flame front. The minor species CO is very sensitive to the unsolved sub-scale wrinkling, for which an appropriate sub-scale wrinkling model is needed.

- **Paper 5**

  Bai X.S., Wang P. Large eddy simulation of flame wrinkling in turbulent premixed combustion. Proceedings of the Joint Meeting of Scandinavian–Nordic and Italian Sections of the Combustion Institute, Ischia, Italy, No. 2.13, September 18–21, 2003.

This work investigates the flame wrinkling based on the level set *G*-equation. In LES the unsteady motion of the large-scale eddies down to the inertial sub-range scales are calculated directly. It is shown that turbulence and the flame surface is closely interacting each other, and the flame surface shape follows closely the shape of the wake vortex shedding. The flame has a significant impact on the turbulence flowfield. On the unburnt side, turbulence eddies are much finer, whereas on the burnt side, turbulence eddies are large. Although the resolved eddies scales are rich, the wrinkle size of them is mainly close to the integral length, and the smaller scale wrinkling is not captured. A possible cause of this may be the lack of response of flame front to small disturbance.

9.2 Proposal for future work

In this thesis work, LES method has been used to study the turbulent swirling flows and the turbulent lean-premixed combustion, in which the turbulent premixed combustion is modeled based on the level set *G*-equation approach. Some proposals for future work may be drawn below.

- The rescaled inflow library condition needs to be improved further. In Figure 6.6, it is shown that the turbulent kinetic energy, obtained by the rescaled inflow library condition, decreases a little near the inlet, though it is much smaller than that of the random-fluctuation condition. A possible way to improve the rescaled inflow library condition's performance is to enforce two or more inflow sections at the inlet. In this way, the spatial structure of turbulence may be retained in some degree.
- More simulations should be done on the lean premixed combustion with swirling flow, since the swirling flow is widely used in various combustors. To do this, both qualitative and quantitative experimental data are needed.
- In this thesis work, the used flamelet library is time steady, which did not account for the history effect. It is expected that the prediction accuracy may be enhanced with an unsteady flamelet library.
- A better performance model for estimation of the subgrid burning speed s_{LES} is wanted. One way is to determine the model coefficient in formulation (4.6) with a dynamic procedure as done in Kim and Menon (2000), Im (1995), Im et al. (1997).

Reference

Adalsteinsson D., Sethian J.A. (1999). The fast construction of extension velocities in level set methods. *J. of Computational Physics* 148:2–22.

Ahmed S.A. (1998). Velocity measurements and turbulence statistics of a confined isothermal swirling flow. *Experimental Thermal and Fluid Science* 17: 256–264.

Akselvoll K., Moin P. (1996). Large-eddy simulation of turbulent confined coannular jets. *J. of Fluid Mechanics* 315: 387–411.

Bahr D.W. (1999). Gas turbine combustion and emission abatement technology current and projected status. *Proceedings of the International Gas Turbine Congress*, November 14–19, Kobe, Japan.

Bai X.S., Fuchs L. (1994). Modeling of turbulent reacting flows past a bluff body: assessment of accuracy and efficiency. *Computers Fluids* 23: 507–521.

Baldwin B.S., Lomax H. (1978). Thin-layer approximation and algebraic model for separated turbulent flows. *AIAA paper* 78–257.

Baldwin B.S., Barth T.J. (1990). A one-equation turbulence transport model for high Reynolds number wall-bounded flows. *NASA TM*–102847 (see also *AIAA paper* 91–0610).

Bardina J., Ferziger J.H., Reynolds W.C. (1980). Improved subgrid model for large-eddy simulation. *AIAA paper* 80–1357.

Barth T.J., Sethian J.A. (1998). Numerical schemes for the Hamilton–Jacobi and level set equations on triangulated domains. *J. of Computational Physics* 145: 1–40.

Baum M., Poinsot T.J., Haworth D.C., Darabiha N. (1994). Using direct numerical simulation to study H2/O2/N2 flames with complex chemistry in turbulent flows. *J. of Fluid Mechanics* 281:1–32.

Bengtsson P.E., Andersson S. (2002). *Material from the CECOST–course: Combustion Science*, August.

Bilger R.W. (1993). Conditional moment closure for turbulent reaction flows. *Physics of Fluids A* 5: 434–444.

Billant P., Chomaz J.M., Huerre P. (1998). Experimental study of vortex breakdown in swirling jets. *J. of Fluid Mechanics* 376: 183–219.

Boger M., Veynante D., Boughanem H., Trouvé A. (1998). Direct numerical simulation analysis of flame surface density concept for large eddy simulation of turbulent premixed combustion. *Proceedings of the Combustion Institute*, vol. 27: 917–925.

Borghi R. (1988). Turbulent combustion modeling. *Progress in Energy and Combustion Science* 14: 245–292.

Bourlioux A. (2000). Semi-analytical validation of a dynamic large-eddy simulation procedure for turbulent premixed flames via the *G*-equation. *Combustion Theory and Modelling* 4: 363–389.

Bradley D. (1992). How fast can we burn? *Proceedings of the Combustion Institute*, vol. 24: 247–262.

Brandt A. (1977). Multi-level adaptive solution to boundary value problems. *Mathematics of Computation* 31: 333-390.

Bray K.N.C. (1996). The challenge of turbulent combustion. *Proceedings of the Combustion Institute*, vol. 26: 1–26.

Bray K.N.C., Moss J.B. (1977). A unified statistical model of the premixed turbulent flame. *Acta Astronautica* 4: 291–319.

Bray K.N.C., Libby P.A., Masuya G., Moss J.B. (1981). Turbulence production on premixed turbulent flames. *Combustion Science and Technology* 25: 127–140.

Bray K.N.C., Libby P.A., Moss J.B. (1985). Unified Modeling Approach for Premixed Turbulent Combustion–Part 1: General Formulation. *Combustion and Flame* 61: 87–102.

Brewster B.S., Cannon S.M., Farmer J.R., Meng F. (1999). Modeling of lean premixed combustion in stationary gas turbuines. *Progress in Energy and Combustion Science* 25: 353–385.

Bui-Pham M., Seshadri K., Williams F.A. (1992). The asymptotic structure of premixed methane-air flames with slow CO oxidation. *Combustion and Flame* 89: 343–362.

Buschmann A., Dinkelacker F., Schäfer T., Schäfer M., Wolfrum J. (1996). Measurement of the instantaneous detailed flame structure in turbulent premixed combustion. *Proceedings of the Combustion Institute*, vol. 26: 437–445.

Butler T.D., O'Rourke P.J. (1977). A numerical method for two-dimensional unsteady reacting flows. *Proceedings of the Combustion Institute*, vol. 16: 1503–1515.

Candel S., Veynante D., Lacas F., Darabiha N., Rolon C. (1994). Current progress and future trends in turbulent combustion. *Combustion Science and Technology* 98: 245–264.

Candel S., Thévenin D., Darabiha N., Veynante D. (1999). Progress in numerical combustion. *Combustion Science and Technology* 149: 297–337.

Carati D., Winckelmans G.S., Jeanmart H. (2001). On the modeling of subgrid-scale and filtered-scale stress tensors in large eddy simulation. *J. of Fluid Mechanics* 441: 119–138.

Cassidy J.J., Falvey H.T. (1970). Observations of unsteady flow arising after vortex breakdown. *J. of Fluid Mechanics* 41: 727–736.

Champagne F.H., Kromat S. (2000). Experiments on the formation of a recirculation zone in swirling coaxial jets. *Experiments in Fluids* 29: 494–504.

Chanaud R.C. (1965). Observations of oscillatory motion in certain swirling flows. *J. of Fluid Mechanics* 21: 111–127.

Chen M., Herrmann M., Peters N. (2000). Flamelet modeling of lifted turbulent methane/air and propane/air jet diffusion flames. *Proceedings of the Combustion Institute*, vol. 28: 167–174.

Chen Y.C., Mansour Mohy S. (1997). Simultaneous Rayleigh scattering and laser-induced CH fluorescence for reaction zone imaging in high-speed premixed hydrocarbon flames. *Applied Physics B* 64: 599–605.

Chopp D.L. (1993). Computing minimal surfaces via level set curvature flow. *J. of Computational Physics* 106:77–91.

Chow F.K., Moin P. (2003). A further study of numerical errors in large eddy simulations. *J. of Computational Physics* 184: 366–380.

Clavin P., Williams F.A. (1982). Effects of molecular diffusion and of thermal expansion on the structure and dynamics of premixed flames in turbulent flows of large scale and low intensity. *J. of Fluid Mechanics* 116: 251–282.

Coats C.M. (1996). Coherent structures in combustion. *Progress in Energy and Combustion Science* 22: 427–509.

Colin O., Ducros F., Veynante D., Poinsot T. (2000). A thickened flame model for large eddy simulation of turbulent premixed combustion. *Physics of Fluids* 12(7): 1843–1863.

Crandall M.G., Lions P.L. (1983). Viscosity solutions of Hamilton–Jacobi equations. *Transactions of the American Mathematical Society* 277: 1–42.

Damköhler G. (1940). Der Einfluß der Turbulenz auf die Flammengeschwindigkeit in Gasgemischen. *Z. Elektrochem.* 46: 601–652. (English translation NASA Tech. Mem. 1112, 1947).

Denet B. (1998). Are small scales of turbulence able to wrinkle a premixed flame at large scale? *Combustion Theory and Modelling* 2: 167–178.

Dijkstra E.W. (1959). A note on two problems in connection with graphs. *Numerische Mathematik* 1: 269–271.

Domingo P., Vervisch L. (1996). Triple flames and partially premixed combustion in autoignition of non-premixed turbulent mixtures. *Proceedings of the Combustion Institute*, vol. 26: 233–240.

Duchamp de Lageneste L., Pitsch H. (2000). A level-set approach to large eddy simulations of premixed turbulent combustion. *Annual Research Briefs,* Center for Turbulence Research, 105–116.

Duchamp de Lageneste L., Pitsch H. (2001). Progress in large-eddy simulation of premixed and partially-premixed turbulent combustion. *Annual Research Briefs,* Center for Turbulence Research, 97–107.

Duchamp de Lageneste L., Pitsch H. (2002). A numerical scheme for the large-eddy simulation of turbulent combustion using a level-set method. *Annual Research Briefs,* Center for Turbulence Research, 15–26.

Fernandez-Feria R., Ortega-Casanova J. (1999). Inviscid vortex breakdown models in pipes. *Mathematics and Physics* 50: 698–730.

Flohr P., Pitsch H. (2000). A turbulent flame speed closure model for LES of industrial burner flows. *Proceedings of the summer program*, Center for Turbulence Research, 169–179.

Fureby C. (2000). Large eddy simulation of combustion instabilities in a jet engine afterburner model. *Combustion Science and Technology* 161: 213–243.

Fureby C., Grinstein F.F. (2002). Large eddy simulation of high Reynolds number free and wall-bounded flows. *J. of Computational Physics* 181: 68–97.

Gabrielsson R., Hermann F. (2002). Gas turbines. *Material from the CECOST-course: Combustion Devices*, Autumn.

Germano M., Piomelli U., Moin P., Cabot W.H. (1991). A dynamic subgrid-scale eddy viscosity model. *Physics of Fluids* 3(7): 1760–1765.

Ghosal S., Moin P. (1995). The basic equations for the large eddy simulation of turbulent flows in complex geometry. *J. of Computational Physics* 118: 24–37.

Glassman I. (1996). Combustion. Third edition, Academic press.

Gottlieb S., Shu C.W. (1998). Total variation diminishing Runge–Kutta schemes. *Mathematics of Computation* 67(221): 73–85.

Gouldin F.G., Halthore R.N., Vu B.T. (1984). Periodic oscillations observed in swriling flows with and without combustion. *Proceedings of the Combustion Institute*, vol. 20: 269–276.

Grinstein F.F., Young T.R., Gutmark E.J., Li G., Hsiao G., Mongia H.C. (2002). Flow dynamics in a swirl combustor. *J. of Turbulence* 3 (030).

Gullbrand J., Bai X.S., Fuchs L. (2001). High-order cartesian grid method for calculation of incompressible turbulent flows. *Int. J. for Numerical Methods in Fluids* 36: 687–709.

Gullbrand J., Chow F.K. (2003). The effect of numerical errors and turbulence models in LES of channel flow, with and without explicit filtering. *J. of Fluid Mechanics* 495: 323–341.

Gupta A.K., Lilley D.G., Syred N. (1984). Swirl flows. Abacus press.

Harten A., Engquist B., Osher S., Chakravarthy S. (1987). Uniformaly high-order accurate essentially non-oscillatory schemes Ⅲ . *J. of Computational Physics* 71: 231–303.

Harvey J.K. (1962). Some observations of the vortex breakdown phenomenon. *J. of Fluid Mechanics* 14: 585–592.

Hawkes E.R., Cant R.S. (2000). A flame surface density approach to large eddy simulation of premixed turbulent combustion. *Proceedings of the Combustion Institute*, vol. 28: 51–58.

Hawkes E.R., Cant R.S. (2001). Implications of a flame surface density approach to large eddy simulation of premixed turbulent combustion. *Combustion and Flame* 126: 1617–1629.

Hilbert R., Tap F., El-Rabii H., Thévenin D. (2004). Impact of detailed chemistry and transport models on turbulent combustion simulations. *Progress in Energy and Combustion Science* 30: 61–117.

Hou T.Y., Li Z., Osher S., Zhao H.K. (1997). A hybrid method for moving interface problems with application to the Hele–Shaw Flow. *J. of Computational Physics* 134: 236–252.

Huang R.F., Tsai F.C. (2001). Flow field characteristics of swirling double concentric jets. *Experimental Thermal and Fluid Science* 25: 151–161.

Hult J., Josefsson G., Aldén M., Kaminski C.F. (2000). Flame front tracking and simultaneous flow field visualization in turbulent combustion. Proceedings of the 10th International Symposium on Applications of Laser Techniques to Fluid Mechanics, No. 26-2, Lisbon.

Im H.G. (1995). Study of turbulent premixed flame propagation using a laminar flamelet model. *Annual Research Briefs,* Center for Turbulence Research, 347–360.

Im H.G., Lund T.S., Ferziger J.H. (1997). Large eddy simulation of turbulent front propagation with dynamic subgrid models. *Physics of Fluids* 9(12): 3826-3833.

Jakirlic S., Volkert J., Pascal H., Hanjalic K., Tropea C. (2000). DNS, experimental and modeling study of axially compressed in-cylinder swirling flow. *Int. J. of Heat and Fluid Flows* 21: 627–639.

Jenkins K.W., Cant R.S. (2002). Curvature effects on flame kernels in a turbulent environment. *Proceedings of the Combustion Institute*, vol. 29: 2023–2029.

Jiang G.S., Shu C.W. (1996). Efficient implementation of weighted ENO schemes. *J. of Computational Physics* 126: 202–228.

Jiang G.S., Peng D.P. (2000). Weighted ENO schemes for Hamilton–Jacobi equations. *SIAM Journal on Scientific computing* 21(6): 2126–2143.

Johansson A.V., Wallin S. (1996). A new explicit algebraic Reynolds sress model. *Proceedings of the Sixth European Turbulence Conference*, Lausanne, July, Kluwer, pp. 31–34.

Jones W.P., Launder B.E. (1972). The prediction of laminarization with a two-equation model of turbulence. *Int. J. of Heat and Mass Transfer* 15: 301–314.

Jones W.P., Whitelaw J.H. (1982). Calculation methods for reacting turbulent flows: A review. *Combustion and Flame* 48: 1–26.

Jones W.P., Lindstedt R.P. (1988). Global reaction schemes for hydrocarbon combustion. *Combustion and Flame* 73: 233–249.

Jones W.P., Prasetyo Y. (1996). Probability density function modeling of premixed turbulent opposed jet flames. *Proceedings of the Combustion Institute*, vol. 26: 275–282.

Just T. (1994). Multichanner reactions in combustion. *Proceedings of the Combustion Institute*, vol. 25: 687–704.

Kaminski C.F., Bai X.S., Hult J., Dreizler A., Fuchs L. (2000a). Flame growth and wrinkling in a turbulent flow. *Applied Physics B* (*Lasers and Optics*) 71: 711–716.

Kaminski C.F., Hult J., Aldén M. et al. (2000b). Spark ignition of turbulent methane/air mixtures revealed by time-resolved planar laser-induced fluorescence and direct numerical simulations. *Proceedings of the Combustion Institute*, vol. 28: 399–405.

Karpov V., Lipatnikov A., Zimont V. (1996). A test of an engineering model of premixed turbulent combustion. *Proceedings of the Combustion Institute*, vol. 26: 249–257.

Katopodes F.V., Street R.L., Ferziger J.H. (2000). A theory for the subfilter-scale model in large-eddy simulation. *Environmental Fluid Mechanics Laboratory, Stanford, Technical Report* 2000–K1.

Kawamura T., Kuwahara K. (1984). Computation of high Reynolds number flow around a circular cylinder with surface roughness. *AIAA paper* 84–0340.

Kerstein A.R., Ashurst W.T. (1988). Field equation for interface propagation in an unsteady homogeneous flow field. *Physical reviews A* 37(7): 2728–2731.

Kim W.W., Menon S., Mongia H.C. (1999). Large-eddy simulation of a gas turbine combustor flow. *Combustion Science and Technology* 143: 25–62.

Kim W.W., Menon S. (2000). Numerical modeling of turbulent premixed flames in the thin-reaction-zones regime. *Combustion Science and Technology* 160: 113–150.

Kitoh O. (1991). Experimental study of turbulent swirling flow in a straight pipe. *J. of Fluid Mechanics* 225: 445–479.

Klein M., Sadiki A., Janicka J. (2003). A digital filter based generation of inflow data for spatially developing direct numerical or large eddy simulations. *J. of Computational Physics* 186: 652–665.

Klimenko A.Y. (1990). Multicomponent diffusion of various scalars in turbulent flows. *Fluid Dynamics* 25: 327–334.

Knikker R., Veynante D., Rolon J.C., Meneveau C. (2000). Planar Laser Induced Fluorescence in a turbulent premixed flame to analyze large eddy simulation models. *Proceedings of the 10th international symposium on turbulence, heat and mass transfer*, Lisbon, Portugal.

Kohse-Höinghaus K., Barlow R.S., Aldén M., Wolfrum J. (2004). Combustion at the focus: laser diagnostics and control. 50th anniversary lecture on 30th International Symposium on Combustion. *Proceedings of the Combustion Institute*, vol. 30, in press.

Kolmogorov A.N. (1941). Local structure of turbulence in incompressible viscous fluid for very large Reynolds number. *Doklady AN. SSSR*, vol.30: 299-303.

Kolmogorov A.N. (1942). Equations of turbulent motion of an incompressible fluid. *Izvestia Academy of Sciences, USSR; Physics*, vol. 6, no. 1 and 2, pp. 56-58.

Kubo I., Gouldin F.G. (1975). Numerical calculations of turbulent swirling flow. *Transactions of ASME J. of Fluids Engineering* 97: 310–315.

Launder B.E., Spalding D.B. (1972). Mathematical models of turbulence. Academic Press, London.

Launder B.E., Sharma B.I. (1974). Application of the energy dissipation model of turbulence to the calculation of flow near a spinning disc. *Letters in Heat and Mass Transfer*, vol. 1, no. 2, pp. 131–138.

Launder B.E., Reece G.J., Rodi W. (1975). Progress in the development of a Reynolds stress turbulence closure. *J. of Fluid Mechanics* 68: 537–566.

Law C.K., Sung C.J. (2000). Structure, aerodynamics and geometry of premixed flamelets. *Progress in Energy and Combustion Science* 26: 459–505.

Leckner B. (2002). Boilers and furnaces (version 3). *Material from the CECOST-course: Combustion Devices*, Autumn.

Lefebvre A.H. (1995). The role of fuel preparation in low-emission combustion. *Transactions of ASME J. of Engineering for Gas Turbines and Power* 117: 617–654.

Lesieur M., Métais O. (1996). New trends in large-eddy simulations of turbulence. *Annual Review of Fluid Mechanics* 28: 45–82.

Levy D., Puppo G., Russo G. (2002). A fourth-order central WENO scheme for multidimensional hyperbolic systems of conservation laws. *SIAM J. on Scientific Computing* 24(2): 480–506.

Lipatnikov N., Chomiak J. (2002). Turbulent flame speed and thickness: phenomenology, evaluation, and application in multi-dimensional simulations. *Progress in Energy and Combustion Science* 28: 1–74.

Liu S., Meneveau C., Katz J. (1994). On the properties of similarity subgrid scale models as deduced from measurements in a turbulent jet. *J. of Fluid Mechanics* 275: 83–119.

Liu X.D., Osher S., Chan T. (1994). Weighted essentially non-oscillatory schemes. *J. of Computational Physics* 115: 200–212.

Lopez J.M. (1994). On the bifurcation structure of axisymmetric vortex breakdown in a constricted pipe. *Physics of Fluids* 6(11): 3683–3693.

Lu P., Semião V. (2004). A new second-moment closure approach for turbulent swirling confined flows. *Int. J. for Numerical Methods in Fluids* 41: 133–150.

Lucca-Negro O, O'Doherty T. (2001). Vortex breakdown: a review. *Progress in Energy and Combustion Science* 27: 431–481.

Lund T.S., Wu X., Squires K.D. (1998). Generation of turbulent inflow data for spatially-developing boundary layer simulations. *J. of Computational Physics* 140: 233–258.

Løvås T., Nilsson D., Mauss F. (2000). Automatic recuction procedure for chemical mechanisms applied to premixed methane-air flame. *Proceedings of the Combustion Institute*, vol. 28: 1809–1815.

Løvås T., Mauss F., Hasse C., Peters N. (2002). Development of adaptive kinetics for application in combustion systems. *Proceedings of the Combustion Institute*, vol. 29: 1403–1410.

Magnussen B.F., Hjertager B.H. (1977). On mathematical models of turbulent combustion with special emphasis on soot formation and combustion. *Proceedings of the Combustion Institute*, vol. 16: 719–729.

Margolin L.G., Smolarkiewicz P.K., Wyszogrodzki A.A. (2002). Implicit turbulent modeling for high Reynolds number flows. *Transactions of ASME J. of Fluids Engineering* 124: 862–867.

Markstein G.H. (1964). Nonsteady flame propagation. Pergammon press, NewYork.

Matalon M., Matkowsky B.J. (1982). Flames as gasdynamic discontinuities. *J. of Fluid Mechanics* 124: 239–259.

Mathieu J., Scott J. (2000). An introduction to turbulent flow. Cambridge University Press.

Mauss F., Peters N. (1993a). Reduced kinetic mechanisms for premixed methane–air flames. *In N. Peters and B. Rogg, editors, Reduced Kinetic Mechanisms for Applications in Combustion Systems, Lecture Notes in Physics*, m15, 58–75, Springer-Verlag, Berlin.

Mauss F., Peters N., Rogg B., Williams F.A. (1993b). Reduced kinetic mechanisms for premixed hydrogen flames. *In N. Peters and B. Rogg, editors, Reduced Kinetic Mechanisms for Applications in Combustion Systems, Lecture Notes in Physics*, m15, 29–43, Springer-Verlag, Berlin.

Mauss F. (1998). Entwicklung eines kinetischen Modells der Russbildung mit schneller Polymerisation. *Ph.D. thesis*, Rheinisch–Westfhlishe Technische Hochschule, Aachen, Germany.

Mehta R.D., Wood D.H., Clausen P.D. (1991). Some effects of swirl on turbulent mixing layer development. *Physics of Fluids A* 3(11): 2716–2724.

Moin P., Squires K., Cabot W., Lee S. (1991). A dynamic subgrid-scale model for compressible turbulence and scalar transport. *Physics of Fluids A* 3(11): 2746–2757.

Meneveau C., Kata J. (2000). Scale-invariance and turbulence models for large-eddy simulation. *Annual Review of Fluid Mechanics* 32: 1–32.

Mueller C.J., Driscoll J.F., Reuss D.L., Drake M.C. (1996). Effect of unsteady stretch on the length of a freely propagating flame wrinkled by a vortex. *Proceedings of the Combustion Institute*, vol. 26: 347–355.

Nejad A.S., Vanka S.P., Favaloro S.C. (1989). Application of laser velocimetry for characterization of confined swirling flow. *J. of Engineering for Gas Turbines and Power* 111: 36–45.

Nilsson P. (2001). A level-set flamelet library model for premixed turbulent combustion. *Ph.D. dissertation*, Department of Heat and Power Engineering, Lund Institute of Technology, Sweden.

Nilsson P., Bai X.S. (2000). Level-set flamelet library approach for premixed turbulent combustion. *Experimental Thermal and Fluid Science* 21: 87–98.

Nilsson P., Bai X. S. (2002). Effects of flame stretch and wrinkling on co formation in turbulent premixed combustion. *Proceedings of the Combustion Institute*, vol. 29: 1873–1879.

Nilsson P., Bai X.S. (2003). PDF of distance function for level-set flamelet library modelling. *Int. J. for Numerical Methods in Fluids* 41: 653–673.

Nygren J., Hult J. Richter M., Aldén M. et al. (2002). Three-dimensional laser induced fluorescence of fuel distributions in an HCCI engine. *Proceedings of the Combustion Institute*, vol. 29: 679–685.

Oberlack M., Wenzel H., Peters N. (2001). On symmetries and averaging of the *G*-equation for premixed combustion. *Combustion Theory and Modelling* 5: 363–383.

Olsson M., Fuchs L. (1998). large eddy simulation of a forced semi-confined circular impinging jet. *Physics of Fluids* 10: 476–486.

Osher S., Sethian J.A. (1988). Fronts propagating with curvature dependent speed: algorithms based on Hamilton–Jacobi formulations. *J. of Computational Physics* 79: 12–49.

Osher S., Shu C.W. (1991). High-order essentially non-oscillatory schemes for Hamilton–Jacobi equations. *SIAM Journal on Numerical Analysis* 28: 907–922.

Panda J., Mclaughlin D.K. (1994). Experiments on the instabilities of a swirling jet. *Physics of Fluids* 6: 263–276.

Paschereit C.O., Gutmark E., Weisenstein W. (1999). Coherent structures in swirling flows and their role in acoustic combustion control. *Physics of Fluids* 11: 2667–2678.

Patankar S.V. (1980). Numerical heat transfer and fluid flow. Hemisphere publishing corporation.

Pauley L.L., Moin P., Reynolds W.C. (1990). The structure of two-dimensional separation. *J. of Fluid Mechanics* 220: 397–411.

Peng D.P., Merriman B., Osher S., Zhao H.K., Kang M. (1999). A PDE-based fast local level set method. *J. of Computational Physics* 155: 410–438.

Peters N. (1985). Numerical and asymptotic analysis of systematically reduced reaction schemes for hydrocarbon flames. Numerical simulation of combustion phenomena. *Lecture Notes in Physics*, 241, 90–109, Springer-verlag, Berlin.

Peters N. (1993). Falme Calculations with Reduced Mechanisms – An Outline. *In N. Peters and B. Rogg, editors, Reduced Kinetic Mechanisms for Applications in Combustion Systems, Lecture Notes in Physics*, m15, 3-14, Springer-Verlag, Berlin.

Peters N. (1999). The turbulent burning velocity for large-scale and small-scale turbulence. *J. of Fluid Mechanics* 384: 107–132.

Peters N.(2000). Turbulent combustion. Cambridge university press.

Peters N., Williams F.A. (1987). The asymptotic structure of stoichiometric methane-air flames. *Combustion and Flame* 68: 185–207.

Pierce C.D., Moin P. (1998a). Method for generating equilibrium swirling inflow conditions. *AIAA J.* 36: 1325–1327.

Pierce C.D., Moin P. (1998b). Large eddy simulation of a confined coaxial jet with swirl and heat release. *AIAA 98–2892*, 29th AIAA Fluid Dynamics Conference, June 15–18.

Pierce C.D. (2001). Progress-variable approach for large eddy simulation of turbulent combustion. *Ph. D. Dissertation*, Stanford University, USA.

Piomelli U. (1999). Large-eddy simulation: achievements and challenges. *Progress in Aerospace Sciences* 35: 335–362.

Pitsch H. (2002). A *G*-equation formulation for large-eddy simulation of premixed turbulent combustion. *Annual Research Briefs,* Center for Turbulence Research, 3–14.

Pitsch H., Steiner H. (2000). Large-eddy simulation of a turbulent piloted methane/air diffusion flame (Sandia flame D). *Physics of Fluids* 12(10): 2541–2554.

Pitsch H., Duchamp de Lageneste L. (2002). Large-eddy simulation of premixed turbulent combustion using a level-set approach. *Proceedings of the Combustion Institute*, vol. 29: 2001–2008.

Poinsot T., Veynante D., Veynante D. (1990). Diagrams of premixed turbulent combustion based on direct simulation. *Proceedings of the Combustion Institute*, vol. 23: 613–619.

Poinsot T., Veynante D., Candel S. (1991). Quenching Process and Premixed Combustion Diagrams. *J. of Fluid Mechanics* 228: 561–606.

Poinsot T., Veynante D., Trouvé A. (1996). Applications of direct numerical simulation to premixed turbulent combustion. *Progress in Energy Combustion Science* 21: 531–576.

Poinsot T., Veynante D. (2001). Theoretical and Numerical Combustion. Edwards Inc.

Pope S.B. (1985). Pdf methods for turbulent reactive flows. *Progress in Energy Combustion Science* 11: 119–192.

Prandtl L. (1925). Über die ausgebildete turbulenz. *ZAMM*, vol. 5: 136–139.

Qian J., Tryggvason G., Law C.K. (1998). A front tracking method for the motion of premixed flames. *J. of Computational Physics* 144: 52–69.

Ribeiro M.M., Whitelaw J.H. (1980). Co-axial jets with and without swirl. *J. of Fluid Mechanics* 96: 769–795.

Rodi W. (1976). A new algebraic stress relation for calculation the Reynolds stresses. *ZAMM* 56: 219–221.

Russo G., Smereka P. (2000). A remark on computing distance functions. *J. of Computational Physics* 163: 51–67.

Sankaran V., Menon S. (2000). Structure of premixed turbulent flames in the thin-reaction-zones regime. *Proceedings of the Combustion Institute*, vol. 28: 203–209.

Schmittel P., Gunther B., Lenze B., Leuchel W., Bochhorn H. (2000). Turbulent swirling flames: experimental investigation of the flowfield and formation of nitrogen oxide. *Proceedings of the Combustion Institute*, vol. 28: 303–309.

Schwer D.A., Lu P., Green W.H. (2003). An adaptive chemistry approach to modeling complex kinetics in reacting flows. *Combustion and Flame* 133: 451–465.

Seinfeld, J. H. (1986). Atmospheric Chemistry and physics of Air Pollution. John Wiley & Sons, New York.

Serre E., Bontoux P. (2002). Vortex breakdown in a three-dimensional swirling flow. *J. of Fluid Mechanics* 459: 347–370.

Seshadri K. (1996). Multistep asymptotic analyses of flame structure. *Proceedings of the Combustion Institute*, vol. 26: 831–846.

Seshadri K., Peters N. (1990). The inner structure of methane-air flames. *Combustion and Flame* 81: 96–118.

Sethian J.A., Strain J.D. (1992). Crystal Growth and Dendritic Solidification. *J. of Computational Physics* 98: 231–253.

Sethian J.A. (2001). Evolution, Implementation, and Application of level set and fast marching methods for advancing fronts. *J. of Computational Physics* 169: 503–555.

Sethian J.A., Smereka P. (2003). Level set methods for fluid interfaces. *Annual Review of Fluid Mechanics* 35: 341–372.

Sharif M.A.R., Wong Y.K.E. (1995). Evaluation of the performance of three turbulence closure models in the prediction of confined swirling flows. *Computers & Fluids* 24: 81–100.

Shepherd I.G., Moss J.B., Bray K.N.C. (1982). Turbulent transport in a confined premixed flame. *Proceedings of the Combustion Institute*, vol. 19: 423–431.

Shepherd I.G., Cheng R.K., Plessing T., Kortschik C., Peters N. (2002). Premixed flame front structure in intense turbulence. *Proceedings of the Combustion Institute*, vol. 29: 1833–1840.

Shinjo J., Mizobuchi Y., Ogawa S. (2003). LES of unstable combustion in a gas turbine combustor. *Proceedings of the 5th International Symposium on High Performance Computing*, ISHPC, Japan, 234–244.

Shu C.W., Osher S. (1988). Efficient implementation of essentially non-oscillatory shock-capturing schemes. *J. of Computational Physics* 77: 439–471.

Shu C.W. (1997). Essentially Non-Oscillatory and Weighted Essentially Non-Oscillatory Schemes for Hyperbolic Conservation Laws. NASA/CR–97–206253.

Sivashinsky G.I. (1977). Diffusional-thermal theory of cellular flames. *Combustion Science and Technology* 15: 137–146.

Sjunnesson A., Olovsson S., Sjöblom B. (1991). Validation rig – a tool for flame studies. *Internal Report VFA 9370–308*, Volvo Flygmotor, Sweden.

Smagorinsky J. (1963). General circulation experiments with the primitive equations. *Monthly Weather Review* 91: 99–152.

Smiljanovski V., Moser V., Klein R. (1997). A capturing-tracking hybrid scheme for deflagration discontinuities. *Combustion Theory and Modelling* 1: 183–215.

Smith A.M.O., Cebeci T. (1967). Numerical solution of the turbulent boundary–layer equations. *Douglas Aircraft Division Report, DAC* 33735.

Spalart P.R. (1988). Direct numerical simulations of a turbulent boundary layer up to $Re_\theta=1410$. *J. of Fluid Mechanics* 187: 61–98.

Spalart P.R., Allmaras S.R. (1992). A one-equation turbulence model for aerodynamic flows. *AIAA paper* 92–439.

Spalding D.B. (1971). Mixing and chemical reaction in steady confined turbulent flames. *Proceedings of the Combustion Institute*, vol. 13: 649–657.

Speziale C.G., Abid R., Anderson E.C. (1990). A critical evaluation of two-equation models ofr near wall turbulence. *AIAA paper* 90–1481.

Strain J. (1999). Fast tree-based redistancing for level set computations. *J. of Computational Physics* 152: 664–686.

Strand T. (2002). Gas turbine combustion devices. *Material from the CECOST-course: Combustion Devices*, Autumn.

Sussman M., Smereka P., Osher S. (1994). A level set approach for computing solutions to incompressible two-phase flow. *J. of Computational Physics* 114: 146–159.

Sussman M., Fatemi E. (1999). An efficient, interface-preserving level set redistancing algorithm and its application to interfacial incompressible fluid flows. *SIAM J. on Scientific Computing* 20(4): 1165–1191.

Takahira H., Horiuchi T. (2003). An improved three dimensional level set method for gas-liquid two-phase flows. *The 8th international symposium on gas-liquid two-phase flows*. July 6–10, Honolulu, Hawaii, USA.

Tanahashi M., Nada Y., Ito Y., Miyauchi T. (2002). Local flame structure in the well-stirred reactor regime. *Proceedings of the Combustion Institute*, vol. 29: 2041–2049.

Tennekes H., Lumley J.L. (1990). A first course in turbulence, 13th printing. The Massachusetts institute of technology press, London, England.

Thévenin D., Gicquel O., Charentenay J.D., Hilbert R., Veynante D. (2002). Two- versus three-dimensional direct simulations of turbulent methane flame kernels using realistic chemistry. *Proceedings of the Combustion Institute*, vol. 29: 2031–2039.

Tryggvason G., Bunner B., Esmaeeli A. et al. (2001). A front tracking method for the computations of multiphase flow. *J. of Computational Physics* 169: 708–759.

Tsai R. (2002). Rapid and accurate computation of the distance function using grids. *J. of Computational Physics* 178: 175–195.

Tsai R., Osher S. (2003). Review article: Level set methods and their applications in image science. *Communications in Mathematical Sciences* 1(4): 623–656.

Tsitsiklis J.N. (1995). Efficient algorithms for globally optimal trajectories. *IEEE Transaction Automatic Control* 40: 1528–1538.

Turns S.R. (2000). An introduction to combustion: concepts and applications. McGraw–Hill International Editions.

Udaykumar H.S., Kan H.C., Shyy W., Tran-Son-Tay R. (1997). Multiphase dynamics in arbitrary geometries on fixed Cartesian grids. *J. of Computational Physics* 137: 366–405.

Vervisch L., Bidaux E., Bray K.N.C., Lollmann W. (1995). Surface density function in premixed turbulent combusiontmodeling, similarities between probability density function and flame surface approaches. *Physics of Fluids A* 2496–2503.

Vervisch L., Poinsot T. (1998). Direct numerical simulation of non-premixed turbulent flames. *Annual Review of Fluid Mechanic* 30: 655–691.

Vervisch L., Veynante D. (2000). Interlinks between approaches for modeling turbulent flames. *Proceedings of the Combustion Institute*, vol. 28: 175–183.

Veynante D., Vervisch L. (2002). Turbulent combustion modeling. *Progress in Energy and Combustion Science* 28: 193–266.

Wallin S., Johansson A.V. (2000). An explicit algebraic Reynolds stress model for incompressible and compressible turbulent flows. *J. of Fluid Mechanics* 403: 89–132.

Wang P., Bai X.S., Wessman M., Klingmann J. (2004a). Large eddy simulation and experimental studies of a confined turbulent swirling flow. *Physics of Fluids* 16(9): 3306–3324.

Wang P., Bai X.S. (2004b). Large eddy simulation of turbulent premixed flames using level-set *G*-equation. *Proceedings of the Combustion Institute*, vol. 30: 581–589.

Wang P., Bai X.S. (2005). Large eddy simulation of turbulent swirling flows in a dump combustor: a sensitivity study. *Int. J. for Numerical Methods in Fluids*, 47: 99–120.

Wang S., Rusak Z. (1996). On the stability of an axisymmetric rotating flow in a pipe. *Physics of Fluids* 8: 1007–1016.

Weber R., Visser B.M., Boysan F. (1990). Assessment of turbulence modeling for engineering prediction of swirling vortices in the near burner zone. *Int. J. of Heat and Fluid Flows* 11: 225–235.

Weller H.G. (1993). The development of a new flame area combustion model using conditional averaging. *Thermo-fluids section report* TF–9307, Imperial college science, Technology and medicine.

Weller H.G., Tabor G., Gosman A.D., Fureby C. (1998). Application of a flame-wrinkling LES combustion model to a turbulent mixing layer. *Proceedings of the Combustion Institute*, vol. 27: 899–907.

Wenzel H., Peters N. (2000). Direct numerical simulation and modeling of kinematic restoration, dissipation and gas expansion effects of premixed flames in homogeneous turbulence. *Combustion Science and Technology* 158: 273–297.

Wessman M. (1995). Laser Doppler measurements of turbulent swirling flows in a circular tube with a sudden expansion followed by a sudden contraction. *Licentiate thesis*, Lund University, Sweden, Report ISRN LUTMDN/TMVK-7018-SE.

Westbrook C.K., Dryer F.L. (1981). Simplified reaction mechanisms for the oxidation of hydrocarbon fuels in flames. *Combustion Science and Technology* 27: 31–43.

Wilcox D.C., Rubesin M.W. (1980). Progress in turbulence modeling for complex flow fields including effectes of compressibility. *NASA TP*–1517.

Wilcox D.C. (1998). Turbulence modeling for CFD, second edition. DCW Industries, Inc., California.

Williams F.A. (1975). Recent advances in theoretical descriptions of turbulent diffusion flames. In S.N.B. Murthy, editor, Turbulent mixing in nonreactive and reactive flows, 189–208, Plenum press, New York.

Williams F.A. (1985a). Turbulent combustion. In J. Buckmaster, editor, the Mathematics of combustion, pp. 97–131, SIAM, Philadelphia.

Williams F.A. (1985b). Combustion theory. Benjamin/Cummins, Menlo park, CA.

Williams F.A. (2000). Progress in knowledge of flamelet structure and extinction. *Progress in Energy and Combustion Science* 26: 657–682.

Winckelmans G.S., Jeanmart H., Carati D. (2002). On the comparison of turbulent intensities from large-eddy simulation with those from experiment or direct numerical simulation. *Physics of Fluids* 14: 1809–1811.

Xia J.L., Yadigaroglu G., Liu Y.S., Schmidli J., Smith B.L. (1998). Numerical and experimental study of swirling in a model combustor. *Int. J. of Heat and Mass Transfer* 41: 1485–1497.

Zimont V.L. (1979). Theory of turbulent combustion of a homogeneous fuel mixture at high Reynolds number. *Combustion, explosion, and shock waves* 15: 305–311.

Zimont V.L. (2000). Gas premixed combustion at high turbulence: turbulent flame closure combustion model. *Experimental Thermal and Fluid Science* 21: 179–186.

Zimont V.L., Battaglia V. (2003). RANS, LES and hybrid RANS/LES turbulent premixed combustion TFC model. *Joint meeting of the Scandinavia–Nordic and Italian sections of the combustion institute* No. 2.6. Ischia, Italy, September 18–21.

Glossary

ARSM(ASM)	Algebraic Reynolds Stress Model
BML	Bray–Moss–Libby
CARS	Coherent Anti-Stokes Raman Scattering
CFD	Computational Fluid Dynamics
CMC	Conditional Moment Closure
DLE	Dry Low Emission
DLN	Dry Low NO_x
DNM	Detailed Numerical Modeling
DNS	Direct Numerical Simulation
EARSM	Explicit Algebraic Reynolds Stress Model
EBU	Eddy-Break-Up
EDC	Eddy-Dissipation-Concept
ENO	Essentially Non-Oscillatory
FAS	Full Approximate Storage
FGR	Filter width to Grid spacing Ratio
HSCT	High Speed Civil Transport aircraft
IRZ	Internal Recirculation Zone
LDA	Laser Doppler Anemometry
LDV	Laser Doppler Velocimetry
LES	Large Eddy Simulation
l.h.s.	left hand side
LP	Lean Premixed
LPP	Lean Premixed/Prevaporized
MPI	Message Passing Interface
PDE	Partial Differential Equations
pdf	probability density function
PIV	Particle Image Velocimetry
PLIF	Planar Laser Induced Fluorescence
PVC	Precessing Vortex Core
RANS	Reynolds Averaged Navier–Stokes
r.h.s.	right hand side
r.m.s.	Root Mean Square
RQL	Rich-burn/Quick-quench/Lean-burn
RSM	Reynolds Stress Model
SCR	Selective Catalytic Reduction

SGS	Sub-grid Scale
SFS	Sub-filter Scale
STS	Sub-test Scale
SSM	Stress Similarity Model
TFC	Turbulent Flame (or Flame-speed) Closure
TVD	Total Variation Diminishing
UHC	Unburned Hydrocarbons
VLES	Very Large Eddy Simulation
WENO	Weighted Essentially Non-Oscillatory

Nomenclature

Latin characters

A_m	LES smoothed flame surface area	[m^2]
A_T	instantaneous flame surface area	[m^2]
b	regress variable (1–*c*)	[–]
c	reaction progress variable	[–]
C_{EBU}	EBU model constant	[–]
C_S , C_μ	model constant	[–]
D	mass diffusion coeff.	[m^2/s]
D_T	turbulent mass diffusion coeff.	[m^2/s]
E	kinetic energy spectrum	[m^3/s^2]
f	frequency	[s^{-1}]
G	signed distance to flame surface	[m]
H	height of step	[m]
h	grid length	[m]
k	turbulent kinetic energy per unit mass	[m^2/s^2]
K	stretch rate	[s^{-1}]
l	integral length scale	[m]
l_F	flame thickness	[m]
l_G	Gibson length scale	[m]
l_M	Markstein length	[m]
P	pressure	[N/m^2]
p	probability function	[–]
r	local radius	[m]
R	radius of pipe	[m]
R_c	reaction rate	[s^{-1}]
S	swirl number	[–]
S_{ij}	flow strain rate tensor	[s^{-1}]
s_d	flame front displacement speed	[m/s]
s_{LES}	LES solved flame propagating speed	[m/s]
s_L	laminar flame speed	[m/s]
s_L^0	unstretched laminar flame speed	[m/s]

s_T	turbulent flame speed	[m/s]
T_u	temperature on unburnt side of combustion	[K]
T_b	temperature on burnt side of combustion	[K]
T	temperature	[K]
t_F	reaction time scale	[s]
t_I	turbulent integral time scale	[s]
t_η	Kolmogorov time scale	[s]
t	time	[s]
t_{ij}	molecular viscous stress tensor	[N/m^2]
$\boldsymbol{u}$	velocity vector	[m/s]
U, V, W	mean velocity components	[m/s]
U_b	mean axial velocity at inlet	[m/s]
U_θ, U_r	mean azimuthal and radial velocity	[m/s]
U_{con}	mean outflow velocity	[m/s]
U_{min}	minimum axial velocity	[m/s]
u, υ, w	instantaneous velocity component	[m/s]
u_i	velocity component	[m/s]
u', v', w'	r.m.s. of velocity fluctuation	[m/s]
u_θ', u_r'	azimuthal and radial velocity fluctuation	[m/s]
$\overline{u'u'}$ $\overline{v'v'}$, $\overline{w'w'}$	variance of velocity components	[m^2/s^2]
W_k	molecular weight of species *k*	[kg/kmole]
x, y, z	coordinate component	[m]
x_i	coordinate component	[m]
Y	species mass fraction	[–]
Y_k	mass fraction of species *k*	[–]
Z	mixture fraction	[–]

Greek characters

α	thermal diffusion coeff.	[m^2/s]
α_{ij}, β_{ij}	stress tensor	[N/m^2]
δ_{ij}	Kronecker delta	[–]
δ_{LES}	LES smoothed flame thickness	[m]
ε	turbulent kinetic energy dissipation rate per unit mass	[m^2/s^3]
$\overline{\phi}$	time averaging, or spatial filtering of variable ϕ	

$\tilde{\phi}$	Favre time averaging or spatial filtering of variable ϕ	
ϕ'	fluctuation of variable ϕ from time averaging or spatial filtering	
ϕ''	fluctuation of variable ϕ from Favre time averaging or spatial filtering	
η	Kolmogorov length scale	[m]
κ	wave number	[m^{-1}]
λ	Taylor length scale	[m]
μ	dynamic viscosity	[kg/ms]
μ_t	turbulent eddy viscosity	[kg/ms]
v	kinematic viscosity	[m^2/s]
v_t	turbulent kinetic viscosity	[m^2/s]
ω_k	formation rate of species *k*	[kg/m^3s]
ω_x	axial vorticity	[s^{-1}]
τ_{ij}	SGS stress tensor	[N/m^2]
ρ	density	[kg/m^3]
ρ_u	density on the unburnt side of combustion	[kg/m^3]
ρ_b	density on burnt side of combustion	[kg/m^3]
ξ	SGS wrinkling factor	[–]
Σ	flame surface density	[m^{-1}]
Ξ	flame wrinkling density scalar	[–]
Ω_{ij}	rotation tensor	[s^{-1}]
Δ	LES filter size	[m]

Dimensionless Numbers

$Da = t_I / t_F$	Damköhler number
$Ka = t_F / t_\eta$	Karlovitz number
$Le = \alpha / D$	Lewis number
$Pr = v / \alpha$	Prandtl number
$Re = \rho UL / \mu$	Reynolds number
$Re_l = \rho u' l / \mu$	turbulent Reynolds number
$Sc = v / D$	Schmidt number
Sc_t	turbulent Schmidt number
$St = fR / U$	Strouhal number
$\gamma = (T_b - T_u) / T_b$	dimensionless temperature